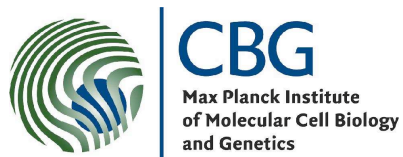


Max Planck Institute of
Molecular Cell Biology and Genetics



**Mechanics of the axoneme:
Self-organized beating patterns and vortex arrays of
spermatozoa**

Dissertation
zur Erlangung des
Doktorgrades der Naturwissenschaften
(Doctor rerum naturalium)

vorgelegt von
Ingmar Riedel
Geboren am 22. Januar 1975 in Sebnitz

1. Gutachter: Prof. Dr. Jonathon Howard
2. Gutachter: Prof. Dr. Frank Jülicher
3. Gutachter: Prof. Dr. Raymond Goldstein

Eingereicht am:

Verteidigt am:

Abstract

Cilia and eukaryotic flagella are long, thin extensions of cells that contain a structure known as axoneme. The key components of the axoneme are microtubule filaments and the motor proteins dynein. These dynein motors force the microtubules to slide in an oscillatory fashion leading to a wave pattern along the axoneme. How these motors are coordinated and how this phenomenon can be described quantitatively is not understood.

I therefore studied the waveforms of sperm tails that contain such an axoneme. I observed these waveforms under different conditions with a high-speed camera and developed an automated image analysis tool allowing the extraction of long time series of this waveform. In a subsequent Fourier analysis I increased the precision by obtaining an averaged waveform. I then compared the data to the predictions of a theoretical framework (Camalet, Julicher et al. 1999) and found that they do not agree. I suggested extending this theoretical framework by considering a visco-elastic element at the base of the axoneme, which leads to a satisfactory agreement. This project leaves open questions hence further work is discussed.

As a side finding, I discovered a new phenomenon on how spermatozoa form dynamic vortex arrays. I described this pattern in detail and introduced a novel order parameter to quantify the order among many particles. I showed that the array only forms above a critical sperm density. I suggested a model to explain the origin of the pattern and showed by simulation that the model can account for the main features of the pattern. Finally I estimated the typical interaction force between beating axonemes to be 0.1 pN and drew conclusions about their collective action in general that might be relevant for sperm cooperation or metachronal waves of cilia.

Zusammenfassung

Cilien und eukariotische Flagellen sind lange, dünne Fortsätze von Zellen. Sie enthalten eine Struktur namens Axonem. Die wesentlichen Komponenten des Axonems sind die Filamente und Motorproteine namens Mikrotubuli und Dynein. Die Motoren forcieren die Filamente, sich in oszillierender Weise gegeneinander zu verschieben, was zu einem Schlagmuster entlang des Axonemes führt. Wie diese Motoren koordiniert werden und wie dieses Phänomen quantitativ beschrieben werden kann, ist nicht verstanden.

Wir studierten die Wellenformen an Spermischwänzen, welche ein solches Axonem enthalten, unter verschiedenen Bedingungen mit einer Hochgeschwindigkeitskamera. Wir entwickelten eine automatisierte Bildanalyse-Software, die es erlaubt, lange Zeitreihen solcher Wellenformen von Filmen zu extrahieren. In einer anschließenden Fourieranalyse erzielten wir eine gemittelte Wellenform mit erhöhter Präzision. Ein Vergleich von unseren Daten mit den Vorhersagen einer Theorie (Camalet, Julicher et al. 1999) führte zu einer Diskrepanz. Entsprechend schlugen wir eine Erweiterung der Theorie vor, indem wir annahmen, daß an der Basis des Axonems ein viskos-elastisches Element existiert. Dies führte zu einer zufrieden stellenden Übereinstimmung zwischen Theorie und Experiment. Abschließend diskutieren wir offene Fragen und zukünftige Experimente.

Als ein Nebenprodukt entdeckten wir ein neues Phänomen, bei welchem Spermien Anordnungen von dynamischen Strudeln (Vortices) bilden. Wir beschrieben dieses Phänomen im Detail und führten einen neuen Ordnungsparameter ein, mit dem die Ordnung zwischen vielen Objekten quantifiziert werden kann. Mittels dieses Ordnungsparameters konnten wir zeigen, daß dieses Muster sich erst ab einer kritischen Dichte herausbildet. Wir schlugen ein Model vor, um den Ursprung des Musters zu erklären. Die Simulation des Modells zeigte volle Übereinstimmung mit den wesentlichen Eigenschaften dieses Musters. Weiterhin schätzten wir die typische Wechselwirkungskraft zwischen aktiven Axonemen mit 0.1 pN ab. Abschließend ziehen wir Schlußfolgerungen über die kollektive Wirkung von Axonemen im Allgemeinen mit Hinblick auf Spermienkooperation und metachronale Cilienwellen.

Epistemology:
Is knowledge knowable? If not, how do we know this?
Woody Allen (Allen 1980)

This work is dedicated to
Dana, Luzy, the Keks,
and everyone my spermatozoa will bring along in the future.

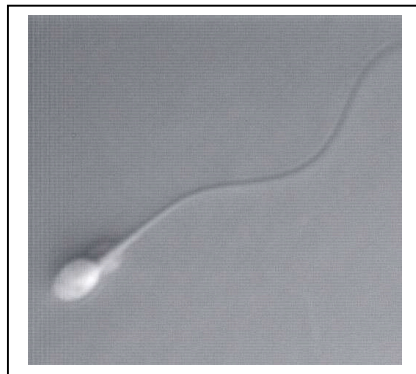


Table of content

Introduction and overview.....	9
1. Present knowledge on axonemal beating	11
1.1. Abstract.....	11
1.2. Cilia and flagella.....	11
1.3. Dynein – a molecular motor	21
1.4. A generic theory for the axonemal beat	31
1.5. Conclusions	40
2. High precision waveforms and the test of a generic theory.....	41
2.1. Abstract.....	41
2.2. Methods.....	41
2.3. Experimental results: Waveforms	50
2.4. Fit results: Test of a generic description.....	53
2.5. Discussion and conclusions	66
3. Self-organized vortex array of sperm cells	71
3.1. Abstract.....	71
3.2. Introduction: The experimental observation.....	71
3.3. Methods.....	73
3.4. Results.....	75
3.5. Discussion and conclusions	81
Outlook.....	83
Appendices	85
A1 Coordination of axonemal beating	85
A2 Self-organized vortex array	97
A3 Supplementary movies	108
List of Figures	110
List of Tables.....	110
List of Movies	111
List of Publications.....	112
Acknowledgements	114
Bibliography	117

Introduction and overview

Modern biology is faced with the challenges of complexity and quantitation. Many phenomena depend on many parameters; hence the behavior of these systems cannot be understood purely by qualitative pictures and intuition, e.g. see (Pollard 2003). Instead mathematical tools need to be applied to study and model such phenomena. This in turn also requires new types of experiments, which extract quantitative parameters and test the theoretical predictions. Consequently this has opened up a variety of interesting problems and attracted many mathematicians and physicists to study biological problems – including myself.

This “quantification of biology” is one of the big slogans of our time and generates the impression that biology has “only” been a qualitative science until very recently. Although there is a lot of truth in this statement, I am worried that the traditional approaches and achievements of biologists and biochemists get underrated - actually in two ways: First, there are many things that need to be explored and described qualitatively before one even could think about a quantitative analysis, e.g. the tedious work of identifying new genes. And second, there has always been a strong tradition of quantitative analysis and modeling in biology, just to mention the classic work on action potentials in neurons by Hodgkin and Huxley (Hodgkin and Huxley 1952).

Another classic example is the analysis on how a spermatozoon generates the beating pattern of its tail. In contrast to the work on action potentials the answer to the question of sperm beating cannot be found in a few seminal papers published within a short period of time. Instead, many scientists made different breakthroughs over a few decades, while some of the central questions are still not solved today.

When introduced to this problem I got immediately fascinated. Motivated by combining experiments and theories I almost got torn apart somewhere between petting sea urchins in a self-built aquarium and calculating functional derivatives. That this actually did not happen and I finally can present this thesis is also a merit of my supervisor Jonathon Howard and of our close collaborators from the MPI-PKS, namely Andreas Hilfinger, Karsten Kruse, and Frank Jülicher.

The work itself is divided into three parts that are sandwiched by this introduction and an outlook. In the appendices I give additional controls and discussion. Furthermore a CD accompanies this thesis containing movies to illustrate the dynamic patterns that spermatozoa can generate.

The first part is a summary of what is known about the organelles called cilia and flagella. The tail of a spermatozoon is exactly such a (eukaryotic) flagellum. We will see how the internal molecular motors force the internal filaments to slide in an oscillatory fashion, giving rise to a wave pattern on the sperm tail. This then leads me to the open questions: How are these motors coordinated and how can a theoretical framework be set up to quantitatively predict the beating pattern? Consequently I review a theoretical framework developed by Camalet and coworkers (Camalet, Julicher et al. 1999; Camalet and Julicher 2000) that potentially answers these questions and I also introduce some extensions to this work that are motivated by my experimental findings.

In the second part I present the experimental work to measure the waveforms of a beating bull spermatozoa with high precision under different conditions. The movies were acquired with a high-speed camera. I developed an automated image analysis tool allowing the extraction of long time series of this waveform. In a subsequent Fourier analysis I increased the precision by obtaining an averaged waveform. This data was used to test the theoretical predictions by Camalet. I find a very good agreement between experiment and theory given that some extensions to the original work by Camalet are considered, namely a visco-elastic element at the base of the axoneme. This project leaves open questions hence further work and experiments are discussed.

In the third part I describe the discovery of a new phenomenon on how sea urchin spermatozoa form dynamic vortices. I study this pattern in detail and introduce a novel order parameter to quantify the order among many particles. I show that the array only forms above a critical sperm density. I suggest a model to explain the origin of the pattern and show by simulation that the model can account for the main features of the pattern. Finally I estimate the typical interaction force between beating axonemes and draw conclusions about their collective action in general.

1. Present knowledge on axonemal beating

1.1. Abstract

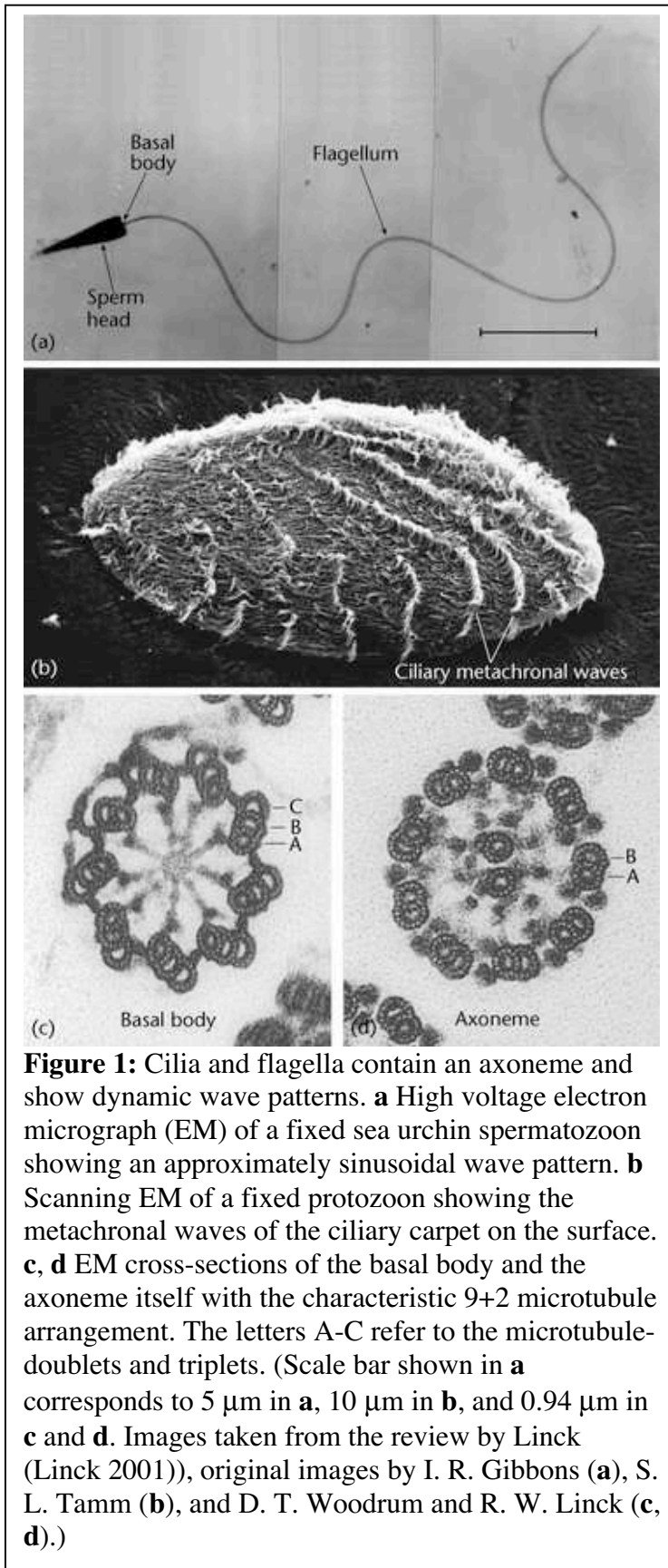
In this chapter I summarize the earlier work concerning cilia and flagella by other groups with a focus on the question how the beat of a spermatozoon can be described quantitatively based on the knowledge of its molecular details. This is one of the central questions of this thesis. Particular attention is given to the theoretical work by Camalet (Camalet, Julicher et al. 1999; Camalet and Julicher 2000) since it is tested against my experimental data in the succeeding chapter. Furthermore, I present and discuss some extensions of the work by Camalet that are necessary to find an agreement with the experimental data.

1.2. Cilia and flagella

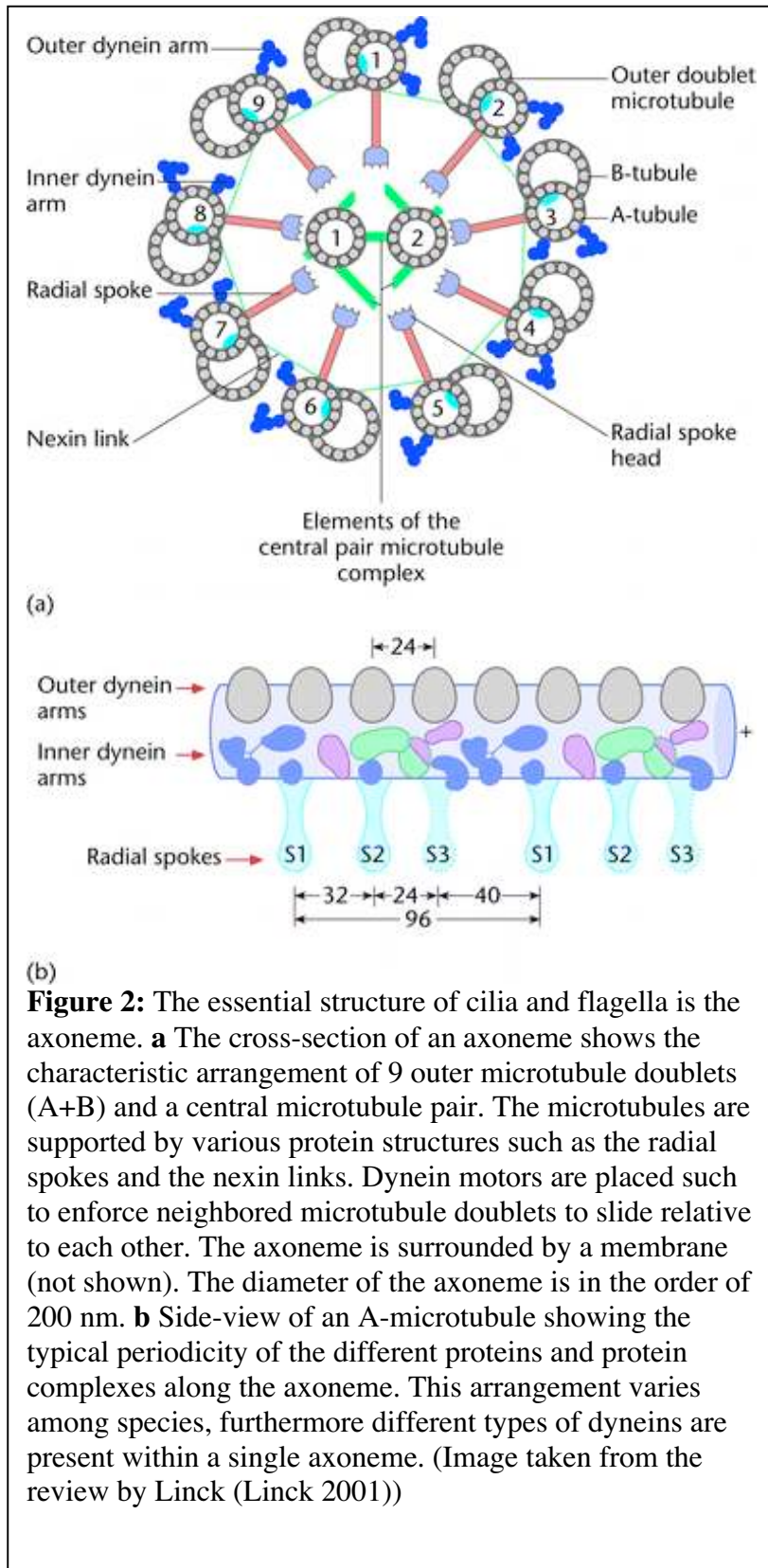
First I introduce the reader to the organelles called cilia and flagella. Especially the facts summarized in the first subsection are largely common textbook knowledge. Therefore the original references are only given for a few special cases. For a deeper introduction including original references I recommend the review articles (Gibbons 1981; Linck 2001).

1.2.1. Design, function and importance of cilia and flagella

Cilia and eukaryotic flagella are long, thin extensions that contain a structure known as axoneme (Fig. 1). The typical dimensions of the axoneme are lengths ranging from 10 μm up to 50 μm (axonemes with lengths into the millimeter regime have been found as well) and diameters of ~ 200 nm. They are surrounded by a cell membrane and sometimes by much thicker and highly specialized structures such as mitochondria.



The typical cross-section of an axoneme is sketched in Fig. 2a. It shows the prototypical 9+2 arrangement of 9 outer microtubule doublets and a central microtubule pair. Dynein-motors are arranged between the microtubule-filaments in a nine-fold rotational symmetry. I will devote a later section to these filaments and motors hence I am very brief at this point. The axoneme contains many supporting and presumably also regulatory structures such as the radial spokes and the elastic nexin links. The total number of different proteins present in an axoneme is several hundreds (~180 according to (Gibbons 1981) but ~700



according to newer studies (personal communication by Charles Brokaw)). Part of a microtubule doublet is shown in side view in figure 2b. The polarity of the microtubules is such that the minus-end, which is the natural walking direction of the dynein-motors, is at the attachment point in the cell body. This attachment point is called the base and usually consists of a basal body, a tubuline-based structure to which the microtubule doublets are connected (Fig. 1c). At the tip of the axoneme the microtubules are loosely attached to the membrane, but they are free to slide relative to each other. Many deviations from this prototypical axoneme

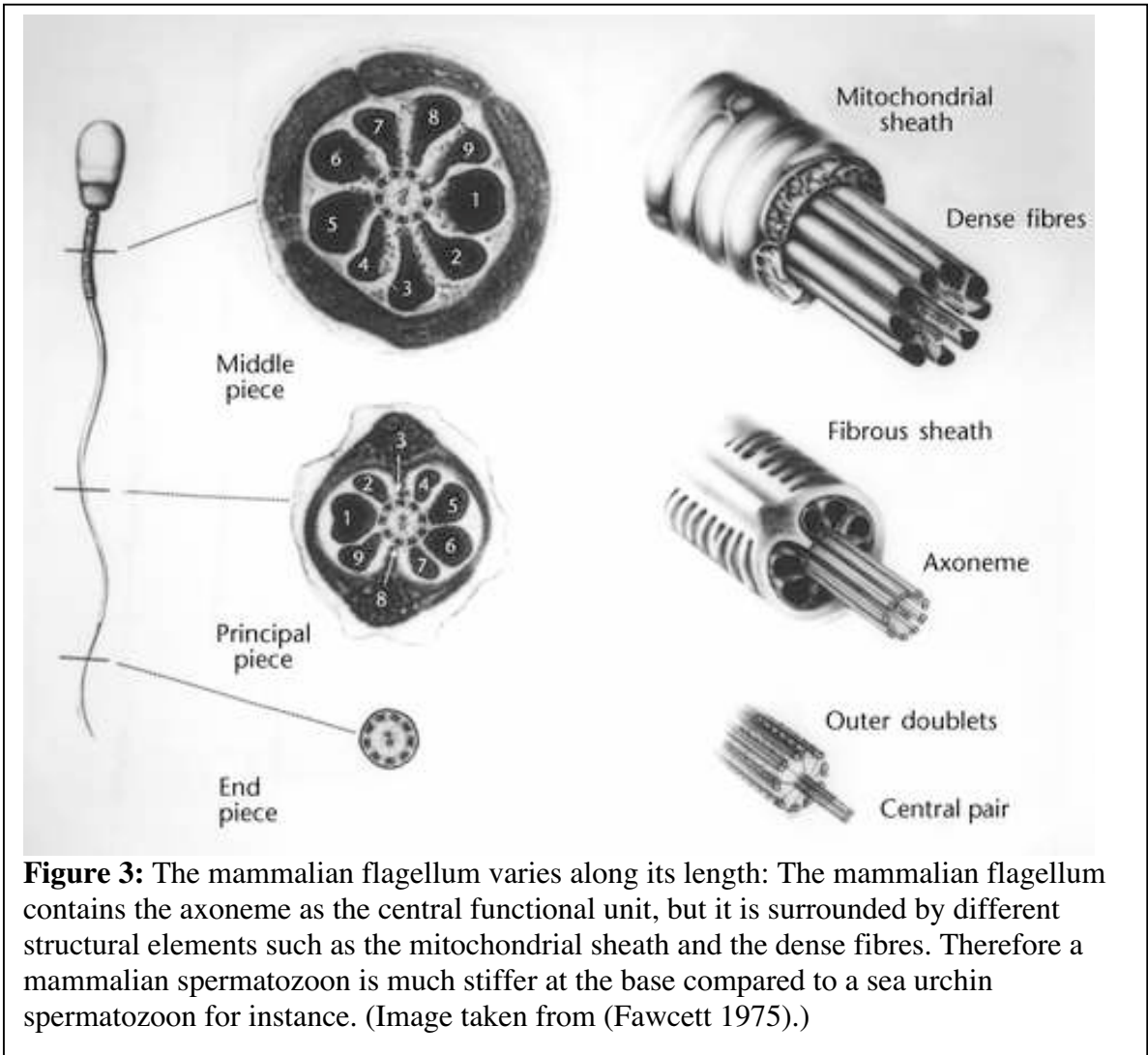


Figure 3: The mammalian flagellum varies along its length: The mammalian flagellum contains the axoneme as the central functional unit, but it is surrounded by different structural elements such as the mitochondrial sheath and the dense fibres. Therefore a mammalian spermatozoon is much stiffer at the base compared to a sea urchin spermatozoon for instance. (Image taken from (Fawcett 1975).)

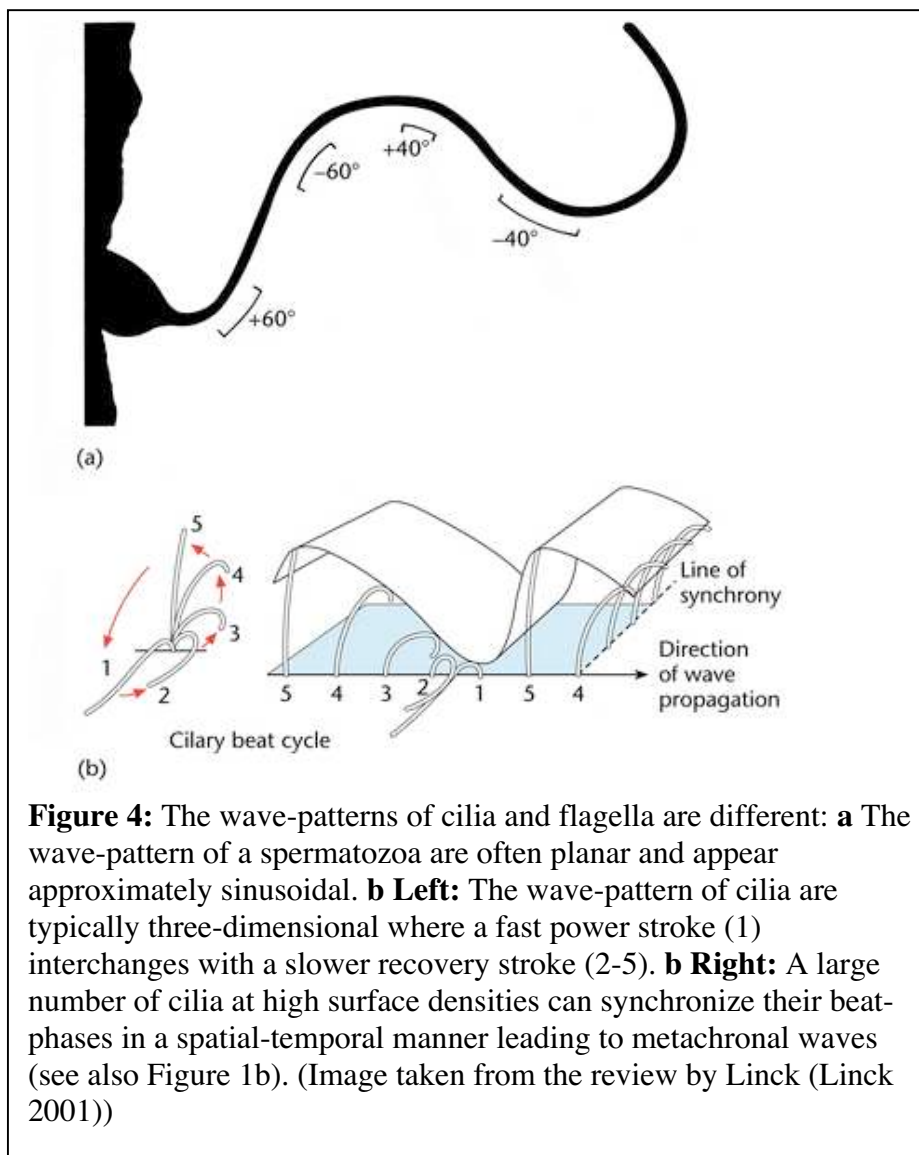
can be found in nature. Figure 3 shows the design of a mammalian spermatozoon that has further structural and functional elements surrounding the axoneme.

The terms cilia and eukaryotic flagella were given at a time before it was recognized by electron microscopy that all these organelles share the same internal design that is now called the axoneme. In contrast bacterial flagella are passive rods and have a rotary motor at their base. Throughout this thesis the term flagella refers to eukaryotic flagella if not explicitly stated.

Cilia and flagella, can undergo periodic, that is oscillatory, motion when active. To generate the beat the dynein motors within the structure convert chemical energy by hydrolyzing adenosine triphosphate (ATP) into mechanical work while they walk on the microtubules. This motor activity forces neighboring microtubule doubles to slide relative

to each other. Due to structural constraints this sliding motion is converted into an oscillatory bending motion. How these motors are coordinated to generate a periodic beating pattern is a central question in the field. I will come back to this question at a later point. The form of the beating pattern itself is regulated by the cells, e.g. changes in Ca^{2+} concentrations typically lead to changes in the symmetry of the waveform; in the trypanosomid *Crithidia* it was even observed, that the direction of wave propagation can be reversed (Holwill and McGregor 1976).

Cilia and flagella have distinct functions. The functional role of flagella is the forward propulsion of cells, such as in spermatozoa. The beating pattern typically consists



of rather symmetrical and propagating waves, often planar or helical (Fig. 4a). Cilia in contrast are usually shorter than flagella and are found very often at high densities on cell or tissue surfaces. A cilium typically beats in two phases with a faster power stroke followed by a slower recovery stroke, where the pattern

looks oar-like (Fig. 4b). Cilia can be found at very high surface densities in ciliary epithelium or in single celled organisms such as *Paramecium* (Fig. 1b). These cilia beat cooperatively in synchrony leading to metachronal waves. The function of a ciliary epithelium is to propel fluids over its surface, leading for instance to the clearance of dirt or to forward propulsion of such a *paramecium*.

The axoneme is broadly distributed among eukaryotes, also within the human body. They are found in the ciliary epithelia of lungs, as tails of spermatozoa and in the primary cilia during early development. Furthermore, non-motile forms exist as supporting structures such as in the hair-bundle or the photoreceptor cell of the eye. Consequently, there are many diseases related to dysfunctional axonemes. Immobile sperm tails cause infertility, paralyzed or uncoordinated tracheal cilia causes chronic bronchitis, and an immobile primary cilium causes situs inversus, to give three prominent examples. This highlights the importance of studying these structures, not only from a purely scientific but also from a medical point of view.

To summarize, the axoneme is a broadly distributed structure in nature, serving different functions. Its key components are microtubules and dynein-motors, leading to the capability of active motion of the axoneme. The questions that I want to focus on are: Why does the axoneme oscillate and can I find a quantitative theoretical framework that predicts the beat-characteristics from the molecular structure of the axoneme?

1.2.2. How to describe the axonemal beat? – A historical account

To achieve a quantitative understanding of the axonemal beat several conceptual steps took place over the last decades. In this subsection I give a historical sketch of the main findings and concepts relevant to this thesis. These lead me to the open questions. Only the most relevant work is referenced since the literature is huge. I focus on the work on spermatozoa as the subject of study of this thesis, although most of the presented findings apply to cilia as well.

Taylor in 1951 (Taylor 1951) was the first one to realize, that the Reynolds number for self-propelled cells are very low (10^{-6} to 10^{-4} for individual cilia and 10^{-2} to 10^{-1} for protozoa (Gibbons 1981)), hence propulsion is different than for a human in water, for instance. At low Reynolds numbers inertia is negligible. In order to gain any directed

movement by periodic forcing the time reversal symmetry needs to be broken. For a nice introduction I recommend “life at low Reynolds numbers” (Purcell 1977). In order to describe the forward movement of a spermatozoon, the Stokes equation was solved by Hancock in 1953 (Hancock 1953), which is linear at low Reynolds numbers. In 1953, Gray and Hancock simplified the description of the viscous fluid by using two local drag coefficients (Gray and Hancock 1955), furthermore they calculated the forward velocities of spermatozoa from the observed waveforms. These forward-velocities are in reasonable agreement with the experimental observations. Since then such forward-velocities have been calculated for different beat patterns and head-sizes (Blum and Hines 1979). Generally it can be concluded, that predicting swimming velocities from a certain beating pattern is understood very well in first approximation.

It was also Gray in 1955 (Gray 1955) who took the first photographs of waveforms of single sea urchin spermatozoa. Sea urchin spermatozoa are easily observable due to their circular swimming paths and planar beat patterns when close to surfaces. The waves of the sperm tail have almost constant amplitudes along the tail. The waveforms of other spermatozoa, especially bull, were observed in succeeding years (Gray 1958; Rikmenspoel, Vanherpen et al. 1960). It was found for bull spermatozoa that the amplitude increased towards the end of the tail, in contrast to sea urchin spermatozoa.

The next question was how certain waveforms and beating patterns are generated. In 1958, Machin was the first one (Machin 1958) to give a mathematical treatment on this problem. He correctly concluded that the force must be generated all along the length of the axoneme due to the not-decaying amplitude of the waves in such a highly over-damped environment. (Actually, Sharpey hypothesized the same scenario already in 1835 (Gibbons 1981).) At that time it was not clear what the force-generators were and Machin assumed contractile elements along the flagellum. He set up a fourth order differential equation that included the flexural rigidity of the flagellum, the viscous drag of the surrounding fluid and the forcing of active internal elements. In 1963 (Machin 1963) Machin reasoned that the oscillations resulted from a feed-back loop being a nonlinear oscillator that determines amplitude and frequency of the oscillation, furthermore allowing the synchronization of close-by flagella as described in 1928 by Gray (Gray 1928).

The next breakthrough was achieved when Gibbons identified the dynein arms between the microtubules as the force-generating elements (Gibbons and Rowe 1965; Gibbons and Gibbons 1972). This discovery led to the concept of motor driven oscillatory microtubule sliding. Gibbons was able to reactivate demembrated sea urchin spermatozoa with Triton in an ATP-buffer obtaining beating patterns very similar to those in live spermatozoa (Gibbons and Gibbons 1969). Precursors of this technique but with less success had been developed by others, mainly Hoffmann-Berling (Hoffmann-Berling 1955) and Brokaw (Brokaw 1961). This demembration and reactivation technique turned out to be a powerful tool since the beating patterns and frequencies under various bio-chemical conditions could be studied. Gibbons treated such demembrated spermatozoa with trypsin to destroy structural components of the axoneme (Summers and Gibbons 1971). Adding then ATP to the buffer he found an up to 8-fold elongation of the structure. This experiment showed (also with some further experiments that I do not want to explicitly mention here) that the molecular motors force the microtubules to slide relative to each other by molecular motors. He named these motors dynein. As found later the trypsin digestion led to the disruption of the nexin links and radial spokes, while the microtubules and the dynein-motors stayed intact. From these experiments, it was reasoned that inside an intact axoneme the sliding of the axoneme is partially hindered by structural elements leading to a conversion of the microtubule sliding into a bending of the axoneme. Correspondingly the so-called sliding-bending hypothesis was formed which is now a well-established and supported paradigm in the field. It has furthermore been shown in electron microscope studies by Satir (Satir 1968), that the microtubules are free to slide at the tip but not able to slide at the base, supporting the sliding-bending hypothesis.

Further insight came from micro-manipulation experiments. Micro-needles were used to measure flexural rigidities on immotile axonemes and forces produced by active axonemes (Lindemann, Rudd et al. 1973; Okuno and Hiramoto 1979; Schmitz, Holcomb-Wygle et al. 2000). The values obtained agree very well with what we know today from single molecule experiments on microtubules (Gittes, Mickey et al. 1993) and dynein motors (Shingyoji, Higuchi et al. 1998). Furthermore, active spermatozoa were mounted on their head to a piezo-driven micro-needle and the beat-characteristics under

different stimuli were studied (Gibbons, Shingyoji et al. 1987). It was found that the axoneme adapts to the externally imposed frequency, which shows, that the axonemal oscillator structurally couples and feedbacks to the actual beating state of the axoneme. This is in contrast to the possibility of some autonomous oscillator periodically stimulating the motors, for instance in the form of a chemical oscillator sitting in the head of a spermatozoon. The same conclusion had already been drawn by Machin (Machin 1963) from the fact, that two nearby spermatozoa can synchronize their beat (Gray 1928).

Another important experimental finding was that a beating spermatozoa can be stalled in any part of the beat cycle with a micro-needle while after removing the needle the flagellum resumes its beating cycle in the same part of the beat cycle as it has been before (Schmitz, Holcomb-Wygle et al. 2000). Furthermore demembrated spermatozoa could be “frozen” into a waveform by quickly taking away the ATP, while re-adding the ATP led to resuming of the beat at the same part of the beat cycle (Gibbons and Gibbons 1974). Both experiments indicate that there is a structural memory within the axoneme about the beating state that can be preserved over times longer than the typical beating period.

Given the nine-fold symmetry of the axoneme (Fig. 2a) and the unidirectional movement of the dynein-motors, it is obvious that the axoneme might twist if all the motors were pulling at the same time. But it is not obvious how oscillatory motion can be achieved in this way. Consequently, the focus of the research shifted to the question, how the motors are controlled or coordinated to enforce microtubule sliding in the required spatio-temporal order to generate the observed wavy and oscillatory beat patterns. This is considered as one of the main open question in the field up to today.

Suggested concepts for this motor coordination (among others) are curvature control (Brokaw 1971; Brokaw 1972), geometrical switches within the axoneme that change the inter-microtubule spacing and consequently changing the rate constants for the motors (Lindemann and Kanous 1995), or spontaneous oscillations of collective motors that are coupled to an elastic element (Brokaw 1975; Julicher and Prost 1997). (I will discuss these concepts in a later subsection in more detail.)

Many analytical and numerical studies and simulations were carried out to predict waveforms for certain concepts of internal motor coordination (Hill 1974; Brokaw 1975;

Hines and Blum 1979). These predicted waveforms were compared to the waveforms of spermatozoa from different species observed under various conditions such as increased viscosities and changed ATP-concentrations. All of the published work demonstrated waveforms that look reasonable under certain conditions and consequently making the assumed concept a valid candidate for motor coordination. But often under extreme conditions such as very high viscosity these descriptions break down. Usually it is hard to judge whether this is simply due to some approximation leading to failure when the approximation is not valid anymore or whether the assumed concept of motor coordination as such is not adequately describing what actually happens inside the axoneme. Especially due to the large number parameters it is often hard to judge what influence each component has and how relevant it is for the real system.

Finally I want to mention that tremendous understanding of motor proteins at the single molecule level has been achieved over the last two decades. I will review this field in the following section. This understanding gives hope that the question of motor-coordination within the axoneme can be posed more sharply and also can be answered in the near future. Further insight comes from more simple but similar systems of molecular motors showing oscillations, such as the spindle oscillator (Grill, Julicher et al. 2005).

In summary the sliding-bending hypothesis as the principle underlying the axonemal beat is well established, and it leads to a quantitative description that combines the internal motor-forces with the flexural rigidity of the axoneme and the external fluid drag. It is furthermore clear that the axoneme oscillates via a feedback loop. This means that the motor activity couples back to the actual beating state which then determines the frequency and amplitude of the oscillation. This is in contrast to an externally driven oscillation. The main open questions are: How is this periodic motor activity achieved and coordinated? Can I find a theoretical framework based on the molecular details of the axoneme that predicts the waveform under various conditions? What role do the various structural details play, such as the connection of the axoneme to the base or the nexin links along the axoneme?

1.3. Dynein – a molecular motor

In this section I sketch a picture on how molecular motors work – alone or in large numbers. I do not restrict myself purely to dynein as the motor acting inside the axoneme, instead I also comment on kinesin and myosin since many concepts on how dynein does and might work were developed on these other two. Furthermore I focus on the question how such motors can generate oscillations. There is definitely much more to be known about motor proteins – I refer the interested reader for a deeper introduction to (Schliwa and Woehlke 2003) (Schliwa 2003) (Howard 2001).

1.3.1. Motor proteins and the cytoskeleton

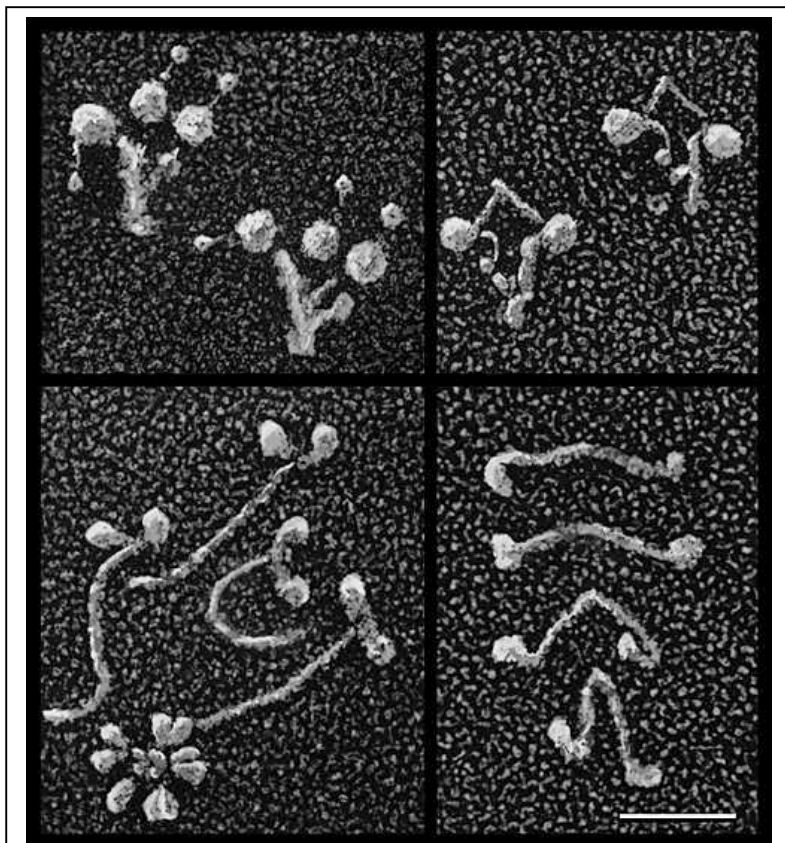


Figure 5: The different cytoskeletal motors as seen by EM. **Upper left:** 3-headed ciliary dynein from *Tetrahymena*. **Upper right:** 2-headed cytoplasmic dynein from chick cells. **Lower left:** Myosin from *Acanthamoeba*. **Lower right:** Kinesin from chick brain. (Scale bar: 40 nm. Image taken from (Hollenbeck 1989).)

Motor proteins are enzymes that convert chemical energy into mechanical work by hydrolyzing ATP. (In the following I restrict myself to the so-called cytoskeletal motor-proteins.) The first cytoskeletal motor protein discovered was myosin in muscles (Huxley 1957), followed by dynein (Gibbons and Rowe 1965) in axonemes, and by kinesin (Brady 1985) being responsible for transport in axons. Each of these motor-proteins forms a class by itself, meaning that many different isoforms of e.g.

dynein exist even in a single species. These motors have various functions. For instance dynein does not only drive axonemal motility, another type of dynein is also present in the cytoplasm being responsible for the intra-cellular transport towards the nucleus. Figure 5 shows the electron micrographs of the different motors.

These motor proteins walk upon filaments that constitute the cytoskeleton. Figure 6 shows the three main filaments, namely actin filaments, microtubules and intermediate filaments. These filaments have a polarity setting a preferred direction for the motors to walk to. While both, kinesin and dynein, walk along microtubules, the former moves

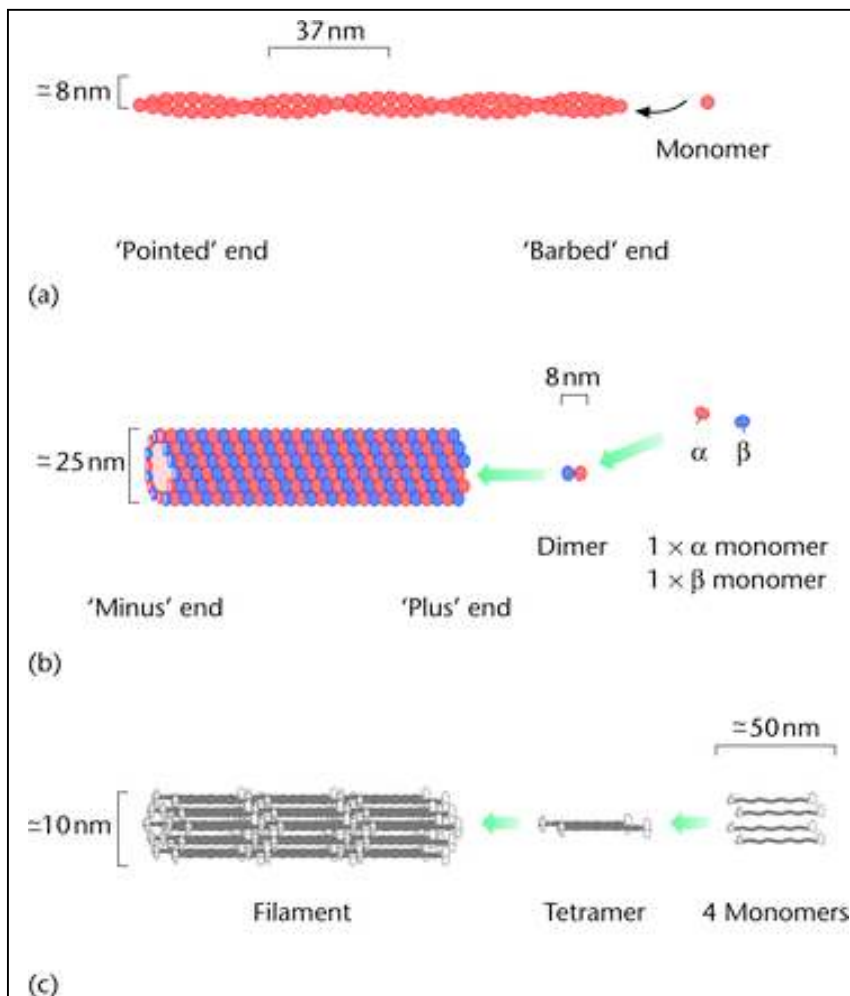


Figure 6: The cytoskeleton consists of three main types of filaments: **a** The actin filament is built from monomers and has the shape of a double helix. **b** The microtubule is a hollow tube formed from tubulin dimers. **c** The intermediate filament is a bundle made of various types of monomers. (Image taken from the review by Insall (Insall and Machesky 1999).)

towards the “+”-end while the later towards the “-”-end. Myosin in contrast walks along actin-filaments. Actin filaments and microtubules are made of proto-filaments that have a dynamic structure; that is, they can shrink and grow. Microtubules are hollow cylinders with a circumference of typically 13 protofilaments but other arrangements are possible such as the microtubule doublets found in the axoneme. The

periodicity along the microtubule is 8 nm as given by the size of the dimers in the protofilaments. This periodicity for instance determines the step size of kinesin. Actin filaments in contrast form a left-handed helix of actin monomers with a full period of 72 nm. Hence the lattice constant as seen by a motor is 36 nm.

These cytoskeletal filaments have various functions: First, they form a scaffold that is a main determinant of the cell-shape. The persistence length of a microtubule for instance is 6 mm (Howard 2001), hence over a typical cell diameter of 10 μm or the length of an axoneme of 50 μm the microtubule is stiff, accordingly it forms the “backbone” of axons in nerve cells for instance. Actin filaments in contrast are much softer and have a persistence length of 15 μm (Howard 2001). Secondly, microtubules and actin filaments serve as “highways” for the motor-proteins for intracellular transport. This leads to directed transport, which is furthermore faster than diffusion on relevant cellular length scales, such as to transport an organelle inside a cell over 1 μm (Howard 2001). Thirdly, these filaments are involved in dynamic process in cell motility such as the actin-polymerization-front in keratocytes and microtubule-based chromosome segregation during cell division.

These cytoskeletal based motors are not the only motor proteins that exist. For instance the DNA-polymerase, which walks along the DNA to synthesize mRNA, or the ATP-synthase, which is a rotary motor sitting in the membrane and using a proton-gradient to generate ATP from ADP and P, and many others are also called motor proteins. For a more general reading I refer to (Schliwa 2003).

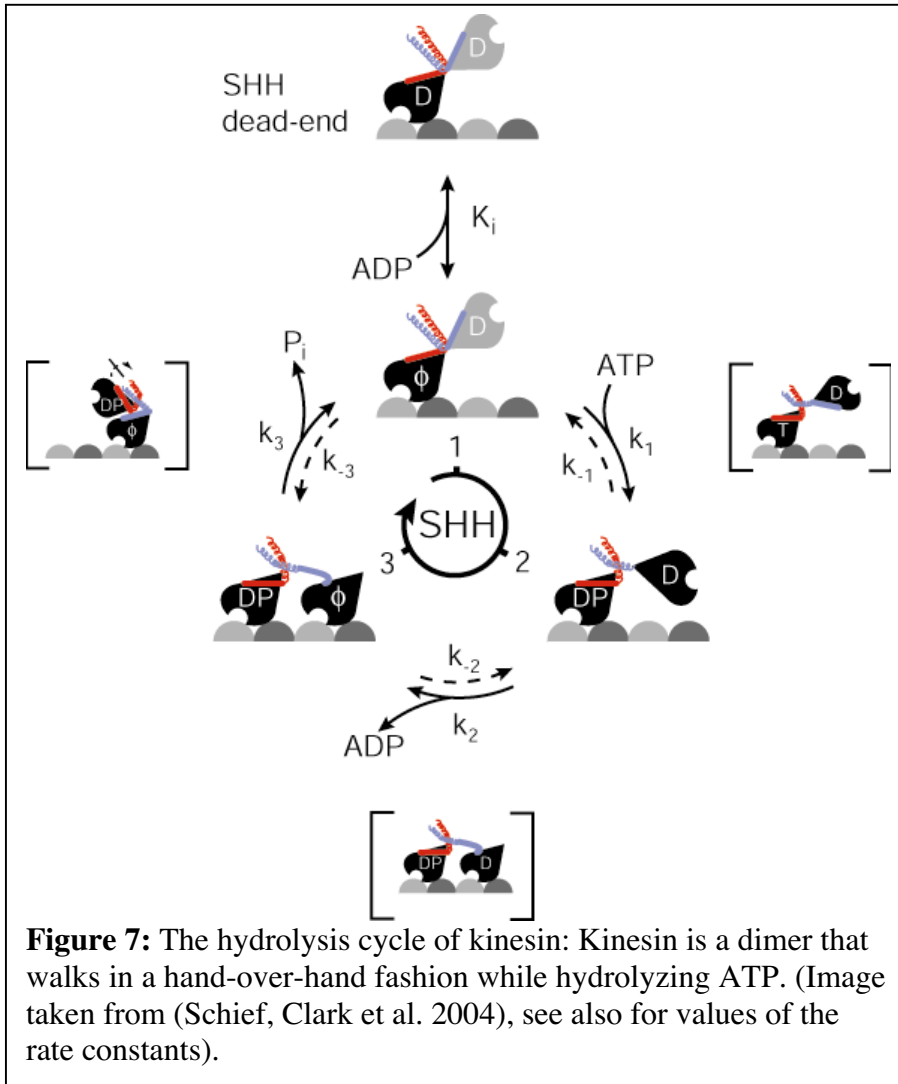
1.3.2. Motor concepts: Lessons from kinesin and myosin

Starting from a molecular picture, it is natural to ask how a single motor protein or a group of them manages to perform a directional movement relative to the lattice of a filament. This involves a series of periodically performed conformational changes of the protein. I want to explain the concepts developed to describe the functioning of such proteins using kinesin and myosin as examples. These concepts were developed while studying these two, which have many things in common but also show substantial differences. Dynein itself is not as well studied as the other two – especially due to its

comparatively larger size. But the concepts presented here are applicable as well to dynein, and we should not be surprised if the study on dynein brings up more concepts.

As a first example I discuss conventional kinesin. Kinesin has two identical heads that alternately step along the lattice in a so-called hand-over-hand mechanism (Fig. 7) (Schief, Clark et al. 2004), very similar to a pedestrian walking along the street. This leads to the concept of processivity that describes whether a single motor can walk or whether many motors are required. Kinesin is a processive motor. For each step kinesin takes it hydrolyses one molecule of ATP. Both heads are highly coordinated concerning the stepping and the nucleotide binding state they are in. This way of forward movement also requires that always one head is bound to the filament at any given time to prevent the fall-off of the motor from the filament. The maximum speed that a kinesin molecule can achieve is then given by $v = k \cdot d$, where d is the step-size and k the hydrolysis rate of a two-headed kinesin in the presence of microtubules. The step-size for kinesin has been measured to be $d=8$ nm, which is the lattice spacing of a microtubule. Together with a hydrolysis-rate at of $k=100$ 1/s for the single head this leads to a maximum speed of $v=800$ nm/s, which has consistently been measured in other setups (Howard 2001). This brings me to the concept of the duty-ratio, which is defined as the fraction of the time of the ATP-cycle each head spends attached on the filament. For conventional kinesin this duty ratio clearly has to be at least 1/2 or larger meaning that one head is always attached to the lattice.

The next important question is how the speed is affected if a load is applied. It was found that the speed decreases with increasingly opposing force leading to the concept of force-velocity curves. Typically these force-velocity curves can be approximated by a linear relationship $F = F_{\text{stall}}(1 - v/v_{\text{max}})$, where F is the applied force, v the actual speed, F_{stall} the stalling force at which the motor does not move anymore, and v_{max} the maximal velocity the motor can walk. Such curves have been measured by various techniques, e.g. with optical traps. The stall force for kinesin has been measured to be $F \approx 6$ pN (Howard 2001). Considering the step size of $d=8$ nm we find that the maximum work is $W = Fd = 5 \cdot 10^{-20}$ J, which can be compared to the free energy of a single ATP-molecule inside the cell of $G = -10 \cdot 10^{-20}$ J (Howard 2001). Hence one can say that kinesin is about 50% efficient at high loads. Finally I mention the concept of run length, which



measures the number of steps a motor can take before it falls off the lattice. For a single kinesin in the absent of any forces this was measured to be 125 steps on average (Howard 2001).

Myosin is different in a few very important aspects compared to kinesin. It moves along actin filaments. Some members of the

myosin-family exist, e.g. myosin V (Howard 2001) that also have two heads like kinesin and move in a similar processive manner. But in contrast, myosin II, though it has two heads like kinesin, cannot move on its own along the lattice and hence it is non-processive. Instead myosin II molecules have to work together in large numbers. In muscles, all motors are attached to a common backbone hence effectively forming a multi-headed motor. Some fraction of these heads is always attached to the actin filaments on which the motors walk on. The other fraction of heads is detached and recovers from their power stroke. Myosin II is a low duty ratio motor; under low load a myosin head spends most of the time of its hydrolysis cycle detached from the filament. Only for a very short fraction of the hydrolysis cycle the motor attaches to the filament and does its so-called working stroke. The distance that the myosins travel collectively during the time

that a single motor spends attached to the filament defines the working distance of a single myosin. This distance corresponds directly to the conformational change the molecule undergoes while being attached to the actin filament. Note that distance traveled during a full hydrolysis cycle is much larger, since for the most part of the hydrolysis cycle the motor is detached from the filament. Since the magnitude of this working stroke depends on the applied load there is no well-defined step-size as for kinesin. Under low load this working distance has been measured to be $d=5$ nm (Howard 2001). The speed of collective myosin motors is then limited by the time $\tau_{on} = 1$ ms that each motor spends attached on average. This maximum speed then is $v = d \cdot \tau_{on} = 5000$ nm/s. Hence many myosin motors together can obtain much higher speeds than a single kinesin.

A force velocity curve for single myosin head does not make sense since it is not processive on its own. But the force-velocity curve of many myosins working together can be measured and maximum forces generated per motor were found to be $F=1.5$ pN (Howard 2001). The shape of the force-velocity-relationship of collective myosins could also be approximated by a linear relationship, although it clearly has some concave component (Howard 2001) stemming from the fact, that at higher forces and accordingly at lower speed each motor spends a larger portion of the hydrolysis cycle attached. Consequently the fraction of attached motors is larger at lower speeds, which in turn lowers the force pulling on each motor. Hence a large number of myosin motors can combine very high velocities under no load with very high pulling forces at very low velocities, a feature we can notice from our muscles everyday.

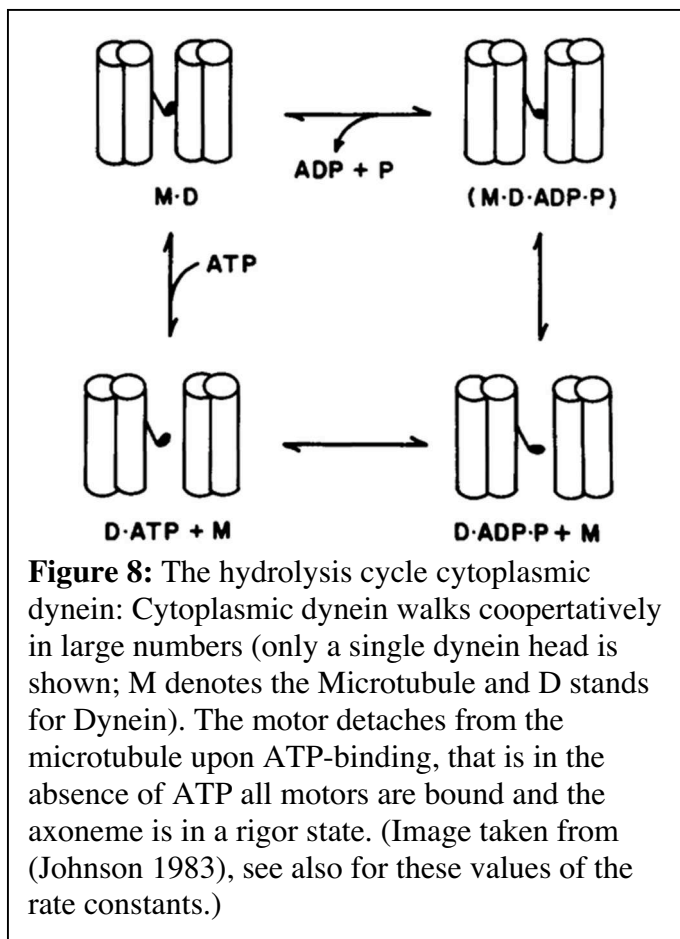
To summarize, conventional kinesin is processive and hence a single molecule can walk on its own, while myosin typically (such as myosin II) is adapted to function in large numbers to obtain much higher speeds under no load or compromise the high speed for higher forces.

1.3.3. Dynein – a more complicated motor

Our knowledge about dynein (Oiwa and Sakakibara 2005) is certainly behind that of kinesin and myosin. It is a much larger protein than the other two. Actually it is a complex of a few smaller proteins, generally termed by their size as heavy, intermediate and light chains. This leads to the following complications: First, it is much more

complicated to purify functional proteins (Gibbons and Rowe 1965) (Nishiura, Kon et al. 2004). Secondly, no crystal structure of all the subunits has been obtained yet (Burgess, Walker et al. 2003). And third, the many subunits leave much more functional freedom possibly leading to more complicated conformational changes and regulation mechanisms. Nevertheless, it was shown by sequence analysis that dynein is a member of the AAA-family (ATPase associated with various cellular activities) which has six potential nucleotide binding sites. Four of these sites have been shown to be active and it is speculated that some of these binding sites rather have a regulatory role, e.g. upon binding of ADP the properties of the whole motor change (Kon, Nishiura et al. 2004). From the cryo-EM studies (Burgess, Walker et al. 2003) also the flexibilities of different dynein parts were estimated (Lindemann and Hunt 2003) leading to the hypothesis, that the way in which dynein walks has to be different at high and low loads.

Two main categories for dynein exist (Oiwa and Sakakibara 2005), namely



cytoplasmic and axonemal dynein.

Cytoplasmic dynein is similar to kinesin and myosin V since a single dynein complex consists of two heads and can walk on its own along microtubules, presumably in a similar hand-over-hand mechanism as kinesin. Cytoplasmic dynein is responsible for a variety of intracellular processes such as organelle transport, organization of the mitotic spindle and chromosome segregation.

Axonemal dynein on the other hand is similar to muscle myosin concerning its function: It works in large numbers and has a low duty ratio, leading to the high

velocities of $v=7000$ nm/s as can be estimated from microtubule sliding inside the axoneme while studying the beating pattern of sea urchin spermatozoa (Howard 2001). As in the case of myosin these sliding speeds can be understood from its off-rate $k=300$ 1/s (Kamimura and Kamiya 1989) and possible step-sizes of $d=16$ nm (Burgess, Walker et al. 2003) leading to maximum sliding velocities of $v=4500$ nm/s. Maximum forces of dynein have been measured to be 6 pN (Shingyoji, Higuchi et al. 1998), which is similar to kinesin and myosin. The hydrolysis cycle of axonemal-dynein is shown in figure 8.

To summarize, axonemal dynein is similar in many aspects to myosin II, although due to its larger size it might show some additional and very fundamental features.

1.3.4. How to describe the oscillations of the axonemal motors?

Oscillations involving molecular motors can be found in many instances, e.g. flight muscle (Pringle 1977), spindle oscillation (Grill, Julicher et al. 2005), or the axoneme as my object of interest.

The cytoskeletal motors are typically mono-directional. Most of the oscillations involving molecular motors are coupled to an elastic element and take place at low Reynolds numbers hence involving no significant inertia. Therefore these oscillations cannot be simply understood as a mass coupled to a spring undergoing oscillations while the motors only replenish the dissipated energy. This raises the question: How can molecular motors, and in particular dynein inside the axoneme, give rise to oscillations?

Different mechanisms have been suggested to explain the oscillations of the axoneme and I want to summarize the most prominent ones. As pointed out already earlier, it is clear from experiments that the oscillation couples back to the actual status of the oscillation. Therefore the oscillator is somehow contained within the structural (mechanical) part of the axoneme. This is in contrast to an external oscillator being independent of the beating state and periodically stimulating the axoneme. I describe the main suggestions presented over the past decades:

The local curvature determines the activity of the motors. Termed as curvature control, this was one of the earliest ideas (Brokaw 1971; Brokaw 1972) after the proposal of the bending-sliding mechanism. Many simulation studies and also analytic studies were undertaken by Brokaw showing the feasibility of the approach but also running into

difficulties to reproduce wave patterns under extreme conditions. A related idea making the molecular mechanism of such a regulatory mechanism more explicit was that the structural changes within the microtubules due to bending influence the rate constants for the motor activity (Hines and Blum 1979).

Collective molecular motors can undergo spontaneous oscillations. This concept has been proposed and studied in theoretical detail (analytical and numerical) by Brokaw (Brokaw 1975) and by Juelicher and colleagues (Juelicher and Prost 1997). Their analysis shows, that a large number of motors coupled elastically to the environment can undergo a dynamic instability leading to oscillations. Plotting the force-velocity relationship of these motors for a parameter set showing oscillations, a negative compliance is found.

Dynein is an oscillating force generator. The idea is, that a single dynein motor is an oscillator on its own. An optical trap experiment by Shingyoij (Shingyoji, Higuchi et al. 1998) shows, that a single dynein molecule (or at maximum two) are capable of undergoing oscillations. The concept of the dynein motor being an oscillator is rather vague, but roughly means that the motor itself moves into both directions in a periodic manner. Therefore the motors inside the axoneme do not have to alternatively pull the microtubules into opposite directions. Instead all motors contribute at all instances to the oscillatory sliding. This idea is based on this single experimental work, which unfortunately has never been repeated and leaves open questions upon its interpretation.

Structural changes within the axoneme hinder the motors on each side alternatively in reaching the opposite microtubule. Such models are based on observations in electron micrographs showing that the spacing between two neighbored microtubule doublets is larger if the dynein arms are un-bound to the opposing microtubule-doublet than when they are bound (Gibbons and Gibbons 1973). It was argued that structural (geometric) constraints exist within the axoneme such that while the microtubule doublets on one side of the axoneme are coming together the ones on the opposite site have to get displaced apart. Consequently only the motors on one side can be active at any time at given piece of the tail. It is further argued that while the motors on one side bend the axoneme in one direction, forces built up at the basal region of the axoneme. These forces then rip off the active motors from the microtubules by pulling the microtubule doublets apart. At the same time the microtubule doublets on the

other side are pushed together activating the motors there. After each switching the activity of the motors travels down the tail. This model has been termed “geometric-clutch-model” and its feasibility has been shown by computer simulations (Lindemann 1994).

Further concepts for the motor coordination exist that I do not want to explicitly mention. The question now is how to test and possibly rule out these explanations. Since we are dealing with such a complicated system, we need more than just sophisticated and insightful experiments. It is also important to develop a reductionistic framework allowing one to discriminate between the key components vs. all the details that lead to minor corrections.

Based on the analytical work by Machin (Machin 1958) and successors, a generic description of the axonemal beat was presented by Camalet and coworkers (Camalet, Julicher et al. 1999; Camalet and Julicher 2000), which is based on the sliding-bending hypothesis but where no particular molecular model for the motors was considered nor how these motors are coupled. Hence general statements can be made that should be valid for all motor models. Particular motor models can of course be incorporated as well and a simplified two state model was discussed that gives rise to spontaneous oscillations (Julicher and Prost 1997). I will discuss this model at a later point. This generic description is then expanded in its different order approximations. This has the advantage that every term can be analyzed systematically, compared to experimental observations and then judged in its importance for the axoneme itself. In the original work by Camalet (Camalet, Julicher et al. 1999; Camalet and Julicher 2000) the linear order was presented and discussed (actually it was done up to second order since these terms canceled for symmetry reasons) being consistent with the earlier analytical work by Machin and others.

In this thesis I will compare my experimental data to exactly this generic description by Camalet. I will test how well it can account for this data and discuss necessary extensions of this framework. And we will see that to a first approximation an additional term has to be incorporated into the theory that seems not to be related to the coordination of the motors at all.

1.4. A generic theory for the axonemal beat

In this section I discuss in more detail the theoretical tools that have been developed and suggested in the past decades by other groups to describe the axonemal beat. In particular I focus on the more recent work by Camalet and coworkers (Camalet, Julicher et al. 1999; Camalet and Julicher 2000), which incorporates these earlier results but is also mathematically very stringent, following the approach of a systematic order-expansion. In the following I refer to this work as ‘‘Camalet’’. The molecular motors are incorporated in a generic way hence the results should be independent from the particular motor model. To quantify the action of these collective motors the self-organized oscillation of motors as suggested by Jülicher (Julicher and Prost 1997) can be applied.

The experimental work presented in this thesis is partly motivated to explicitly test and possibly extend the theory by Camalet. I sketch the derivation by Camalet and introduce two extensions namely the effect of a sperm tail with varying stiffness along its length and the influence of a visco-elastic element at the base, where the tail is attached. Both extensions are motivated by the experimental results presented in the following chapter. In the derivation I focus on the differences compared to the derivation by Camalet, the interested reader is referred for more detail to this original work.

1.4.1. A two-dimensional description

The theory presented by Camalet describes the two-dimensional beat of an axoneme, where two filaments slide relative to each other (Fig. 9). The centerline of the axoneme in space is given by $\mathbf{r}(s)$, where s is the arc-length of the axoneme with $s=0$ at the base, e.g. at the head of the spermatozoon, and $s=L$ at its tip. Assuming incompressibility of the filaments the relative sliding of the internal filaments $\Delta(s)$ at point s is found by integrating the local curvature $C(s)$ along the filament starting from the base:

$$\Delta(s) = a \int_0^s C(s') ds' \quad (1)$$

Here a is the filament-separation. Denoting the tangent on the filament with $\psi(s)$, which is $\partial_s \psi(s) = C(s)$, we find

$$\Delta(s) = a \int_0^s \partial_s \psi(s') ds' = a(\psi(s) - \psi(0)) \quad (2)$$

Hence the tangent on the filament is linearly related to the internal sliding of the filaments. In the case of small amplitude motion the outline of the tail can be described in terms of the deviation from a straight rod measured by $h(s)$, where $\partial_s h(s) = \psi(s)$, which is called Monge-representation.

1.4.2. The enthalpy functional

The enthalpy functional G takes into account the bending of the filaments and the internal stresses due to active and passive elements inside the axoneme:

$$G = \int_0^L \left[\frac{\kappa}{2} C^2 + f\Delta + \frac{\Lambda}{2} (\partial_s \mathbf{r})^2 \right] ds \quad (3)$$

Here L is the length of the axoneme, κ is the bending elasticity of the axoneme, f is the

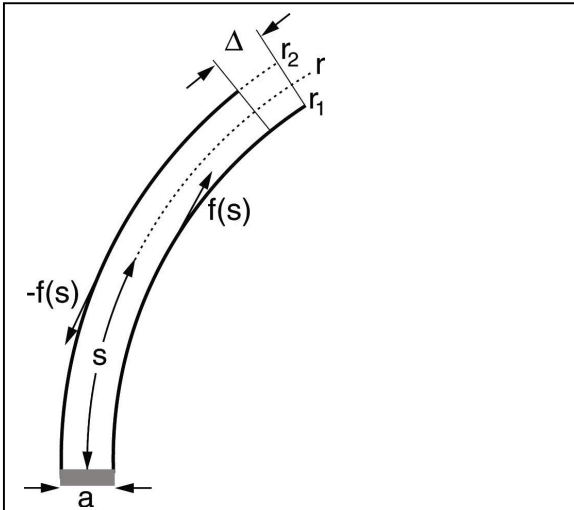


Figure 9: The complex structure of the axoneme is reduced to a pair of sliding filaments: Two filaments are spaced apart by the distance a . The filaments are connected at the base and free to slide at the tip leading to a sliding displacement Δ . The arc-length of the filament pair is described by s . The motors (not shown) generate local forces $f(s)$. (Image taken from (Camalet and Julicher 2000).)

effective active force per unit lengths which forces the filaments to slide relative to each other and Λ is the Lagrange multiplier function ensuring the incompressibility of the system.

After a partial integration and using (eq. 1) we find

$$G = \int_0^L \left[\frac{\kappa}{2} C^2 - aFC + \frac{\Lambda}{2} (\partial_s \mathbf{r})^2 \right] ds \quad (4)$$

where

$$F(s) = - \int_s^L f(s') \cdot ds' \quad (5)$$

Determining the variation δG with respect

to variations in $\delta \mathbf{r}$ we find

$$\frac{\delta G}{\delta \mathbf{r}} = \partial_s [(\kappa \partial_s C - af) \mathbf{n} - \tau \mathbf{t}] \quad (6)$$

where τ plays the role of a physical tension and \mathbf{n} and \mathbf{t} are the normal and tangent on the outline \mathbf{r} .

1.4.3. External fluid friction and the dynamic equation

As discussed earlier the Reynolds numbers for spermatozoa is much lower than 1 hence every motion is highly over-damped and the inertia has negligible influence on the motion.

Using the simplest Rouse-dynamics, the hydrodynamic forces acting on the sperm tail are approximated by two local (perpendicular and parallel) friction forces with the ratio of their friction coefficients being 2 (Howard 2001). Such a Rouse-dynamic is of course an approximation since each part of the tail causes fluid movements elsewhere in the surrounding fluid hence the relative fluid movement at each tail point is not the same as relative to the lab frame. This leads to logarithmic corrections, which can be neglected, especially when low amplitude beating is considered. But it is questionable, whether this is sufficient to precisely describe the waveforms of spermatozoa that can be found experimentally, especially in cases of extreme waveforms such as described by Woolley (Woolley and Vernon 2001).

Now we relate the external drag to the enthalpy functional (eq. 6) to obtain a dynamic equation:

$$\partial_t \mathbf{r} = - \left(\frac{1}{\xi_{\perp}} \mathbf{nn} + \frac{1}{\xi_{\parallel}} \mathbf{tt} \right) \cdot \frac{\delta G}{\delta \mathbf{r}} \quad (7)$$

Here \mathbf{nn} and \mathbf{tt} are the normal and tangential projection operators, ξ_{\parallel} and ξ_{\perp} are the parallel and orthogonal friction coefficients respectively.

Analogous to the derivation by Camalet we then derive in linear order a dynamic equation for the waveform $\psi(s, t)$

$$\partial_s^3 \{ \kappa \partial_s \psi - aF \} = -\xi_{\perp} \partial_t \psi \quad (8)$$

or alternatively in the Monge representation

$$\partial_s^2 \{ \kappa \partial_s^2 h - aF \} = -\xi_{\perp} \partial_t h \quad (9)$$

where the flexural rigidity κ can vary along the tail.

1.4.4. The boundary conditions

Different boundary conditions have been discussed by Camalet. I will focus in the following on the case where the spermatozoon is clamped with its head that is the head does not carry out any motion. In small amplitude approximation Camalet showed that the four boundary conditions are given as:

$$\begin{aligned} h(0) &= 0 \\ \partial_s h \Big|_{s=0} &= 0 \\ \partial_s^2 h \Big|_{s=L} &= 0 \\ \partial_s (\kappa \partial_s^2 h - aF) \Big|_{s=L} &= 0 \end{aligned} \quad (10a-d)$$

We convert these boundary conditions in the $\psi(s,t)$ representation, where we substitute the relation $\partial_s h = \psi$. Since this is not possible directly for the first boundary condition we substitute $h(0) = 0$ in (eq. 9) and then make the substitution $\partial_s h = \psi$.

Hence we find for the boundary conditions:

$$\begin{aligned} \partial_s^2 (\kappa \partial_s \psi - aF) \Big|_{s=0} &= 0 \\ \psi(0) &= 0 \\ \partial_s \psi \Big|_{s=L} &= 0 \\ \partial_s (\kappa \partial_s \psi - aF) \Big|_{s=L} &= 0 \end{aligned} \quad (11a-d)$$

1.4.5. Oscillatory solution

Now we use $\partial_s F(s,t) = f(s,t)$ (eq. 5) and seek an oscillatory solution by making a Fourier-ansatz with $\psi(s,t) = \tilde{\psi}(s) \cdot e^{i\omega t}$ and $f(s,t) = \tilde{f}(s) \cdot e^{i\omega t}$, where ω is the angular beat frequency, which leads to

$$\partial_s^3 \{ \kappa(s) \cdot \partial_s \tilde{\psi}(s) \} - a \partial_s^2 \tilde{f}(s) = -i\omega \xi_{\perp} \tilde{\psi}(s) \quad (12)$$

and the boundary conditions

$$\begin{aligned}
& \left\{ \partial_s^2 (\kappa(s) \cdot \partial_s \tilde{\psi}(s)) - a \partial_s \tilde{f}(s) \right\} \Big|_{s=0} = 0 \\
& \tilde{\psi}(0) = 0 \\
& \partial_s \psi \Big|_{s=L} = 0 \\
& \left\{ \partial_s (\kappa(s) \cdot \partial_s \tilde{\psi}(s)) - a \tilde{f}(s) \right\} \Big|_{s=L} = 0
\end{aligned} \tag{13a-d}$$

1.4.6. Active internal visco-elasticity

The forcing term $\tilde{f}(s)$ can be described in linear response as

$$\tilde{f}(s) = \chi(\Omega, \omega) \tilde{\Delta}(s) \tag{14}$$

where $\tilde{\Delta}(s)$ is the first Fourier mode of the sliding displacement $\Delta(s, t)$. $\chi(\Omega, \omega)$ is the linear response. It describes the influence of the active motors and the passive internal visco-elastic elements, such as stretchable and detachable nexin links leading to protein-springs and protein-friction. Hence $\chi(\Omega, \omega)$ can be written as

$$\chi(\Omega, \omega) = k + i\lambda\omega + F(\Omega, \omega) \tag{15}$$

Here k is the stiffness and λ is the friction per unit length of the passive internal elements, while the last term $F(\Omega, \omega)$ is the linear response of the active motors themselves.

For a particular two state model (Julicher and Prost 1997) this motor response is

$$F(\Omega, \omega) = -\rho k_{CB} \Omega \frac{i\omega / \alpha + (\omega / \alpha)^2}{1 + (\omega / \alpha)^2} = -\rho \frac{U}{l^2} \frac{2\pi^2 \beta}{\alpha} \cdot \frac{i\omega / \alpha + (\omega / \alpha)^2}{1 + (\omega / \alpha)^2} \tag{16}$$

Here ρ is the motor density, k_{CB} is the cross-bridge elasticity of the motors, α is the characteristic ATP-cycling rate. Ω plays the role of a control parameter ($0 < \Omega < \pi^2$) that is related to the rate constants of the motors and measures the distance of the system from thermal equilibrium. Furthermore the substitutions $\Omega = 2\pi^2 \beta / \alpha$ and $k_{CB} = U / l^2$ with U being the typical potential height and l being the wavelength of the potential landscape can be made.

We note that the real and imaginary part of $\chi(\Omega, \omega)$ can be positive or negative. Hence the system can be resting or become unstable and starts oscillating, depending on the general parameter choice. In particular, if Ω increases, e.g. with increasing ATP-concentration, the real or imaginary part (or both) of $\chi(\Omega, \omega)$ becomes positive at a

critical Ω_c and the axoneme starts beating. In the scenario presented by Camalet this corresponds to a supercritical Hopf-bifurcation.

The motor response in (eq. 14) is a generic term, which is independent of the particular motor model. The only exceptions are: First, a constant force is acting additionally, which breaks the assumed symmetry and would lead to an average curvature. Actually, this averaged curvature is found and hence it would be very interesting to discuss, what this constant force might relate to (e.g. it could already stem from the axonemal 9-fold symmetry which together with the glass surface upon which the spermatozoon is swimming leads to a symmetry breaking). Since we discuss an approach, where the eigenmodes separate, there is no loss of generality in neglecting such a constant force and the corresponding average curvature, and hence we concentrate on the oscillatory pattern in the first eigenmode. Second, this linear term could exactly vanish and some higher order term is the governing term. This is possible, but generally a rare case.

1.4.7. Sliding at the base

To my knowledge in earlier theoretical work it has been exclusively assumed that no filament sliding is possible at the base. Motivated by my experimental findings I introduce a basal visco-elastic element that allows such sliding. This is also supported by recent experimental work directly demonstrating basal sliding with electron micrographs (Vernon and Woolley 2004). The enthalpy functional (eq. 3) then acquires an additional term:

$$G' = \frac{K}{2} \Delta_0^2 \quad (17)$$

where K is the stiffness of the visco-elastic element and Δ_0 denotes the basal filament sliding. The filament sliding (eq. 1) needs to be corrected for Δ_0 :

$$\Delta(s) = a \int_0^s C(s') ds' + \Delta_0 \quad (18)$$

Variations of the enthalpy functional and incorporating friction at the base then lead to a dynamic equation describing the displacement at the base

$$K\Delta_0(t) + \int_0^L f(s,t)ds = -\Gamma\partial_t\Delta_0(t) \quad (19)$$

where Γ describes the friction at the base and the integral term describes the motors all along the length leading to the forces that deform this basal element.

Now we can make the Fourier-ansatz as before to find

$$\tilde{\Delta}_0 = -\frac{1}{i\omega\Gamma + K} \int_0^L \tilde{f}(s)ds \quad (20)$$

The internal forces in linear response are (eq. 14)

$$\tilde{f}(s) = \chi\tilde{\Delta}(s) = a\chi[\tilde{\psi}(s) + \tilde{\Delta}_0/a] \quad (21)$$

where $\tilde{\Delta}(s) = a\tilde{\psi}(s) + \tilde{\Delta}_0$ is the Fourier component of the filament sliding taking place along the axoneme. Hence we find

$$\tilde{\Delta}_0 = -\frac{a\chi}{i\omega\Gamma + K + \chi L} \int_0^L \tilde{\psi}(s)ds \quad (22)$$

or alternatively to resolve for the motor response:

$$\tilde{f}(s) = a\chi\tilde{\psi}(s) - \frac{a\chi^2}{i\omega\Gamma + K + \chi L} \int_0^L \tilde{\psi}(s)ds \quad (23)$$

1.4.8. Varying flexural rigidity along the tail

Now I discuss that the flexural rigidity κ varies linearly with the length, which is motivated by earlier measurements on bull spermatozoa (Lindemann, Rudd et al. 1973). Hence $\kappa(s) = \kappa_0 + \kappa_1 s$, where κ_0 is the flexural rigidity at the base and κ_1 describes the decrease in flexural rigidity per unit length. It is negative and is expected to lead to a value of $\kappa(s = L)$ similar to the one of a pure axoneme.

Hence we find from equations (eq. 12)

$$\partial_s^3 \{(\kappa_0 + \kappa_1 s) \cdot \partial_s \tilde{\psi}(s)\} - a^2 \chi \partial_s^2 \tilde{\psi}(s) = -i\omega \xi_{\perp} \tilde{\psi}(s) \quad (24)$$

and

$$\begin{aligned}
& \left\{ \partial_s^2 \left((\kappa_0 + \kappa_1 s) \cdot \partial_s \tilde{\psi}(s) \right) - a^2 \chi \partial_s \tilde{\psi}(s) \right\} \Big|_{s=0} = 0 \\
& \tilde{\psi}(0) = 0 \\
& \partial_s \tilde{\psi} \Big|_{s=L} = 0 \\
& \left\{ \partial_s \left((\kappa_0 + \kappa_1 s) \cdot \partial_s \tilde{\psi}(s) \right) - a^2 \chi \tilde{\psi}(s) + \frac{a^2 \chi^2}{i\omega\Gamma + K + \chi L} \int_0^L \tilde{\psi}(s) ds \right\} \Big|_{s=L} = 0
\end{aligned} \tag{25a-d}$$

If we explicitly carry out the differentiations we find:

$$(\kappa_0 + s \cdot \kappa_1) \cdot \partial_s^4 \tilde{\psi}(s) + 3\kappa_1 \partial_s^3 \tilde{\psi}(s) - a^2 \chi \partial_s^2 \tilde{\psi}(s) = -i\omega \xi_{\perp} \tilde{\psi}(s) \tag{26}$$

and

$$\begin{aligned}
& \left\{ \kappa_0 \partial_s^3 \tilde{\psi}(s) + 2\kappa_1 \partial_s^2 \tilde{\psi}(s) - a^2 \chi \cdot \partial_s \tilde{\psi}(s) \right\} \Big|_{s=0} = 0 \\
& \tilde{\psi}(0) = 0 \\
& \partial_s \tilde{\psi} \Big|_{s=L} = 0 \\
& \left\{ (\kappa_0 + \kappa_1 L) \cdot \partial_s^2 \tilde{\psi}(s) + \kappa_1 \partial_s \tilde{\psi}(s) - a^2 \chi \cdot (\tilde{\psi}(s) + \tilde{\Delta}_0 / a) \right\} \Big|_{s=L} = 0
\end{aligned} \tag{27a-d}$$

1.4.9. Results and discussion

Without the visco-elastic element at the base and a constant filament stiffness κ as presented originally in the work by Camalet we are dealing with a linear fourth order differential equation with constant coefficients, which can be solved analytically leading to solutions of the type $\tilde{\psi}(s) = A_j e^{k_j s/L}$ with four complex k_j , while the complex amplitudes A_j determine the relative contribution of each of the solutions to the overall waveform.

Using a set with typical parameters Camalet obtained beat-frequencies and wavelengths being consistent with what had been observed experimentally by other groups, furthermore they obtained realistic forward swimming speeds. Depending on the boundary conditions different waveforms are selected, for instance in the case of a clamped head the wave travels from the tip of the tail towards the base (which is in contrast to my experimental observations as we will see later), while in the case of a pivoting head or a freely swimming spermatozoon the wave travels from the base towards the head. The traveling solutions themselves did not look particularly sinusoidal.

Finally they argued, that nonlinear terms might play a much more important role under natural conditions, possibly dominating the waveform.

1.4.10. Summary

I restate at this point all the relations that are needed in the next chapter to describe the waveform of a spermatozoon that is clamped at its head. These are: First, the external fluid friction is related to the bending rigidity of the axoneme and the effectively active internal visco-elastic elements:

$$(\kappa_0 + s \cdot \kappa_1) \cdot \partial_s^4 \tilde{\psi}(s) + 3\kappa_1 \partial_s^3 \tilde{\psi}(s) - a^2 \chi \partial_s^2 \tilde{\psi}(s) = -i\omega \xi_{\perp} \tilde{\psi}(s) \quad (28)$$

Second, the internal effective forces are directly related to the waveform $\tilde{\psi}(s)$:

$$\tilde{f}(s) = a\chi \tilde{\psi}(s) - \frac{a\chi^2}{i\omega\Gamma + K + \chi L} \int_0^L \tilde{\psi}(s) ds \quad (29)$$

where the effective internal response can be broken up in its active and passive parts:

$$\chi(\Omega, \omega) = k + i\lambda\omega + \mathbf{F}(\Omega, \omega) \quad (30)$$

And third, the four boundary conditions that select the solution to equation (eq. 28):

$$\begin{aligned} & \left\{ \kappa_0 \partial_s^3 \tilde{\psi}(s) + 2\kappa_1 \partial_s^2 \tilde{\psi}(s) - a^2 \chi \cdot \partial_s \tilde{\psi}(s) \right\} \Big|_{s=0} = 0 \\ & \tilde{\psi}(0) = 0 \\ & \partial_s \tilde{\psi} \Big|_{s=L} = 0 \\ & \left\{ (\kappa_0 + \kappa_1 L) \cdot \partial_s^2 \tilde{\psi}(s) + \kappa_1 \partial_s \tilde{\psi}(s) - a^2 \chi \cdot (\tilde{\psi}(s) + \tilde{\Delta}_0 / a) \right\} \Big|_{s=L} = 0 \end{aligned} \quad (31a-d)$$

I extended the original work by Camalet in two respects. First I explicitly took the physical properties at the basal connection into account by introducing a visco-elastic element at the base. Second I accounted for a varying flexural rigidity along the length. In contrast to this initial work we are now dealing effectively with a linear fifth order differential equation with non-constant coefficients, which is hardly solvable analytically, hence needs to be solved numerically. (The fifth order is a consequence of substituting the integral term in the last boundary condition and consequently transforming all equations to another variable, leading to an increase in order by one.)

1.5. Conclusions

In summary I discussed that cilia and flagella are broadly distributed organelles containing a motile structure called axoneme. This axoneme contains the typical 9+2 arrangement of microtubules plus dynein motors which together constitute the main functional components. Over the past decades lots of experimental and theoretical knowledge has been accumulated, convincingly showing that a large number of molecular motors (dynein) periodically force the internal microtubules to slide in a (usually) oscillatory fashion. The knowledge of the molecular details is good enough to quantify all parameters needed to for a theoretical description. One of the central open questions is how these motors can collectively undergo this oscillatory motion.

Related to this question is the task of developing and proving a theoretical framework that properly accounts for these cooperative motors and that is able to quantitatively predict the observed beating patterns. I explicitly discussed in detail the theoretical work by Camalet, which I will compare to the experimental data in the following chapter. The work by Camalet has the conceptual advantage that it is an order expansion and incorporates the molecular motors in a generic, that is model independent way. Hence I can test to what extend this description agrees with the experimental data and what additional terms have to be considered to make it a valid description for the observed phenomenon. To be explicit, I already presented two extensions, namely that the flexural rigidity varies along the axoneme and that there is a visco-elastic element at the base of the axoneme that allows filament sliding in this region, in contrast to the assumptions in earlier work by other groups.

2. High precision waveforms and the test of a generic theory

2.1. *Abstract*

I investigate how the oscillations and traveling waves of an axoneme can be understood from its molecular structure. As an experimental model I chose bull spermatozoa that were observed close to a planar glass-surface. I imaged single spermatozoa over many beat-cycles with a high-speed camera. A detection software was developed which extracts automatically the wave-form in each frame of these movies. Subsequently, this data was Fourier-analyzed. In earlier work on sperm waveforms only one or two beat cycles were analyzed. Due to my automated method I was able to gather much more data leading in the subsequent Fourier analysis to much higher precision. This enabled me to make some rigorous statements about the boundary conditions acting at the base and the tip of the tail.

I fitted the experimentally predicted waveforms by Camalet and coworkers (Camalet, Julicher et al. 1999; Camalet and Julicher 2000) to my experimental data. I find a good agreement between theory and experiment if a visco-elastic element at the base is considered. All fit parameters are consistent with what has been predicted and measured in earlier experimental work. Moreover the fits look reasonably similar to the observed waveforms.

Finally I discuss open work and problems, including micromanipulation and time-series analysis experiments, both of which are set-up in the lab but too preliminary to be included in this thesis.

2.2. *Methods*

2.2.1. Sperm, microscopy and high-speed imaging

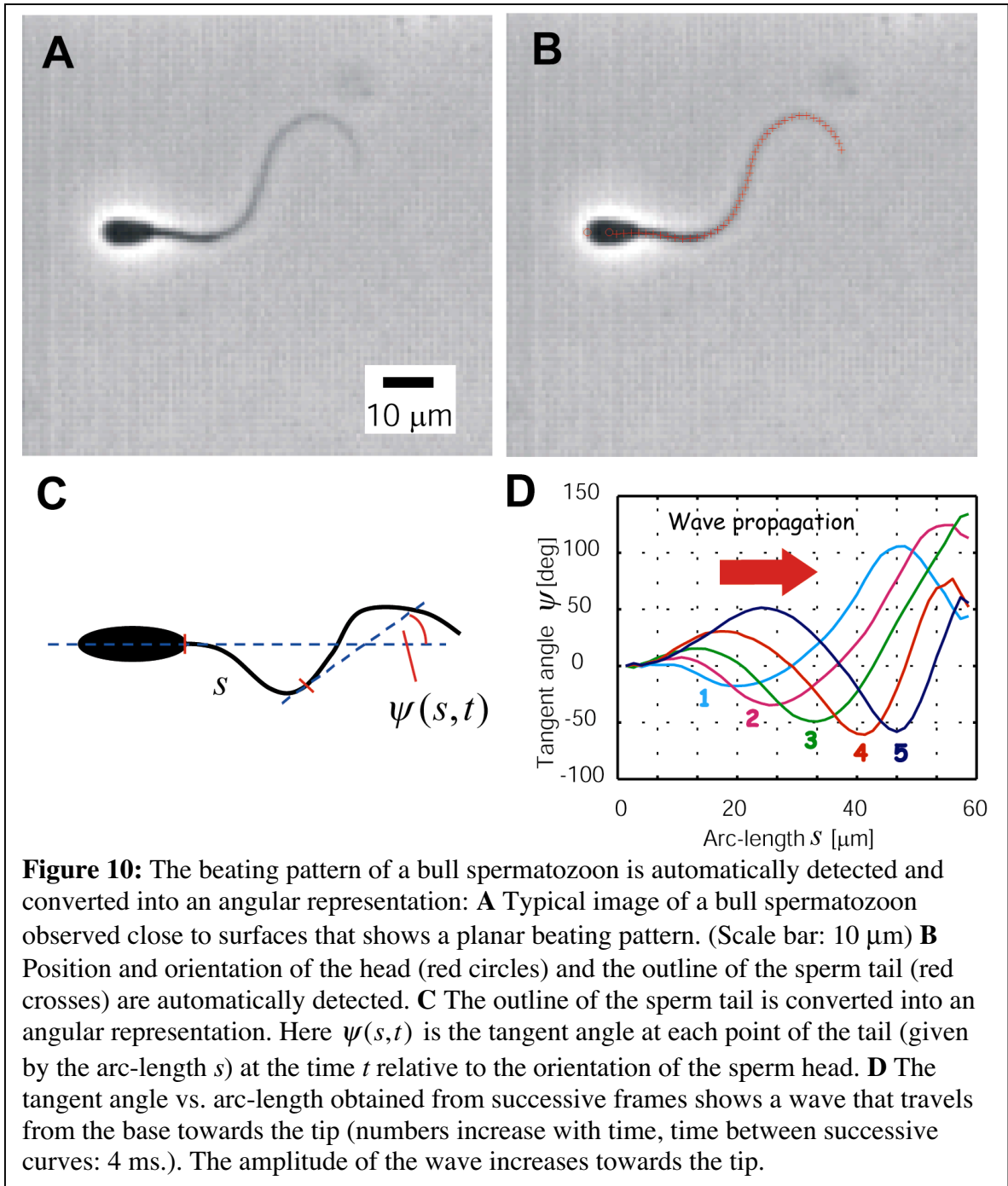
Bull sperm were obtained in frozen 100 μ l pellets from the IFN in Schönnow, kindly supplied by Karin Müller. These pellets were stored under liquid nitrogen and thawed freshly each day according to the following procedure: 0.9 ml PBSMCG-buffer (2.7 mM KCl, 1.5 mM KH_2PO_4 , 8.1 mM Na_2HPO_4 , 58.6 mM NaCl; 1 mM MgSO_4 , 2 mM

CaCl₂, 5 mM Glucose, pH=7.5) was pre-heated to 36° in a 1.5 ml Eppendorf tube. One pellet with sperm was added and the tube was incubated for 10 minutes at 36°. Then the solution was washed three times by 10 minutes centrifuging at 800 g at room temperature, discarding 0.8 ml of the supernatant and re-suspending with PBSMCG-buffer. The sperm were checked for motility under the microscope Axiovert 200M (Zeiss) in an open plastic dish in PBSMCG buffer pre-heated to 36°. Usually about 10-20% of the spermatozoa are motile (that is they survived the freezing and thawing process). Among the ones that were beating at a high frequency (20-30 Hz) one was chosen for observation. As found after analysis, these spermatozoa could differ in beat frequency, but had very similar waveforms hence this selection procedure was without loss of generality.

Spermatozoa of bull swimming freely within the liquid away from the surface show a roughly planar beat with a slight 3D component mainly at the tip-part of the tail making the bull spermatozoa rolling around their swimming path. When spermatozoa come close to surfaces they usually get trapped and follow circular swimming paths at this surface.

For obtaining high quality movies of beating spermatozoa the following procedure was used: Cover glasses No 1 1/2 18x18 mm (Corning #12520A) were cleaned by sonication in a conventional soap solution and afterwards rinsed with technical ethanol and double-distilled water. These cover glasses were either used without further treatment or were further incubated with 1% F-127 (Sigma #P-2443) in PBS (as PBSMCG but without MgSO₄, CaCl₂, and Glucose) for 5 minutes. Without F-127 treatment the spermatozoa usually stuck with their head to surface while their tails were still beating close to the surface. The heads then were either clamped or pivoting. In case of surface treatment with F-127 the sperm did not stick, instead they swam close to the surface, usually in circles of varying radii typical in the order of 40 µm. This allowed the longer observation of freely swimming spermatozoa since they did not leave the field of view. Either way, the spermatozoa were observed close to the surface and their beating pattern was roughly planar. This allowed single spermatozoa to be observed for up to 10 minutes.

I built a little metal (copper) observation chamber with diameter 12 mm and depth of 1 mm. The metal surfaces inside the chamber were sealed with conventional nail polish



to prevent potentially toxic metal ions escaping into the solution. Using conventional vacuum grease the chamber could be sealed (also quickly re-opened) on top and bottom with cover-slides that had been treated as described above. To the chamber two thermocouple-sensors Type K (Conrad #120585-49) were attached with tape and heat-paste (Conrad #189170-49) to constantly monitor the temperature with a thermometer (Voltcraft 304/K204). This chamber was mounted to a microscope heating stage (Zeiss,

Tempcontrol 37-2 digital, Universal Mounting Frame M-H) with tape and heat-paste. The metal and the small volume of the chamber allowed a quick heat-equilibration under the microscope.

Individual spermatozoa were chosen for observation. A movie at 250 fps was taken with a high-speed camera (Fastcam / Photron) lasting for 1024 frames, which is slightly more than 4 seconds and captures about 100 beat cycles. For a typical image see figure 10A.

To study the effect of viscosity I also developed a buffer by adding Ficoll 400 (Sigma, #F-4375) to the PBSMCG buffer. Ficoll 400 is a highly branched polymer, aqueous solutions of which behave as Newtonian fluids. This means that the viscosity of the fluid is independent of the velocity (magnitude and orientation). Work by other groups on increasing viscosity usually used Methyl-cellulose, e.g. (Machemer 1972). The problem with these studies is that buffers with Methyl-cellulose are not Newtonian fluids due to the long-chain-polymeric nature of this solution. I consider the use of a Newtonian fluid being of great importance since all theories assume that the drag is proportional to the velocity, furthermore that the ratio of the perpendicular and parallel drag-coefficient can be approximated by 2 (Howard 2001). The maximum viscosity at 36° that I could go to with the Ficoll buffer was limited to 10 cP, which is about 20 times that of water. Higher viscosities could not be obtained for two reasons: First, Ficoll 400 changes the refractive index of the solution hence worsening the contrast under the microscope. Second, the osmolarity of the buffer gets more unphysiological with increasing Ficoll concentration eventually immobilizing all the spermatozoa.

Viscosities were measured with a viscometer (Brookfield, Model DV-I +), where water of 36° was constantly flowing through the device to ensure to measure the viscosity at the same temperature as later within the observation chamber. The same thermocouples used at the observation chamber under the microscope were attached to the viscometer to control the temperature.

2.2.2. Wave-form detection within the movie

All movies were automatically analyzed with the detection software that I wrote in Matlab (The Math Works, Inc.). For a full description of the detection algorithm and the precision see appendix A1. At this point I only give a short summary:

The software determines in each frame the position and orientation of the head of the spermatozoon, together with the outline of the tail on 44 points (Fig. 10B). The very tip of the tail itself could not be detected directly, unfortunately, but from immotile spermatozoa I measured $L = (58.3 \pm 0.6) \mu m$ (mean and standard deviation). Hence the variation in tail-length among individual sperm is about 1%, which is fairly small. On the other hand the 41 tail-points used (the first three are still inside the head) correspond to a measured length of $L = 57.4 \mu m$, hence I miss about $1 \mu m$ of the tail. This has to be taken into account if functionals of $\psi(s)$ are computed as discussed in appendix A1.

The detected points along the tail were converted into angles relative to the head orientation $\psi(s)$ (Fig. 10C, D). Hence the center-position of the head, the orientation of the head, and the tangential angles along the tail relative to the head contain the full information about the spermatozoon that I want to obtain. Such a dataset represents the “raw data” for the succeeding work. The detection precision of the tangent angle is estimated to be $d\psi_{total} = 4^\circ$ as shown in the appendix A1.

2.2.3. Fourier analysis

Visual inspection of a beating spermatozoon under physiological conditions reveals already a very repetitive beating pattern. Following the shear angle at one point of the tail, e.g. the middle of the tail (Fig. 11A) shows a periodic, almost sinusoidal curve. This clearly suggests as a next step to perform a Fourier analysis in time on the shear angle at each point along the tail (and also on the head in cases where the head is not completely clamped to the surface). The fast Fourier-Algorithm was used in combination with a Hanning window as already implemented in Matlab.

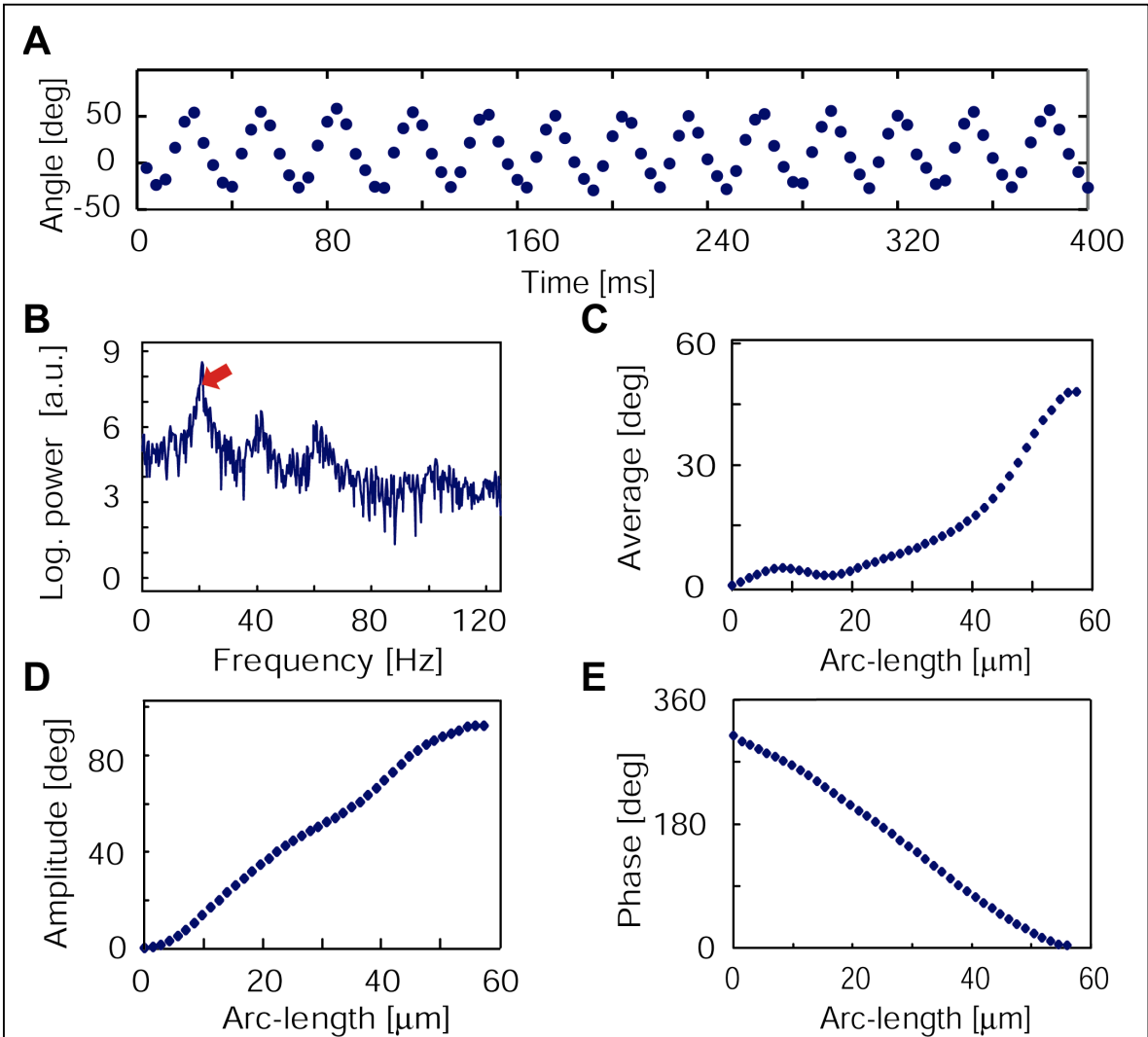


Figure 11: A Fourier analysis in time reveals that the beating pattern of a spermatozoon can be described by its first eigenmode, furthermore the waves travel with similar velocity along the whole tail: **A** The tangent angle $\psi(s,t)$ at any point of the tail shows an approximately sinusoidal form. (The presented curve was taken for a tail-position in the middle of the tail.) **B** The power spectrum of the beating pattern reveals a clear peak at a frequency of 20 Hz (red arrow). Higher modes are visible but clearly suppressed. (Note the logarithmic scale. The power spectrum displayed was computed at the same tail point as in a.) **C** The average tangent angle is different from zero and might in first approximation be described as an arc. The corresponding average curvature leads to a circular swimming path of swimming spermatozoon. **D** The amplitude of the tangent angle along the tail as obtained from the power spectrum. The relationship looks approximately linear. **E** The phase of the tangent angle along the length as obtained from the Fourier analysis changes approximately linear. This means that the wave travels with an approximately constant velocity from the base towards the tip.

2.2.4. Fitting

My goal is to test whether the theoretical framework by Camalet (Camalet and Julicher 2000) is a good description of my experimental data $\tilde{\psi}(s)$, and if not, to suggest an extension that leads to the desired agreement. To do so I fit the theoretically predicted waveforms to the experimentally measured ones.

There are different alternatives how to carry out such a fit:

First, I obtain a parameter-dependent analytical expression of the wave-solution for the given boundary conditions. Then I fit these wave-solutions to the experimental data to determine the coefficients. This is straightforward for the initial work by Camalet since there we are dealing with a linear fourth order differential equation with constant coefficients. But in the case of varying stiffness such an analytical solution is hard (may be impossible) to find therefore I did not follow this approach.

Second, I solve for a given parameter set the differential equation numerically by using a shoot-and-match routine, since the boundary conditions are given at both sides (Press, Vetterling et al. 2002). Then I optimize the agreement between experiment data and theory by searching iteratively for an optimal parameter set that minimized the root-mean-square displacement between numerical solution and experimental data. This is doable but might be complicated since there are six independent parameters in the worst case (see below) and it is not clear how smooth the corresponding six dimensional optimization space is. Hence I am dealing with a non-linear optimization problem. Although this optimization scheme might be a good strategy I choose another alternative:

Third, I can integrate the equation of motion for $\tilde{\psi}(s)$ two times while incorporating the two unknown boundary conditions that have not been checked explicitly before. (I will discuss the details below.) The corresponding relation is then fitted to the experimental data. The fitting procedure is linear hence straightforward to implement and also robust in obtaining the optimal fit.

Preparing the fit:

I integrated (eq. 28) twice and incorporate the two boundary conditions (eq. 31a, d) that I did not test so far:

$$\begin{aligned}
i\omega\xi_{\perp}\tilde{\psi}(s) &= -\partial_s^3\{(\kappa_0 + \kappa_1 s) \cdot \partial_s \tilde{\psi}(s)\} + a\partial_s^2 \tilde{f}(s) \Big| \int_0^s ds \\
i\omega\xi_{\perp} \int_0^s ds' \tilde{\psi}(s') &= -\partial_s^2 [(\kappa_0 + \kappa_1 s) \cdot \partial_s \tilde{\psi}(s)] + \partial_s^2 [(\kappa_0 + \kappa_1 s) \cdot \partial_s \tilde{\psi}(s)] \Big|_0 + a\partial_s \tilde{f}(s) - a\partial_s \tilde{f}(s) \Big|_0 \\
BC : \left\{ \partial_s^2 [(\kappa_0 + \kappa_1 s) \cdot \partial_s \tilde{\psi}(s)] - a\partial_s \tilde{f}(s) \right\} \Big|_{s=0} &= 0 \\
i\omega\xi_{\perp} \int_0^s ds' \tilde{\psi}(s') &= -\partial_s^2 [(\kappa_0 + \kappa_1 s) \cdot \partial_s \tilde{\psi}(s)] + a\partial_s \tilde{f}(s) \Big| \int_s^L ds \\
i\omega\xi_{\perp} \int_s^L \int_0^{s'} ds'' \tilde{\psi}(s'') &= \partial_s [(\kappa_0 + \kappa_1 s) \cdot \partial_s \tilde{\psi}(s)] - \partial_s [(\kappa_0 + \kappa_1 s) \cdot \partial_s \tilde{\psi}(s)] \Big|_L + \dots \\
\dots + a\tilde{f}(s) \Big|_L - a\tilde{f}(s) & \\
BC : \left\{ \partial_s [(\kappa_0 + \kappa_1 s) \cdot \partial_s \tilde{\psi}(s)] - a\tilde{f}(s) \right\} \Big|_{s=L} &= 0 \\
i\omega\xi_{\perp} \int_s^L \int_0^{s'} ds'' \tilde{\psi}(s'') &= \partial_s [(\kappa_0 + \kappa_1 s) \cdot \partial_s \tilde{\psi}(s)] - a\tilde{f}(s)
\end{aligned}$$

By carrying out the differentiation and furthermore substituting the forces for the motors according to (eq. 29) we find:

$$i\omega\xi_{\perp} \int_s^L \int_0^{s'} ds'' \tilde{\psi}(s'') = (\kappa_0 + \kappa_1 s) \partial_s^2 \tilde{\psi}(s) + \kappa_1 \partial_s \tilde{\psi}(s) - a^2 \chi \tilde{\psi}(s) + \frac{a^2 \chi^2}{i\omega\Gamma + K + \chi L} \int_0^L \tilde{\psi}(s) ds \quad (32)$$

Using this integrated equation (eq. 32) instead of equations (eq. 28, 29, 31) directly has the following advantages: First, only to a second derivative instead to a fourth one is fitted. Since higher derivatives are much more sensitive to uncertainties in the initial waveform (see appendix A1), it is important to avoid them. Second, the two boundary conditions that have not been tested so far are now incorporated into equation (eq. 32), hence I do not have to fit for the waveform and the boundary conditions in parallel. (In principle, I could even consider to integrate even two more times and impose the other two boundary conditions as well. The form of functions appearing in (eq. 28) would allow this. Whether this advantageous over the current strategy needs to be explored in the future.)

So we can rewrite (eq. 32) as

$$\partial_s^2 \tilde{\psi}(s) = \frac{i\omega\xi_{\perp}}{\kappa_0} \int_s^L \int_0^{s'} ds'' \tilde{\psi}(s'') + \frac{\kappa_1}{\kappa_0} \cdot [s \cdot \partial_s^2 \tilde{\psi}(s) + \partial_s \tilde{\psi}(s)] + \frac{\chi a^2}{\kappa_0} \cdot \tilde{\psi}(s) - \frac{A}{\kappa_0} \quad (33)$$

where

$$A = \frac{a\chi}{i\omega\Gamma + K + \chi L} \int_0^L \chi a \tilde{\psi}(s) ds \quad (34)$$

from which the amount of filament sliding $\tilde{\Delta}_0$ and the value of the visco-elastic element at the base $i\omega\Gamma + K$ then can be obtained by (eq. 22):

$$\tilde{\Delta}_0 = -\frac{A}{a\chi} \quad (35)$$

and

$$i\omega\Gamma + K = \frac{a\chi}{A} \int_0^L \chi a \tilde{\psi}(s) ds - \chi L \quad (36)$$

Note that A and χ in equation (eq. 33) are complex constants and also $\tilde{\psi}(s)$ is complex. Furthermore both sides can be divided by $i\omega\xi_{\perp}$, hence I find six independent constants that need to be determined in a fit.

Strategy of fitting:

Since I want to test the possible influence of a visco-elastic element at the base, as well as the influence of varying stiffness along the length, I carry out four different fits that include none, one, or both of these influences by setting A and / or κ_1 to zero.

I chose movies of five different bull spermatozoa that were clamped at their heads and were beating at (20 ± 1) Hz (mean \pm Std). Their beating patterns looked very similar. From their Fourier averaged waveforms I computed the different functionals in $\tilde{\psi}(s)$ that show up. Furthermore I determined the uncertainties in these functionals according to appendix A1.

For the fit I only used the points within the bulk of $\tilde{\psi}(s)$; that is, I omitted the first and last three points of $\tilde{\psi}(s)$. The reason is that the error of the derivatives at the ends get very large (see appendix A1) while inside the bulk the error is smaller and everywhere the same. Since these end pieces contain only a small part of the available information on the waveform it is convenient to omit them, which allows the usage of a simpler fitting procedure since consequently the uncertainty is the same at every data point.

I did a linear least-square fit that reveals the three to six fit parameters (depending on the fit) including their uncertainties. Furthermore the root-means-squared error and the

goodness of fit were determined (chi-squared test). All five samples behaved very similar in the different fits. Hence from all five samples for all parameters weighted averages and standard error of the mean (SEM) were computed (Young 1962).

2.3. Experimental results: Waveforms

I obtained four different kinds of data sets: Spermatozoa where the head is clamped at the surface, where the head is fixed at the surface but is able to pivot, forward-swimming spermatozoa, and finally I also observed forward-swimming spermatozoa at higher viscosities due to the addition of Ficoll. Since the Ficoll prevents sticking of the spermatozoon to the surface it was not possible to observe spermatozoa with clamped or pivoting heads at higher viscosity. For all waveforms the wave was always traveling from the base towards the tip of the tail in contrast to the results of the theoretical work by Camalet who predicted that in the case of a clamped head the wave should travel towards the head. Generally, I find that the waveforms look similar for the different boundary conditions (data not shown), but the different fixation conditions of the head lead to different sliding amplitudes close to the head. Furthermore for higher viscosity the wavelength decreases. In the following discussion I restrict myself to the analysis of the case of the clamped head, the other cases still await analysis at the time of writing up this thesis.

The Fourier analysis of these waveforms revealed clear peaks at the main frequency and its higher harmonic (Fig. 11B). It was found that at least 95% of the power in the Fourier spectrum was contained within the first mode at the tip of the tail. This power increased towards the base. Since the power is $|\psi_1(s)|^2$, these 95% correspond to about 2.5% loss in $\psi_1(s)$ compared to the total amplitude $\psi(s)$ at the end of the tail but less loss at other parts. These 10% are still reasonably small enough to argue that the beating pattern is essentially captured by the first eigenmode.

Hence I can conclude that $\psi(s)$ for any given s changes nearly sinusoidal in time. The higher modes only lead to smaller corrections and consequently all further analysis is only executed at the lowest Fourier-mode. At lower beat-frequencies - achievable for instance at lower (un-physiological) temperatures - the spermatozoon beats slower and

more erratic and consequently these higher modes gain in relative contribution and this approach might not be suitable any more. I used only those spermatozoa for analysis that were beating at frequencies close to 20 Hz, which showed negligible higher modes.

Restricting myself to the first mode is also a valid approach if one wants to compare the data to theoretical predictions. Most theoretical analyses make use of the Fourier-ansatz to solve some nonlinear differential equations, which then in turns leads in its first order approximation to some statement about the shape of exactly this lowest mode. Furthermore, each Fourier-mode itself has to satisfy the boundary conditions on its own. Taking all these facts together it is certainly justified to deduce only the lowest Fourier-mode for further analysis from the data, although the higher modes are always experimentally accessible if necessary. The following discussion focuses only on this first Fourier mode. Hence the index of $\tilde{\psi}_1(s)$ is dropped and $\tilde{\psi}(s)$ refers to this mode if not explicitly stated differently.

Furthermore, the power spectrum also leads to the beat-frequency f and its fluctuations df , where df is the standard deviation of a Gaussian fitted to the first peak in the power spectrum. For a spermatozoon beating at $f = 21\text{Hz}$ I found $df / f = 0.05$. Defining the Quality factor as $Q=f/(2df)$ we find $Q=10$. This is a lower estimate since there could be undetected drift in the frequency over the observation time.

Figure 11C shows the amplitude of the zero eigenmode $\psi_0(s)$ that is an average curvature that is superimposed on the beating axoneme. This average curvature leads to a circular swimming path of the spermatozoon near surfaces. The theory presented by Camalet does not make any statement about such a feature. Obviously, some time independent asymmetric force is needed to bend the axoneme on average towards one side. It is known that such an average curvature can be induced or totally prevented or even modified bio-chemically, e.g. with Ca^{2+} (Brokaw and Nagayama 1985). Furthermore it is known that such changes in curvature allow a spermatozoon to move towards a chemo-attractant, usually stemming from the egg, in a spiraling random walk like fashion (Kaupp, Solzin et al. 2003). These facts make it clear, that such an average curvature involves some more complicated regulatory mechanism and is not an essential feature related to the axonemal beat. Since the scope of this work is to understand how collective

motors give rise to the oscillatory beating pattern of an axoneme, I do not investigate this subject further and also neglect this average curvature in the following discussion.

The amplitude $|\tilde{\psi}(s)|$ and phase $e^{i\varphi(s)}$ of the first eigenmode $\tilde{\psi}(s) = |\tilde{\psi}(s)|e^{i\varphi(s)}$ are shown in figures 11D and 11E. I find a surprisingly linear relationship for both of them. This almost linear phase relation means that the waves are traveling with an almost constant velocity from the base towards the tip of the tail and that the waveform can be approximated by a sine-wave with increasing amplitude: $\psi(s,t) = A \cdot s \cdot e^{-i2\pi s/\lambda} e^{i2\pi ft}$, with approximate values $A = 1.8^\circ / \mu m$, $\lambda = 63 \mu m$, and $f = 21 Hz$. (At this point I only give a qualitative picture. The appropriate fitting to a theoretical description including an error analysis is given in the following section.) I point out that this form is clearly an approximation, especially at the boundaries, which will become very important from a theoretical perspective as we will see later. Furthermore, looking at equivalent data in other species, e.g. the waveform $\psi(s,t)$ of *Ciona* spermatozoa (Brokaw 1993) I find a very sinusoidal waveform as well but where the amplitude stays rather constant and hence the wave can be approximated by $\psi(s,t) = A \cdot e^{-i2\pi s/\lambda} e^{i2\pi ft}$. Hence the waves on a spermatozoon in general travel with a constant velocity along the tail. The varying amplitude along the tail in the case of bull spermatozoa is very likely a secondary effect due to the change of the flexural rigidity along the tail. This leads to the hypothesis that the velocity of the traveling wave is in first approximation independent of the flexural rigidity of the axoneme, at least for typical parameter choices.

Using the functions $|\tilde{\psi}(s)|$ and $e^{i\varphi(s)}$ from this Fourier averaged data I can also obtain an averaged waveform, which is plotted for successive time steps in figure 12A. Comparing this to figure 10D we see the correspondence, but the averaged curve is smoother and more precise. As discussed in the appendix A1 the Fourier analysis increases the precision of the measured angles to $d\psi_{total} = 0.4^\circ$, corresponding to a precision in sliding displacement of about 1 nm from the relation $\Delta = a\psi$.

This high precision compared to data obtained earlier by other groups now allows the computation of various functionals in $\psi(s)$ with a reasonable error. This high precision is important, since especially the derivatives $\partial_s^n \psi(s)$ increase in their

uncertainty with increasing n . Furthermore the derivatives at the boundaries have a larger uncertainty than the ones for the bulk, which is summarized in appendix A1. Since the theory given by equations (eq. 28-31) explicitly depends on the 4th derivative it is important to be able to measure the waveform with a high precision.

2.4. Fit results: Test of a generic description

Now I test whether the analysis presented by Camalet (Camalet and Julicher 2000) can be brought into agreement with the experimental data. I chose 5 data sets where the head of the spermatozoon was clamped and that were beating at about 20 Hz. The waveforms of these 5 sets were very similar in appearance, and lead to the very similar fitting parameters and goodness of fits. Hence I am convinced that the conclusions drawn are robust. Furthermore we will see, that the original theory by Camalet is in contradiction to the experimental data. But considering an additional visco-elastic element at the base of the axoneme not included in the original description by Camalet I find a good agreement. Varying the stiffness of the axoneme along its length is also considered, but this, by itself, is not sufficient to account for the discrepancy.

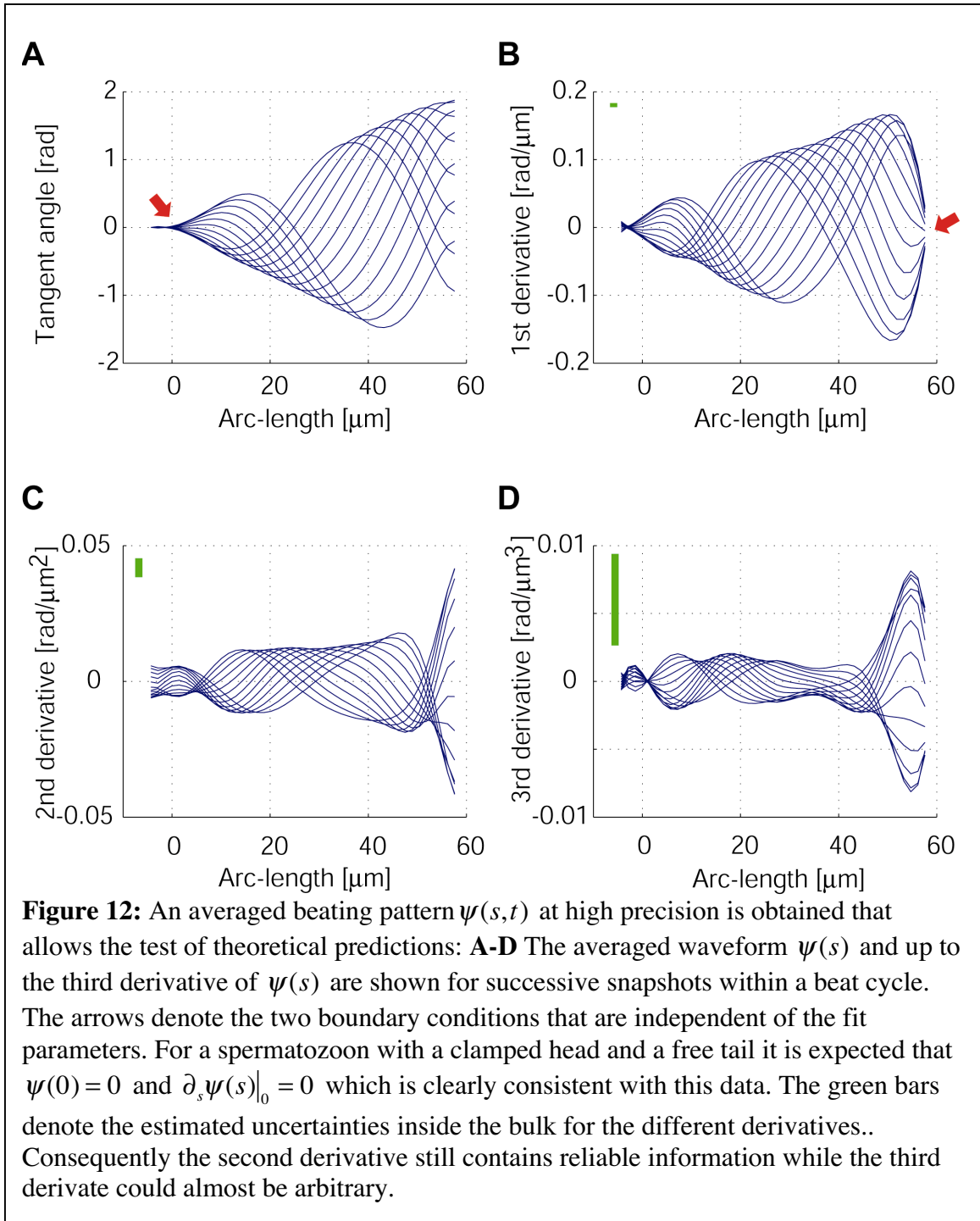
2.4.1. Testing two boundary conditions

First I check whether the experimental boundary conditions are in agreement with the theoretical assumed ones. Figure 12 shows the waveform $\tilde{\psi}(s)$ and the first three derivatives, which are the ones entering the boundary conditions (eq. 31a-d). Two of the boundary conditions can be tested directly without knowing any of the actual parameters determining the beat. They only contain $\tilde{\psi}(s)$ and the derivative of $\tilde{\psi}(s)$ respectively and both of them are zero.

Both relations are zero can be read off from figure 12A, B. Furthermore I can test these relations from the actual data and the error analysis in appendix A1. I find

$$\tilde{\psi}(0) = [(-0.07 \pm 0.09) + i(-0.26 \pm 0.12)]^\circ \quad (37)$$

$$\partial_s \tilde{\psi}(s)|_L = [(-0.11 \pm 0.4) + i(0.11 \pm 0.5)]^\circ / \mu m \quad (38)$$



where the values are given as mean and standard error of the mean (SEM). Since both values are expected to be zero I should find that the means are not significant from zero that is similar to the SEM. This is the case.

Furthermore I can compare the SEM obtained from the 5 data sets with what I expect from the measurement uncertainties estimated in appendix A1: For $SEM(\tilde{\psi}(0)) = 0.4^\circ / \sqrt{5} = 0.2^\circ$ and $SEM(\partial_s \tilde{\psi}(s)|_{s=L}) = 1.4^\circ / \mu\text{m} / \sqrt{5} = 0.6^\circ / \mu\text{m}$. These values are similar to the SEM in (eq. 37, 38) indicating that my error estimation in appendix A1 is reasonable.

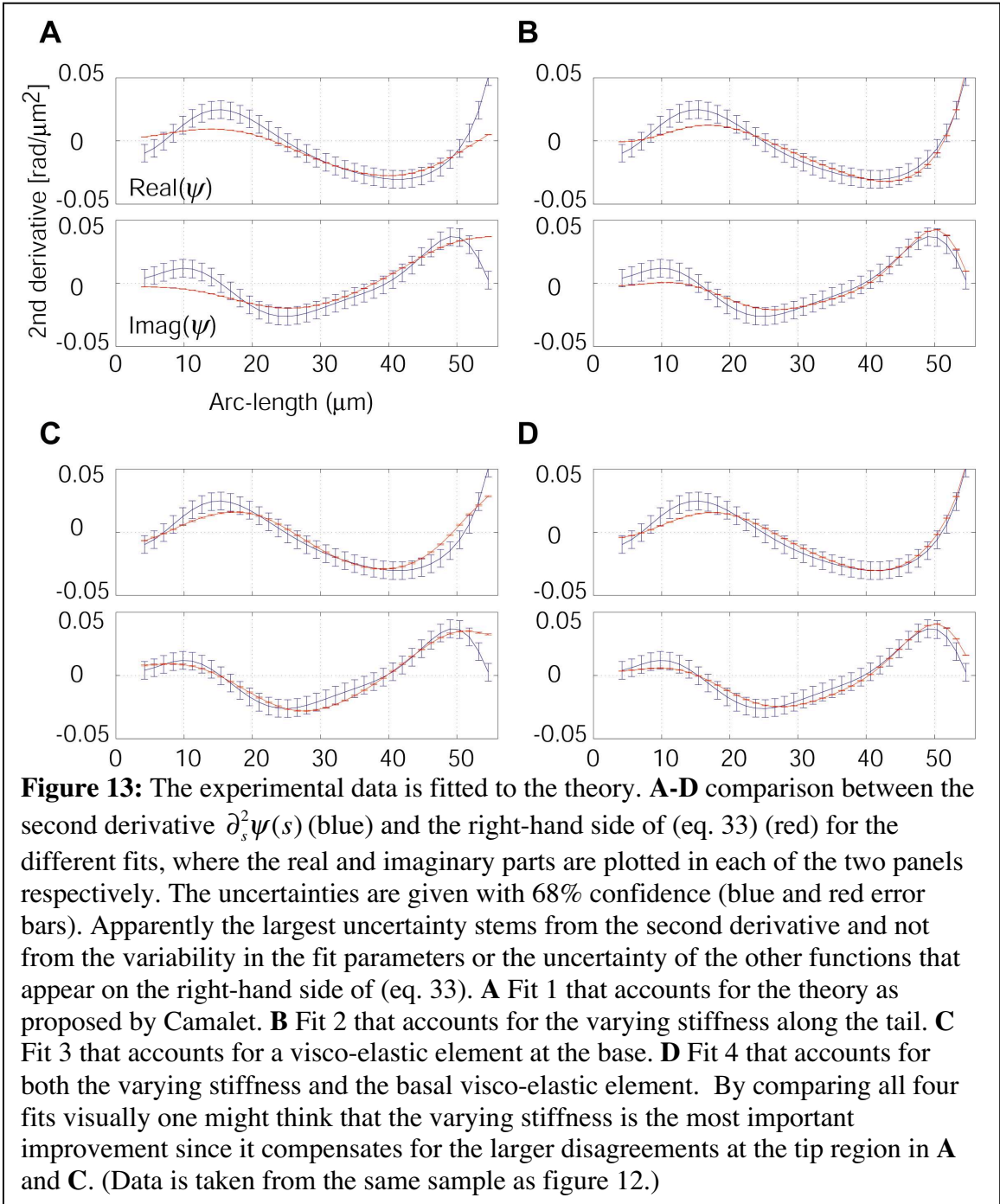
The other two boundary conditions depend on the actual parameters determining the forces and the torques at the base and the tip. Since I first have to obtain these parameters from fitting the theory to the experimental data I will come back to this issue in a later subsection.

2.4.2. Fit results

As discussed earlier I carry out four different fits where I fit the second derivative $\partial_s^2 \tilde{\psi}(s)$ according to (eq. 33). These fits include the original work presented by Camalet, additionally the effect of linearly decreasing flexural rigidity or a basal viscous element or both effects at once. Figure 13 shows the real and imaginary part of $\partial_s^2 \tilde{\psi}(s)$ (blue) and the corresponding fits (red) for one of the five samples. The uncertainty in $\partial_s^2 \tilde{\psi}(s)$ and the uncertainties in the fit are given as error-bars with 68% confidence level. By a chi-square test I find that the first fit is not in agreement with the experimental data while the others are. Actually, the agreement is already too good, indicating that either the measurement uncertainties were overestimated, or that the theory contains too many free parameters in comparison to the information content of the data.

The fit parameters are ratios of the different observables (eq. 33) that I am really interested in. To obtain these observables I have to fix the spacing between two microtubule-doubles, which was chosen to $a=60$ nm (Howard 2001). Furthermore I need to fix one additional parameter that enters (eq. 33), where I chose friction coefficient $\zeta_\perp = 2.5$ mPas. The significance of the different fits, the fitted observables und the expected values for these observables are summarized in Table 1. (How to determine these expected values I will discuss in the following subsection.)

Comparing the values of the observables to the expected ones I find a negative flexural rigidity and a fully positive response for fit 1, which is unphysical. Hence I



conclude that the original description by Camalet is not sufficient to account for the experimental observation on bull spermatozoa. This is also supported by the prediction that the wave travels from the base towards the head, while I see exactly the opposite in the experiment.

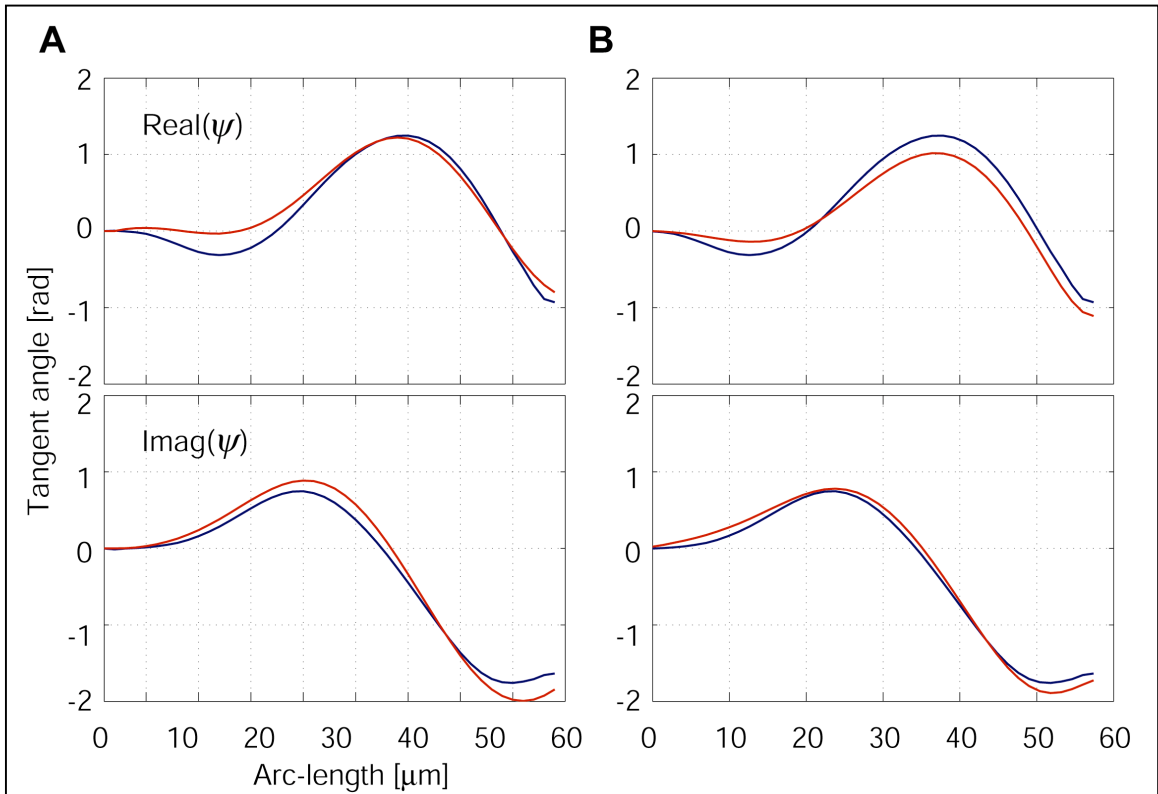


Figure 14: The fitted waveforms $\tilde{\psi}(s)$ are in good agreement with the experimental data. The experimental data (blue) is compared the fit results (red). The theoretical $\tilde{\psi}(s)$ was obtained by integrating the fitted second derivative $\partial_s^2 \psi(s)$ (see Fig. 13 C, D) two times and applying the boundary conditions $\psi(0) = 0$ and $\partial_s \psi(s)|_0 = 0$. **A** Fit 3 that accounts for a basal visco-elastic element. **B** Fit 4 that accounts for a basal visco-elastic element and the varying stiffness along the tail. Both fits show a good visual agreement. (Data is taken from the same sample as figures 12 and 13.)

In fit 2 I accounted for a linearly varying flexural rigidity along the length as has been measured for bull spermatozoa by (Lindemann, Rudd et al. 1973). Again I find unphysical values at least for the flexural rigidity. Hence this description fails as well.

Alternatively I considered in fit 3 that one of the boundary conditions might be different from what as originally been assumed. The general assumption is that the microtubules are rigidly connected at the base of the axoneme to prevent any filament sliding there. But it was shown recently that at least for mammalian spermatozoa sliding takes place at the base (Vernon and Woolley 2004). Consequently I assumed a visco-elastic element being present at the base that allows this filament sliding. From the table we can read off that all parameters have the expected sign, furthermore they are all in the correct order of magnitude, although the viscous part of the basal element seems quite

high. The values for all observables obtained from the different samples agree with each other within their uncertainties. Hence I conclude that fit 3 is a valid description for the experimental data.

In fit 4 the effect of the varying stiffness and the basal visco-elastic element are combined. The flexural rigidities are too high, the other parameters agree with the expectations. But we also note that the uncertainties for these observables are often higher than the mean, furthermore that the values obtained from the different samples do not agree with each other within their uncertainties. This indicates that there are too many free parameters that cannot be deduced independently from the experimental data. I conclude that introducing the effect of linearly varying stiffness is expected to lead to a quantitative improvement for the description of the beating pattern of the bull spermatozoon but the data analyzed so far is not sufficient to fully support this conclusion.

As a final control I compare the results from fit 3 and 4 directly with the original data. To do so I integrate the fitted second derivate two times $\partial_s^2 \psi(s)$ by using the boundary conditions $\partial_s \psi(s)|_{s=L} = 0$ and $\psi(0) = 0$. (I had to adjust the first integration constant to obtain the final agreement, which is reasonable to do due to measurement and fitting uncertainties.) The results are shown in figure 14 and I find a very good agreement.

Parameter	Symbol	Fit 1	Fit 2	Fit 3	Fit 4	Expected value
RMSE (fit) (10^{-3})		5.2±3.2 *	1.9±1.6 *	3.5±0.7 *	1.6±0.2 *	-
Beat frequency (Hz)	$\omega = 2\pi f$	131±5 *				-
Drag coefficient (10^{-3} Pas)	ξ_{\perp}	2.5				2.5
Flexural rigidity base (10^{-21} Nm ²)	κ_0	-(88±10) §	-(69±17) ‡	3.6±0.2 ‡	19±7 §	4.0
Flexural rigidity change per unit length (10^{-15} Nm)	κ_1	-	-(1.2±0.7) §	-	-(0.32±0.11) §	-0.056
Elastic response (10^3 N/m ²)	Re(χ)	260±30 ‡	(42±14) ‡	-(19±1) ‡	-(17±5) ‡	-30
Viscous response (10^3 N/m ²)	Im(χ)	54±15 ‡	-(18±8) ‡	-(12±1) ‡	-(10±3) ‡	-50
Spring at base (N/m)	K	-	-	(4±1) ‡	-(11±17) ‡	2
Friction at base (N/m)	$\omega\Gamma$	-	-	(12±1) ‡	(12±18) §	2
Displacement at base (10^{-9} m)	$ \tilde{\Delta}_0 $	-	-	(66±5) ‡	(82±27) ‡	50

Table 1: Comparison of fit parameters and their expected values for the different fits. **Fit 1** corresponds the description suggested by Camalet (Camalet and Julicher 2000), **Fit 2** additionally includes varying stiffness along the length of the axoneme, **Fit 3** accounts for a visco-elastic element at the base of the axoneme, and **Fit 4** includes both the terms from Fit 2 and 3.

* mean ± Std (n=5)

§ Values from the different samples are within 95% confidence not consistent with each other, hence given as mean ± Std (n=5)

‡ Values from the different samples are consistent, hence given as mean ± SEM (SEM computed by weighing the individual uncertainties according to (Young 1962)) (n=5)

2.4.3. Estimation of the fit parameters

In the following I want to discuss how the parameters obtained from the fits can be estimated, some of them even have been measured. I also discuss whether the fit parameters are reasonable, especially for fit 3 and 4 since the other two fits have already been rejected as discussed before.

Friction per unit length: The friction coefficient for a cylinder close to a surface can be estimated as $\xi_{\perp} = 4\pi \cdot \eta / \ln(2h / r)$ (Howard 2001), where h is the distance between center of the cylinder and the surface, r is the radius of the cylinder and $\eta = 0.5$ mPas is the viscosity of water at 36° C. Given the thickness of the head by $5 \mu\text{m}$ (Brennen and Winet 1977), the radius of the tail at the base with $r=1 \mu\text{m}$ and at the tip $r=0.1 \mu\text{m}$ I assume an average radius $r=0.5 \mu\text{m}$ and an average distance from the surface $h=3$. I find $\xi_{\perp} = (2.5 \pm 1)$ mPas, where the uncertainty was estimated from higher or lower friction at the base and tip respectively.

Flexural rigidities: The flexural rigidity for the basal part of a bull spermatozoon has been measured to be $\kappa_0 = 4 \cdot 10^{-21}$ Nm² (Lindemann, Rudd et al. 1973). The distal flexural rigidity can be assumed to be the same as the one of a pure axoneme, which has been measured to be $\kappa = 0.7 \cdot 10^{-21}$ Nm² (Okuno and Hiramoto 1979). Assuming that the flexural rigidity varies linearly along the length I find a changing rate per unit length of $\kappa_1 = (\kappa - \kappa_0) / L = -56 \cdot 10^{-18}$ Nm where $L = 60 \mu\text{m}$.

I find that for fit 3 the flexural rigidity is in full agreement while for fit 4 both values κ_0 and κ_1 are higher than expected. Since both are influenced from the choice of the friction per unit length ξ_{\perp} but their ratio is not, it is informative to compare this ratio as well to the expected value. I find $\kappa_0 / \kappa_1 = -6 \cdot 10^{-5} / \text{m}$ compared to the expected value of $\kappa_0 / \kappa_1 = -7 \cdot 10^{-5} / \text{m}$, which is only about 15% difference. I conclude that at least the ratio κ_0 / κ_1 of the flexural rigidities as revealed by fit 4 is very reasonable.

The internal effectively active linear response χ : As discussed (eq. 30) the internal effective active response is due to the active motors $F(\Omega, \omega)$ and the passive visco-elastic elements, such as protein friction λ and the stretching of nexin links k :

$\chi(\Omega, \omega) = k + i\lambda\omega + F(\Omega, \omega)$. The linear response for a certain two-state motor model

(Julicher and Prost 1997) then is $F(\Omega, \omega) = -\rho \frac{U}{l^2} \frac{2\pi^2\beta}{\alpha} \cdot \frac{i\omega / \alpha + (\omega / \alpha)^2}{1 + (\omega / \alpha)^2}$. In the

following I discuss each of the terms separately:

Internal elasticity per unit length k : The microtubule doublets are connected by stretchable elements called nexin links (Warner 1976; Gibbons and Gibbons 1980). This elasticity density has been measured by (Minoura, Yagi et al. 1999) to be

$k = (2.0 \pm 0.8) \cdot 10^3 N / m^2$ (mean \pm StD). From the typical cross-bridge elasticity

$k_B = 5 \cdot (10^{-4} - 10^{-3}) N / m$ (as for Myosin or Kinesin (Howard 2001)) and the typical nexin density (Minoura, Yagi et al. 1999) $\rho_p = 95 / \mu m$ I find a higher value of

$k = 5 \cdot (10^4 - 10^5) N / m^2$. Since the motors can be assumed to be typically stiffer and also not as stretchable as the nexin links, the later value is an overestimation, hence the value of $k = (2.0 \pm 0.8) \cdot 10^3 N / m^2$ is reasonable and presumably mainly due to the nexin links.

Internal friction per unit length $\omega\lambda$: The internal friction is due to fluid and protein friction. Assuming for the fluid friction the viscosity of the cytosol $\lambda = 0.1$ Pas being 100 times higher than that of water, furthermore the sliding of $N=10$ filaments I find $\lambda \approx 2\pi N\eta = 6$ Pas (Howard 2001). Protein friction in contrast is given by the rupturing of attached proteins, in that case nexin links for instance, which have been observed to detach and reattach periodically during the axonemal beat. The resulting protein friction then would be $\lambda = pk_B\tau_{on}\rho_p = 50$ Pas. Here $p \approx 1$ is the fraction of time the nexin spends attached (were I assume that these nexin links are attached most of the time), the stiffness of the molecular bond of the nexin links k_B and the nexin density ρ_p are determined by $k = k_B\rho_p = 2.0 \cdot 10^3 N / m^2$ as discussed before (Minoura, Yagi et al. 1999)). Finally I assume the rate of detachment $1 / \tau_{on} \approx 40$ Hz that is each nexin link gets ripped of two times per cycle for a beat frequency of the spermatozoon of $f = 20$ Hz. Hence I find that protein friction dominates over fluid friction. The passive viscous response then is $2\pi f\lambda = 6 \cdot 10^3 N/m^2$.

Linear response of the motors themselves $F(\Omega, \omega)$: The linear response of the motors can be estimated from $F(\Omega, \omega) = -\rho \frac{U}{l^2} \frac{2\pi^2 \beta}{\alpha} \cdot \frac{i\omega / \alpha + (\omega / \alpha)^2}{1 + (\omega / \alpha)^2}$ by assuming a motor density $\rho = 500 / \mu\text{m}$, the energy scale $U = 5 \cdot 10^{-20}$ J as being half the free energy available from an ATP-molecule within the cell, $l = 8$ nm as the step-size of the motor, the on- and off-rates of the motors $\beta = 10$ /s (Shiroguchi and Toyoshima 2001) and $\alpha = 300$ /s (Kamimura and Kamiya 1989), and the beat-frequency of the spermatozoon $\omega = 2\pi f = 126$ Hz I find $F(\Omega, \omega) = -(3 + 6i) \cdot 10^4$ N/m². This value is reduced by a factor of 4 if the step-size is 16 nm instead of 8 nm (Burgess, Walker et al. 2003).

Summary internal effective active response: Putting the passive and active internal response together I find $\chi(\Omega, \omega) = -(3 + 5i) \cdot 10^4$ N/m² where the active parts dominate. Since all four values are within the same order of magnitude the real and imaginary part of $\chi(\Omega, \omega)$ can easily switch from negative to positive for lower ATP-concentrations, leading to a transition from oscillatory to non-oscillatory state as proposed (Julicher and Prost 1997).

From the present experiment it is not possible to discriminate between the active and passive response. This suggests an experiment to observe spermatozoa beating at different frequencies, e.g. due to varying the ATP-concentration, which keeps the passive components k and λ constant but influences the rate constants β and α .

Finally I note that the estimated responses are in reasonable agreement with what I measured from fitting my experimental data for fit 3 and 4.

Visco-elastic element at the base: I notice from table 1 that for fit 3 the visco-elastic element at the base is purely passive due to the positive signs. Within uncertainties the same can be said about fit 4. This is very important since there is no experimental indication for any additional active element at the base. Furthermore I see that the viscous element dominates the elastic one for fit 3.

To estimate the elastic part I assume a protein structure consisting of 10 microtubule doublets ranging over $l = 5 \mu\text{m}$. The elastic modulus then is $E = 2 \cdot 10^9$ N / m² (Howard 2001) with the cross-sectional area of a microtubule-doublet of $A = 400$ nm² leading to $K = 10EA / l = 2N / m$.

To estimate the passive friction at the base I again consider a region of $l=5 \mu\text{m}$. I assume that the friction is due to protein friction, and in this case not only due to the nexin links but also to the much stiffer dynein motors that are presumably stalled in this region due to the high built-up force in this basal region. Hence using the internal friction per unit length $2\pi f\lambda = 6 \cdot 10^3 \text{ N/m}^2$ as estimated above but correct with a factor of 5 for the higher protein density ($95 / \mu\text{m}$ for nexin links and $500 / \mu\text{m}$ for dynein) and with another factor of 10 for the much stiffer dynein. I find $\omega\Gamma = 50\omega\lambda l = 2 \text{ N/m}$.

Hence I conclude that both the elastic and the viscous element are in the order of magnitude of what I determine from the fit. While the elastic element agrees very well, the viscous element obtained from the fits (especially fit 3) seems to be too high, also given that the viscous element might be already overestimated. One solution to this discrepancy is that the total number of molecules that get ruptured in this region is higher due to other proteins.

The displacement at the base: It has generally been assumed that the microtubules are so rigidly attached at the base such that no filament sliding is possible there. This has also been shown directly in the case for the case of sea urchin and tunicate spermatozoa (Brokaw 1991). In contrast it was shown very recently in the case of mammalian spermatozoa (*Chinchilla*) (Vernon and Woolley 2004) that there is sliding at the base. It is reasonable to assume that the value for a bull spermatozoon is similar. A reason for the difference between sea urchin and mammalian spermatozoa is that in the case of mammalian spermatozoa the microtubules are not attached at the basal body. For a basal diameter of 450 nm the sliding amplitude was 85 nm, leading to a sliding amplitude of $|\tilde{\Delta}_0| = 10 \text{ nm}$ in the case of two neighbored microtubules that are spaced apart by 60 nm. This is in the order of magnitude I obtained from the fit but still too small. Note that the displacement at the base does not scale with the chosen value for friction ξ_{\perp} since it cancels in the ratio A / χ . Hence this value is entirely determined by the fit and the given microtubule-doublet separation a .

Besides this effect seen directly by Vernon (Vernon and Woolley 2004) I can also estimate by what amount the microtubule doublets may get compressed in the basal region. As discussed before, I find for the basal region an elasticity of

$K = 10EA / l = 2N / m$. Hence if I want to compress these 5 μm by 50 nm, that is 1%, I need a force of $F_C = K \cdot \Delta l = 100$ nN. This force has to be generated by more distally motors over a length ΔL . I find $\Delta L = F_C / (\rho \cdot F_M) = 40 \mu\text{m}$ where $\rho = 500 / \mu\text{m}$ is the motor density and $F_M = 5$ pN is the maximum force per motor. Hence ΔL is in the order of the length of the sperm tail hence it is perfectly reasonable that the microtubule-doublets get compressed in the basal region by 50 nm.

2.4.4. Testing the other two boundary conditions

Now I can test for fit 3 and 4 whether the other two boundary conditions (eq. 31a,d) are satisfied as well.

I find for fit 3

$$\left\{ \kappa_0 \partial_s^3 \tilde{\psi}(s) - a^2 \chi \cdot \partial_s \tilde{\psi}(s) \right\} \Big|_{s=0} = [-(0.12 \pm 0.05) + i(0.03 \pm 0.10)] \cdot 10^{-3} \text{rad} \cdot N / m \quad (39)$$

$$\left\{ \kappa_0 \partial_s^2 \tilde{\psi}(s) - a^2 \chi \cdot (\tilde{\psi}(s) + \tilde{\Delta}_0 / a) \right\} \Big|_{s=L} = [(0.11 \pm 0.21) - i(0.13 \pm 0.16)] \cdot 10^{-9} N \cdot \text{rad} \quad (40)$$

and for fit 4

$$\left\{ \kappa_0 \partial_s^3 \tilde{\psi}(s) + 2\kappa_1 \partial_s^2 \tilde{\psi}(s) - a^2 \chi \cdot \partial_s \tilde{\psi}(s) \right\} \Big|_{s=0} = [(6 \pm 13) + i(14 \pm 15)] \cdot 10^{-3} \text{rad} \cdot N / m \quad (41)$$

$$\left\{ (\kappa_0 + \kappa_1 L) \cdot \partial_s^2 \tilde{\psi}(s) + \kappa_1 \partial_s \tilde{\psi}(s) - a^2 \chi \cdot (\tilde{\psi}(s) + \tilde{\Delta}_0 / a) \right\} \Big|_{s=L} = \\ = [(0.02 \pm 0.50) + i(0.49 \pm 0.49)] \cdot 10^{-9} N \cdot \text{rad} \quad (42)$$

The values were obtained as averages of the five samples, together with the SEM. I conclude that all relations are not significant from zero; that is, the boundary conditions are satisfied by both fits.

I note that the measurement uncertainties of the higher derivatives at the boundaries are very large, that is the ratio between the uncertainty and the maximal expected value is larger than one (see appendix A1). Additionally the uncertainties in the fit parameters come into play. For fit 4 they are also very large (table 1). Therefore it is questionable whether my actual measurements contain more information than choosing an arbitrary but realistic value. Nevertheless, it is comforting that the boundary conditions

are consistent with the expectations. Although I might not have expected a disagreement (because I constrained these two boundary conditions by the way I set up my fitting procedure) it could have turned out that the theory might have been in such disagreement with the data that no reasonable fit could have been achieved.

I conclude that these two theoretically assumed boundary conditions are not in disagreement with the experimental data.

2.4.5. Summary

To summarize I find that the theoretical framework by Camalet in its original form is not sufficient to account for the experimentally obtained waveforms on bull spermatozoa. Considering linearly varying flexural rigidity along the tail cannot correct for this failure. But introducing a visco-elastic element at the base leads to a very good agreement. All parameters deduced from the fits are in agreement with what can be expected. The only surprise is the rather large viscous element at the base that seems to even dominate over the elastic properties in this region. Additionally to the basal visco-elastic element, I also considered the varying stiffness along the tail. It leads to a reasonable fit as well, while some of the parameters agree only within the order of magnitude with the expectations. The improvement is not substantial. It seems that there are too many free parameters to be sufficiently constrained by the data.

I found that all four theoretically assumed boundary conditions are in agreement with the experimental data. Two of them can be solidly tested within the measurement uncertainties and are also independent from the fits. While $\tilde{\psi}(0) = 0$ is quite obvious, the condition for zero curvature at the tip $\partial_s \tilde{\psi}(s)|_L = 0$ has not been explicitly measured before to my knowledge. Hence it represents a new result, which was only possible due to the high measurement precision. No curvature at the tip means that no torque is acting there, indicating that the filaments are really free to slide at the tip. For the other two boundary conditions the uncertainties of the measurement and also fit parameters are too large to being actually able to disprove them, but it was useful to show that they do not give rise to disagreement.

The presented results and conclusions are of reasonable conciseness to stop the analysis at this point. But this is certainly work in progress and more work needs to be

done. On one hand I want to consider alternative fitting strategies as discussed earlier to have an independent control. It would be especially desirable to show that solving the original equations (eq. 28-31) with the obtained parameter set leads to a solution that agrees with the experimental data. The other open work concerns the analysis of the other data sets that is waveforms for other boundary conditions and at increased viscosity. I hope that I obtain consistent parameter sets from these fits.

2.5. Discussion and conclusions

I want to summarize and discuss my achievements. These are on one hand the development of a waveform detection and analysis tool. On the other hand I was able to test a theory and suggest an extension to bring this theory in agreement with the experimental data. Finally I suggest an experimental scheme to address open question.

2.5.1. The new waveform detection tool

I developed a new and automated tracking system for the beating pattern of planar beating spermatozoa that can be used in combination with a high-speed digital camera and Fourier analysis, leading to a very high spatial and temporal precision in the waveforms. Sperm waveform detection softwares have been developed before (Brokaw 1984) and correspondingly waveforms have been published before (Brokaw 1996). In these studies usually not more than one beating cycle was analyzed leading to less precision I obtained. I can now automatically detect such a waveform in about 30.000 successive frames, being only limited by the capabilities of the camera.

This new tool has the advantage that it leads to a very increased precision, which enabled me to measure also the derivatives of the waveform with respect to the arc-length. Therefore I was able to make rigorous statement about the boundary conditions, especially to show that the curvature at the tip of the tail is zero as predicted. Furthermore the data can be used to fit it to different theoretical predictions.

This new tool also allows the study of beating patterns that are not periodic by taking much longer time series. Such non-periodic beating patterns can typically be found in unphysiological conditions compared to the ones at which the spermatozoa usually operate, for instance at decreased temperatures. But I expect that exactly these rather

stochastic looking beating patterns can lead to really novel insight concerning the cooperative motion of a large ensemble of molecular motors.

2.5.2. Novel biological insight

I measured waveforms of beating bull spermatozoa with very high precision and showed that they exhibit sinusoidal traveling waves, which can be described reasonably well by the first Fourier-mode. I was able for the first time to make a statement about the frequency stability of the beat by finding a lower estimation on the Quality factor of $Q=10$. What this might tell us about the axoneme needs to be discussed.

Furthermore, I made much more rigorous statements about the importance and the type of the boundary conditions than it has been done before. Besides the visco-elastic element at the base I was also able to show, for the first time, that there is no curvature at the tip of the tail. Hence no torque is acting at the tip. Furthermore all boundary conditions were in quantitative agreement with the theoretical predictions.

I tested the theoretical framework of the axonemal beat by Camalet where the action of the motors was incorporated in a generic way. I found that this theory is not sufficient to account for the experimental data.

Therefore I extended the theoretical work by Camalet in two respects: First, I included the possibility that the stiffness of the axoneme can vary along its length, which is necessary to describe the waveform of bull and presumably other mammalian spermatozoa. Secondly, I suggested considering a passive visco-elastic element at the base, as recently found experimentally.

I found that the varying flexural rigidity is not sufficient to account for the discrepancy between the original work by Camalet and my experimental data, while the properties of such a basal visco-elastic element can. The values that I obtained from the fit agree with what I know from the molecular and structural details of the axoneme, furthermore from experimental results obtained by other groups. Hence my work does not only represent a confirmation of the theory, but can be seen at the same time as an independent measurement of these parameters.

While discussing these parameters I realized that the viscous component of this basal element is very high compared to what one would expect. This raises the question of

whether I interpret this term in the correct way. Moreover it is even possible that a very different term is also sufficient and actually more important to account for the differences between the original Camalet work and the data. The theoretical analysis by Camalet was carried out for small amplitude approximation. Whether this approximation is valid for the experimental data is questionable but also hard to judge. Hence it is possible that some nonlinear correction term is already sufficient and consequently the importance of the introduced basal visco-elastic element are overestimated.

If we think, on the other hand, about what this high viscosity could mean the connection to a basal switching mechanism (“geometric-clutch”) (Lindemann and Kanous 1995) becomes apparent, where the active motors that are stalled on one side, get ripped off the filaments. This is a typical scenario leading to protein friction. Hence models like the “geometric-clutch” seem to be in agreement with my data and the suggested theoretical framework. This again highlights the power of such a generic approach since my conclusions so far are independent of any molecular model concerning the coordination of the motors.

As one of the key results I saw how the waveform depends on these basal attachment properties and more generally on all boundary conditions. This suggests that the basal region has been evolutionary optimized in different species and axonemes to generate a certain wave pattern. For instance, in spermatozoa the attachment might be such to generate the most effective forward propulsion while in cilia it might generate a certain beat pattern leading to a desired fluid flow. I furthermore speculate that a cell might be able to alter these attachment properties on shorter timescales to regulate the beating behavior of the axoneme.

Finally I want to comment on earlier and similar work. The idea of analyzing waveforms of beating spermatozoa is far from new and a fast literature on just this approach has been accumulated. Hence it is a valid and important question to ask, what my new and original contributions are and how they compare to this earlier work.

The corresponding literature is huge and hard to oversee. My work certainly differs in how I carried out this waveform analysis. First, I was the first to analyze the average of a large number of beating cycles compared to typically one or two in earlier work. Second, I did not compare the results of a specific model visually to the

experimentally observed waveforms. Instead I fitted a generic theory directly to the experimental data, which is unbiased and also delivers back the fitting parameters. Third, I made some solid statements about the boundary conditions, which also had not been done before.

In earlier work it is generally assumed that the microtubules are incompressible. As I discussed, it is very reasonable instead that they can get compressed. This leads to different sliding displacements along the tail that are not proportional to the tangent angle. There is one study where this sliding displacement actually was directly measured with gold-beads that were attached to the sliding filaments (Brokaw 1989). The conclusion of this work is that the sliding displacement is proportional to the tangent angle, which is in contrast to my suggestions. This work was carried out on sea urchin spermatozoa where the microtubules are connected differently at the base than in the case bull spermatozoa used in my study. This could explain the difference. On the other hand I might be wrong with my suggestion on that basal element. Furthermore it would be interesting to carefully check the analysis in (Brokaw 1989) whether this data is consistent with some basal filament sliding and how much this sliding could be. Hence there are still many open questions and it becomes obvious that additional and alternative approaches to such a waveform analysis are needed.

I summarize that the generic theory by Camalet in its present extended form is a valid description for the beating pattern of a spermatozoon that is clamped at its head and exhibits planar beat. It would be valuable to include the nonlinearities as well to hopefully reach full quantitative agreement between experiment and theory. These nonlinearities are also needed if one wants to predict the amplitude of the wave and to discuss the stability of the oscillation with respect to slight perturbations. It is important to pose the open questions more sharply, as well as to design and carry out new experiments.

2.5.3. Suggested future work

As a next important step I will test, whether the other data sets, that is pivoting head, free swimming spermatozoon and the different viscosities, lead to an equally good agreement with the theory and to similar, and hence consistent, parameter values.

To avoid the complication of dealing with too many unknown parameters at the same time, I suggest the following experimental scheme of micromanipulation experiments. First, spermatozoa from a different species should be used that have a homogenous tail, such as sea urchin or *Ciona*. This reduces the ambiguities according to the stiffness variations. Second, the spermatozoon should be demembrated and the motors deactivated in such a way that they are detached from the opposite microtubule and hence the axoneme is not in a rigor state, which prevents microtubule sliding. Third, such a spermatozoon should be fixed at its head with a suction needle. With a piezo, different stimuli can be applied by varying the frequency and amplitude (Gibbons, Shingyoji et al. 1987). The obtained waveforms then contain the pure information of the internal visco-elastic parameters, the visco-elastic element at the base, the axonemal stiffness and hydrodynamic friction with the surrounding media. In that way, all actions of the motors are avoided. Hence the obtained waveforms have less free parameters than used in the present study. Furthermore, stimuli of different amplitudes and frequencies allow us to test within what ranges a linearized description as presented by Camalet is valid, and at what point nonlinearities have to be taken into account.

Having obtained this, the experiment could be completed by subjecting such a demembrated spermatozoon under different stimuli to different biochemical conditions, e.g. ATP-concentrations, hence testing the motors themselves. Such experiments have been done (Shingyoji, Yoshimura et al. 1995), but unfortunately in that study no systematical comparison to any theory was undertaken.

I want to mention that I have set up this experiment and that I have already applied sinusoidal stimuli to mobile and immobile spermatozoa. Yet, I was not able to carry out this experiment systematically, mainly due to seasonality concerning the fresh sea urchin sperm supply, and also since I finally ran out of time towards the end of this thesis. Hopefully, I can finish this project in the near future.

The other project at hand, as already mentioned, is the study of long time series of non-periodic sperm beating to test the cooperativity of many motors in a novel regime using the developed tracking software.

3. Self-organized vortex array of sperm cells

3.1. Abstract

I report a self-organized spatio-temporal pattern formed by hydrodynamically entrained spermatozoa. At planar surfaces these spermatozoa form dynamic vortices resembling quantized rotating waves. The vortices in turn form an array with local hexagonal order. Introducing a novel order parameter to quantify the cooperativity of many particles, I show that the array is formed above a critical sperm density. This demonstrates that large-scale coordination of cilia and flagella, such as in ciliary metachronal waves and during sperm cooperation, can, in principle, be regulated via critical phenomena. Moreover, I estimate the hydrodynamic interaction forces between cilia and flagella to be ~ 0.1 pN.

3.2. Introduction: The experimental observation

The oscillatory bending waves of the sperm tail that propel the spermatozoon through the fluid lead to a helical path. If a spermatozoon approaches a planar surface it may get trapped at the surface where it follows a circular swimming path (Woolley 2003) (movie M3). These paths often have a strongly preferred handedness (Woolley 2003).

I found that the spermatozoa of sea urchins (*Strongylocentrotus droebachiensis* and *S. purpuratus*) get trapped at the liquid-glass interface and self-organize into an array of vortices (Fig.15A, B and movies M1, M2) at a high surface density. At the density used in Fig. 15 each vortex contained 10 ± 2 spermatozoa (unless otherwise stated, values refer to mean \pm standard deviation) circling clockwise (observed from inside the water phase) around a common centre (Fig.1C-F). The circular paths had radius $R=13.2 \pm 2.8$ μm , the time for one revolution was $T=0.67 \pm 0.09$ s, and the swimming speed was $v=125 \pm 21$ $\mu\text{m/s}$. The beat frequency was $f=41.7 \pm 3.7$ Hz. Occasionally the hopping of spermatozoa between vortices and the fusion of two vortices was observed. The vortices were densely packed and their centers moved randomly with an apparent diffusion constant of $D=6.2 \pm$

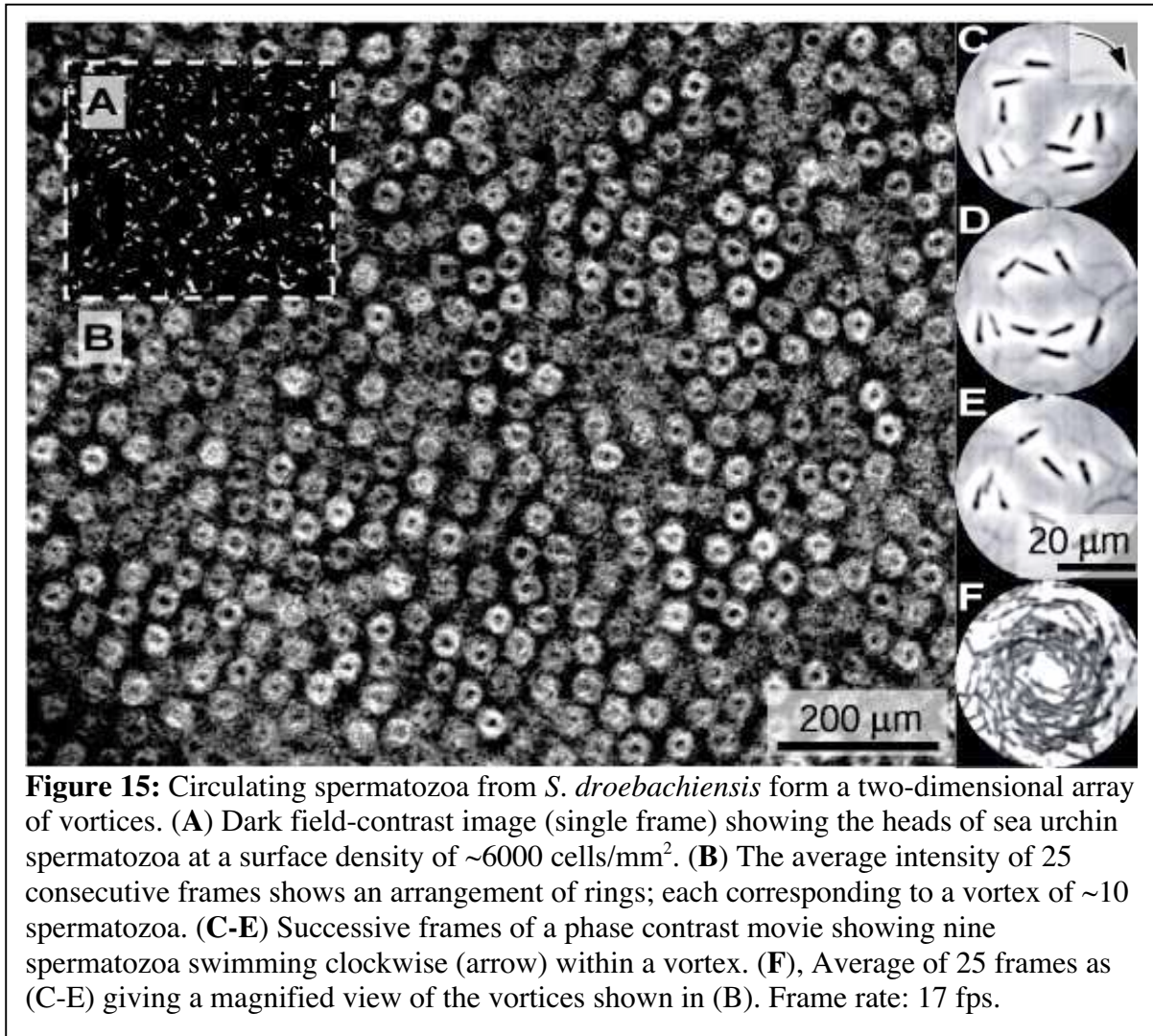


Figure 15: Circulating spermatozoa from *S. droebachiensis* form a two-dimensional array of vortices. (A) Dark field-contrast image (single frame) showing the heads of sea urchin spermatozoa at a surface density of ~ 6000 cells/mm². (B) The average intensity of 25 consecutive frames shows an arrangement of rings; each corresponding to a vortex of ~ 10 spermatozoa. (C-E) Successive frames of a phase contrast movie showing nine spermatozoa swimming clockwise (arrow) within a vortex. (F), Average of 25 frames as (C-E) giving a magnified view of the vortices shown in (B). Frame rate: 17 fps.

$0.9 \mu\text{m}^2/\text{s}$. Thus the pattern formed by the spermatozoa reflected two levels of order, namely a clustering into vortices and a packing of the vortices into an array

Generally, the emergence of spatiotemporal patterns is of great interest in many scientific disciplines (Cross and Hohenberg 1993). Examples include physical self-assembly (Grzybowski and Whitesides 2002), oscillating chemical reactions (Zaikin and Zhabotinsky 1970), self-organization of cellular components (Nedelec, Surrey et al. 1997) and micro-organisms (Ben-Jacob, Cohen et al. 2000; Dombrowski, Cisneros et al. 2004), and the social activity of insects (Hoelldobler and Wilson 1990). Such patterns can arise either due to self-assembly or self-organization (Misteli 2001). While the first one generates equilibrium structures, the latter happens far from thermal equilibrium and is associated with a permanent dissipation of energy (Turing 1952; Prigogin.I and Nicolis

1967), which is the case for the ATP-hydrolyzing spermatozoa. Even if self-organized patterns appear static on a macroscopic level, they are dynamic on the microscopic level and changes in one of the microscopic parameters can lead to very sudden changes in the overall pattern. This duality of stability and flexibility makes self-organized processes favorable for many biological regulatory and dynamic processes (Nedelec, Surrey et al. 1997; Misteli 2001). In this spirit I analyzed this unexpected vortex array (Fig.15) to reveal its underlying physical cause and to determine its possible relevance for related biological processes.

3.3. Methods

Sperm and imaging.

Dry sperm from the sea urchin *Strongylocentrotus droebachiensis* and *S. purpuratus* (green and purple sea urchin) (Westwind Sealab Supplies, Canada) where collected following 0.5M KCl injections (Brokaw 1986), stored on ice, and used within 3 days. Presented data are from green sea urchins.

The spermatozoa were observed in an open plastic or glass dish (diameter: 2.5 cm, volume: 1ml – hence the fluid layer was so thick that spermatozoa trapped at one surface did not experience the opposite surface) pre-incubated for 5 min with 1% F-127 (Sigma, #P-2443) in PBS to prevent sticking. The dry sperm were gently diluted six-fold in artificial seawater (ASW, without Ca^{2+}). This suspension was either further diluted homogeneously, or a highly concentrated drop was placed in an ASW filled dish leading to changes in sperm concentration over time. The sample was imaged on the plastic- or glass-liquid interface. Movies were taken approximately 5 minutes after adding the sperm, except for studies on sperm surface density dependence where the data were within 15 minutes after adding. Motility was good for 20-30 minutes. I noticed that the circling radius of the spermatozoa decreased over time, independent of the sperm surface density. Presumably this is due to the absence of Ca^{2+} (ref. (Brokaw 1986)). It does not effect any of my conclusions (see Appendix A2).

Experiments were carried out at room temperature on an inverted microscope (Zeiss Axiovert 200M) at magnifications between 5 and 40x using dark field or phase

contrast. Movies were taken with a Fastcam (Photron) or Coolsnap HQ (Photometrics) camera.

Data analysis.

The analysis was carried out with Metamorph (Universal imaging) and Matlab (The Math Works, Inc.). Objects were traced by hand and at least six objects were analyzed to estimate averages and standard deviations.

Analysis single vortex.

I tracked the orientation $\alpha(t)$ relative to the laboratory frame of seven sperm heads within one vortex over 1100 frames (Frame rate: 250 fps). The angular position of the head in its trajectory around the vortex, $\Phi(t)$, and the phase of the oscillation of the head during the beat of the spermatozoon, $\varphi(t)$ were filtered from the relation

$\alpha(t) = \Phi(t) + \pi / 2 + \alpha_0 \cos(\varphi(t))$. (On average this relates to $\Phi(t) = 2\pi / T \cdot t + \Phi_0$ and $\varphi(t) = 2\pi f \cdot t + \varphi_0$, where T is the circling time and f is the beat frequency of a spermatozoon.) Then for each $\Delta\Phi$ -channel in Fig. 3C I computed the mean as

$\Delta\bar{\varphi}(\Delta\Phi) = \text{phase}(1/N \cdot \sum_{j=1}^N e^{i\Delta\varphi_j})$ (Fig. 17 E), where N is the total number of $\Delta\varphi$ in a given $\Delta\Phi$ channel.

Order parameter χ .

The grayscale images were thresholded to give binary images in which only the sperm heads were visible. The frame rate (17 fps) and total number of frames (10) ensured that individual spermatozoon had negligible self-overlap over the analysis time. Frame rate, number of frames, and object size influence the value of the order parameter χ . But the dependence of χ on sperm density (plateau followed by a transition towards a positive slope at 2500 cells/mm²) is always independent of parameter choice as shown with a number of controls (see SOM). Therefore these parameters do not interfere with the information content of χ . Hence χ is a robust measurement tool for such correlations.

Model, simulations, and simulated movies.

Starting from random distributions I let 1000 particles equilibrate accordingly to the following equations:

$$\bar{r}_i(t + \Delta t) = \bar{r}_i(t) + \sqrt{2D\Delta t} \cdot \bar{G}_i(t) + \bar{F}_{j \neq i} / \gamma \cdot \Delta t \quad \text{Eq. 43}$$

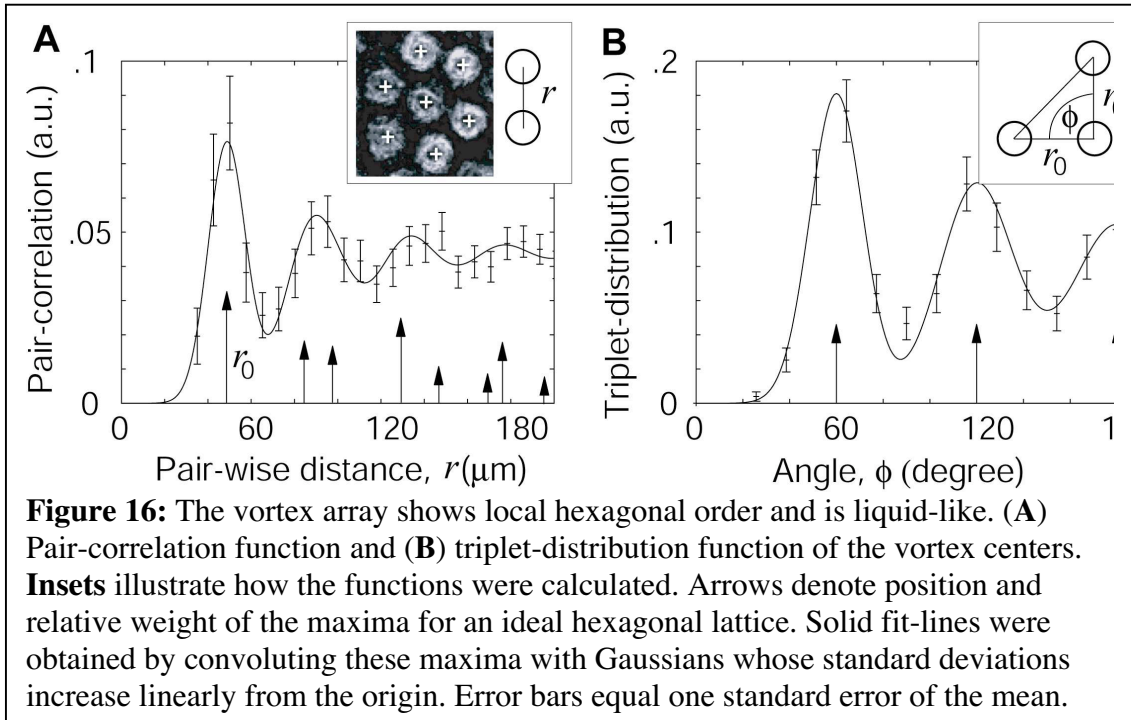
where \bar{r}_i is the position of the i^{th} particle, t is the time, Δt is the time step size, D is the diffusion constant of a free particle, \bar{G}_i is a Gaussian distributed random variable with mean zero and variance one, $\bar{F}_{j \neq i}$ is the interaction force due to all other particles j , and γ is the viscous drag coefficient. A quadratic box with periodic boundary conditions was used. The box-size was chosen to give the desired particle densities for the 1000 particles. The pair-wise interaction among particles is determined by the potential V in Fig. 18D. The experimental measured values for D and R were used. The only free parameter, V_0 / γ , was chosen to match the experimentally obtained curve in Fig. 18C. I averaged the results of six simulations.

To generate simulated movies I assigned to the position of each particle in the equilibrium configuration a spermatozoon head with circling radius, angular velocity, square head, and a random starting phase in the swimming circle. Radius and velocity were randomly chosen from the experimentally measured distributions. Head size was chosen to equal the number of pixels observed for a sperm head in an experimentally obtained movie.

3.4. Results

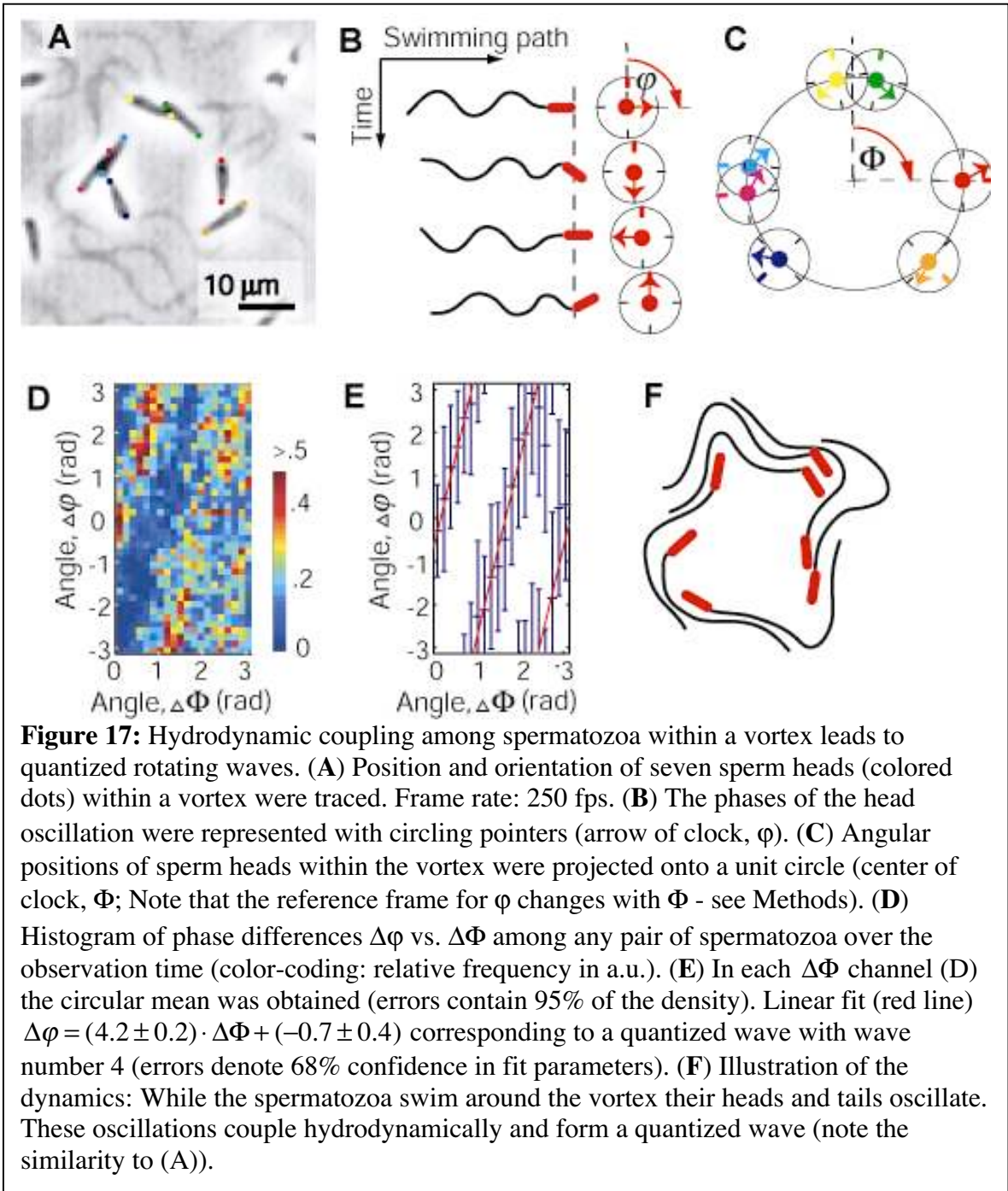
3.4.1 Vortex liquid – spatial correlations

I assessed the packing-order of the vortex array by measuring various correlation functions of the vortex centers. The pair-correlation function and the triplet-distribution function (Zahn, Maret et al. 2003) revealed a local hexagonal order with an average vortex spacing of $49 \pm 9 \mu\text{m}$ (Fig.16). Furthermore, the bond-angular correlation function (Zahn, Lenke et al. 1999) (data not shown) showed an exponential decay revealing the absence of long-ranging order. This characterizes the array as being liquid-like in contrast of being hexatic or crystalline (Zahn, Lenke et al. 1999).



3.4.2. Quantized rotating waves

I asked how the spermatozoa within a vortex (Fig.17A and movie M4) influence each other. Interactions could lead to changes in the circling radius, the swimming velocity or the beat frequency. However, within experimental errors, I found no differences in these parameters whether spermatozoa were in a vortex or isolated (data not shown). On the other hand, I found a particular form of synchronization of the beating patterns of spermatozoa within a vortex, indicating that interactions do indeed take place. I described each spermatozoon by two variables: the phase of the oscillation of the head during the beat of the spermatozoon, $\varphi(t)$ (this oscillation is driven by and has the same frequency as the oscillation of the tail, Fig.17B); and the angular position of the head in its trajectory around the vortex, $\Phi(t)$ (Fig.17C). No correlation in $\Phi(t)$ between any two spermatozoa in the same vortex was found (data not shown). The same was true for $\varphi(t)$ (data not shown). In other words, spermatozoa within a vortex swim at different speeds and beat at different frequencies. However, there is a strong correlation between the differences $\Delta\varphi(t)$ and $\Delta\Phi(t)$ between pairs of spermatozoa in the same vortex (Fig.17D-



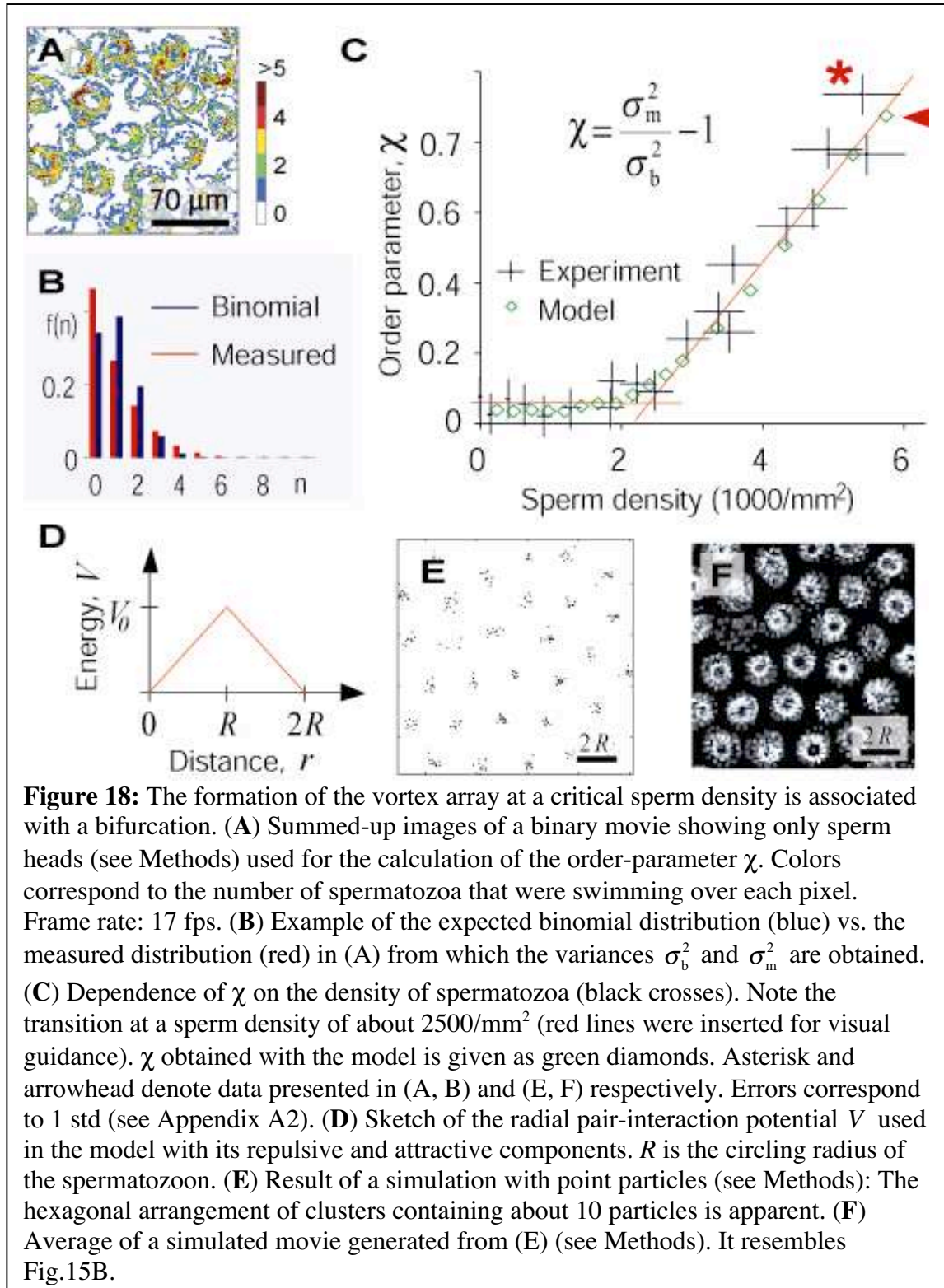
E). Such a correlation implies that, for example, if one spermatozoon swims twice as fast as another then it also beats at twice the frequency. This means that locally the tails are beating in synchrony and that a trailing sperm follows in the wake of the leading one. Consequently, because the spermatozoa swim in closed circular paths, there must be an integral number of wavelengths along the circumference of the vortex. The slope, $\Delta\phi/\Delta\Phi$,

was 4.2 ± 0.2 (Fig.17E). This is consistent with a wave number of 4 which is determined by the geometry of the vortex: dividing the circumference of the path ($2\pi R$, where $R=11.6 \pm 3.0 \mu\text{m}$ was the swimming radius within this particular vortex) by the beat wavelength on the sperm tail ($\lambda=17.6 \pm 1.3 \mu\text{m}$ along the curved centerline of the flagellar waveform, not along the tail) gives 4.1 ± 1.4 . Thus I conclude that hydrodynamic coupling of the sperm tails within a vortex leads to a quantized rotating wave with wave number 4 (Fig.17F).

This hydrodynamic interaction between sperm tails within a vortex is a generalization of the synchronization of the beats of two spermatozoa swimming close to one another (Gray 1928; Taylor 1951; Gray and Hancock 1955). My rotating waves are related to the metachronal waves observed on the surfaces of ciliates and ciliated epithelia and which are respectively important for swimming motility and the movement of mucus (Okamoto and Nakaoka 1994; Gueron and Levit-Gurevich 1998). In contrast to the three-dimensional metachronal wave, however, the waves described here are two-dimensional and hence much easier to analyze. Therefore such a vortex may serve as an experimentally accessible model system for metachronal waves.

3.4.3. Pattern formation via a bifurcation

I now address the question of how the spermatozoa self-organize into an array of vortices. Because I did not observe vortex arrays at low sperm surface densities, I suspected that density might play a role in the self-organization process. To quantify the order at the different densities I defined a novel order-parameter χ as follows. The binary images of each movie showing only sperm heads were summed such that each pixel value in the resulting image was proportional to the number of different spermatozoa that swam over that pixel (see Methods, Fig.18A). If the swimming paths of different spermatozoa are uncorrelated, then these pixel values are binomially distributed. However, if spermatozoa accumulate in a vortex they trail each other and the distribution differs from a binomial one because low and high pixel values (corresponding to centers of the vortices and swimming trails respectively) will be over-represented (Fig. 18B). In this case, the variance of the measured distribution (σ_m^2) will be larger than that of the



binomial distribution (σ_b^2). This motivated my definition of the order parameter:

$\chi = \sigma_m^2 / \sigma_b^2 - 1$. χ has the expected properties of an order parameter: it is zero for a

random configuration, and is greater than zero if spermatozoa share similar swimming paths. The value of χ depends on the average number of spermatozoa per vortex and how well the centers of their circular swimming paths co-localize. χ is a robust measure for the correlation among the objects and is related to the pair-correlation function (see Appendix A2). Furthermore χ has the advantage that no labor-intensive object tracking is required. χ may be a useful tool for quantifying order in other spatiotemporal patterns involving tracks of multiple particles or signals such as intracellular organelle transport (Nielsen, Severin et al. 1999) or ant trails (Hoelldobler and Wilson 1990).

I measured the order parameter χ for various sperm surface densities and found two regimes (Fig.18C). Below 2500 cells/mm², χ was independent of the surface density and was almost zero, indicating that the swimming paths of the spermatozoa were random. Above about 2500 cells/mm², χ increased linearly with density indicating that the correlation among the swimming paths increased. At 6000 cells/mm² the ordered state corresponding to Fig. 15B was reached. The discontinuity in the slope of the curve suggests a bifurcation separating a disordered and an ordered regime. The critical sperm density corresponds to about 4 sperm/vortex.

3.4.4. Equilibrium model

In order to gain insight into the physical mechanisms underlying the pattern formation, I propose a simplified model. The model incorporates a short-range attraction between pairs of spermatozoa, arising from the hydrodynamic forces that lead to the observed synchronization (see ref. (Fauci and McDonald 1995)), and a longer-range repulsion that could be of steric or even hydrodynamic origin (Lenz, Joanny et al. 2003). I represent each spermatozoon by a point particle located at the centre of its circular path. These particles move randomly with an apparent diffusion coefficient of $D=9.0 \pm 2.0$ $\mu\text{m}^2/\text{s}$ measured for isolated sperm. This apparent diffusion coefficient is much larger than the thermal diffusion coefficient $D=0.06$ $\mu\text{m}^2/\text{s}$ of a disk similar in size to a vortex ($D = kT / \gamma$, $\gamma = (32 / 3) \cdot \eta R = 7 \cdot 10^{-8}$ Ns/m, radius $R=13$ μm , friction in water $\eta=1\text{mPas}$) (Berg 1993). The enhancement of the randomly directed motion is due to the

active propulsion of the spermatozoa (Wu and Libchaber 2000; Darnton, Turner et al. 2004) and indicates that the system is not in thermodynamic equilibrium. Furthermore, circular flow is not describable by a potential (Landau and Lifshitz). Nevertheless, as I show below, several important features of the pattern formation are captured by an equilibrium model with the pair-wise interaction potential shown in Fig. 18D.

Stochastic simulations of this model (see Appendix A2) reveal two regimes: a random distribution of particles at low densities and a hexagonal array of clusters at high densities (Fig. 18E). Assigning to each particle a spermatozoon circling around that position, I generated simulated movies (see Methods). A time-average of such a movie (Fig. 18F) mimics the experimentally observed vortex array (Fig. 15B). Moreover the order parameter χ computed for different simulated sperm densities also shows a discontinuity in the slope as was observed experimentally (Fig. 18C). These numerical results are supported by a one-dimensional mean-field analysis (see Appendix A2) that indicates the existence of a critical density associated with a supercritical pitchfork bifurcation (Strogatz 2000). This critical density is proportional to the interaction strength and inversely proportional to the diffusion coefficient, where the latter is associated with the noise in the system.

3.5. Discussion and conclusions

Fitting the model to the data allows me to estimate the strength of the interaction force, F_{int} , between two spermatozoa. The only free parameter in my model (the ratio of the maximum interaction potential to the drag coefficient, $V_0 / \gamma = 5 \cdot 10^{-12} \text{ m/s}$, see Methods) was chosen to match the critical density. Assuming a viscous drag coefficient of a disk as estimated earlier, I find $F_{\text{int}} = |\text{grad}(V)| = (V_0 / \gamma) \cdot \gamma / R = 0.03 \text{ pN}$. This force is about 1% of the forward propulsion force of a spermatozoon $F_{\text{for}} = 5 \text{ pN}$ (Howard 2001) and appears to be of the correct order of magnitude for hydrodynamic forces between particles of this size moving at these velocities (e.g. two rotating spheres (Landau and Lifshitz 1987), page 65). Though this force is small, it is evidently large enough to lead to synchronization and attraction.

I conclude with a discussion of potential implications of my findings. It is unlikely that the vortex array that I have described is directly exploited by any organism for reproduction because it is formed at a surface whereas spermatozoa normally swim in three dimensions. However, I speculate that related patterns might exist in three dimensions and be of biological importance. For instance, the adhesion of spermatozoa can lead to the formation of sperm trains (Moore, Dvorakova et al. 2002) in a process called sperm cooperation that is important for reproduction. My work has shown that hydrodynamic interactions are also capable of coordinating large numbers of spermatozoa and hence could provide a second mechanism for sperm cooperation. On a more conceptual level, my finding of a threshold density for the vortex array suggests that cooperation of large numbers of cilia and flagella can be achieved and regulated via a critical process. For instance the metachronal waves seen in ciliates and ciliated epithelia (Sleigh 1974; Okamoto and Nakaoka 1994) also comprise large numbers of axonemes that can be switched on and off, and changed in form or direction through modulatory processes that are still poorly understood. I propose that physiologically controlled changes of the activity of the individual cilia can change the value of the critical cilia density compared to the actual cilia density and therefore can provide a switching mechanism for the metachronal wave. In summary, I have described a dynamic pattern of cells that forms by hydrodynamic interaction without the need of chemical signaling and may illustrate important concepts for how activity of collective biological processes can be switched.

Outlook

What have we gained? In this thesis two different, though related projects, were presented. The results of both were already discussed and summarized in the corresponding chapters. Hence I do not find it worthwhile to be repetitive at this point. Instead I want to take a step back and comment on some general lessons I can draw from the two projects.

The waveform analysis of beating spermatozoa in the first part brought a deeper understanding for the theory and led to new insights. I clearly did not solve the problem of axonemal beating as such, hence the achievements might seem incremental from a broader perspective. This is no surprise since it has been a longstanding problem where a lot of work has been carried out already. Making another substantial step in a mature field requires a solid foundation on this earlier work, which usually is not even sufficient. Looking back I think that a longstanding question should only be approached with a really novel idea or technique. This was also the initial intention by building a force transducer for spermatozoa, which unfortunately did not work out. However, even when the initial plan fails there is still a possibility to make a solid contribution to the field.

The analysis of the vortex array formed by spermatozoa was based on a phenomenon that one could call a lucky finding. Looking back and thinking about the term “luck”, I think there is a lesson on how to discover something. It is hard to believe that no one has seen this pattern before since sea urchin spermatozoa have been used in many labs for decades; furthermore I observed this pattern for two different species. Hence discovering is not simply being lucky and seeing an effect. It also requires actively noticing it and making the decision that it might be an interesting subject being worth studying. And there is also the opposite way of how to discover something. One can rather quickly form a hypothesis and then try to prove it, which in turn might need lots of persistence. That the formation of this pattern should be associated with some sort of transition is rather obvious. But it took me a lot of trial and error until the right idea came along on how to measure the order in the system in an efficient way, as well as to make the necessary controls to prove that this idea was actually correct.

Finally I want to admit that one of my strongest motivations to switch from physics to biology was the impression that the phenomena under study were much more lively. I never regretted my decision since this turned out to be true, actually in a double-sense: These phenomena are what we call “live” but they are also so fascinating, enjoyable and even funny to fully compensate for the frustrations we experience when trying to unravel them.

Appendices

A1 Coordination of axonemal beating

The goal of this section is to describe the algorithm that was used to detect the outline of a spermatozoon within a single image. This outline was converted into a one-dimensional description, where the outline is given by the tangent angle along the curve. This waveform was measured in many successive frames of a movie corresponding to typically 10 frames per beat cycles and 100 beating cycles in total. This time-series, which shows a very regular beat, was then subjected to a Fourier analysis. This leads to an averaged waveform of higher precision than what could be obtained from a single beat-cycle. Finally I estimate the precision of this averaged waveform.

Movie acquisition

Figure 10A shows a typical image of a movie taken at 250 fps. The movies were taken at 10x Phase-contrast and under standardized light intensity leading to similar contrasts and resolution in the final movies. All movies showed only a single spermatozoon. If dirt particles of significant contrast were observed within the movie the movie was rejected, since this dirt could lead to detection failure, e.g. detecting the dirt-particle instead of the tail.

Wave form detection

A detection algorithm usually does not work by measuring the feature of interest in an image straight away with the desired precision. If a person is asked to measure the length of an object in an image, one might think that this person just measures this length within one step. But instead the person first has to spot the object, decide on its orientation, and decide where the beginning and end is. Then it puts the ruler along, and before reading off any number checks again whether the ruler is properly aligned. Hence it is actually quite a complex task that is broken up in a few sub-steps that one is usually not aware off. Accordingly I also designed the detection algorithm in such a way, that the desired objects are detected coarsely first, and then re-measured with a few iterations and

increasing precision. I also want to mention, that the development of such an algorithm also involves a lot of trial and error to obtain a certain robustness and precision in the algorithm. All programming was carried out in Matlab (Mathworks Inc.) The algorithm works as follows:

First, the whole image is searched for that square-pixel-matrix of a certain size (6x6 pixels) that has the lowest total intensity. This spot corresponds roughly to the head. Around this square an area of a bigger size is thresholded and an ellipse is fitted to it. Hence the outline and the center of the head are roughly known, but so far it is not clear, into what direction the tail starts. Therefore, around the center of the head a circle is drawn, with the radius being clearly larger than the size of the head. Along the circumference of this circle for the highest intensity is searched, which coincides with some basal part of the tail. Hence this point together with the center of the head give roughly the symmetry line of the head including the direction of tail.

This leads to the task to detect the head more precisely: Perpendicular to the head orientation slices through the head are analyzed. Each of these slices corresponds to a cross-section of the head, which is symmetric in the case of a bull spermatozoon. Therefore, each of these slices gives a point of the centerline of the head. 9 of these centerline points are obtained and a line is fitted through them leading to a very precise orientation of the head. Along this orientation the tip of the head is measured by interpolating for the point where the intensity is half way between the intensity of the head and the intensity of the image in the surrounding of the head.

Knowing the tip and the orientation of the head precisely, the base of the tail is also known, since all bull sperm heads look very similar in size and shape. Actually, the point where the tail starts in absolute terms is not detectable in such a 10x Phase-contrast image, since the tail grows out of the head and the circumference of the tail seems to shrink smoothly to the thickness of the tail. Hence I use an arbitrary but fixed distance from the tip of the head, which is in agreement with the distance that was measured from a higher-resolution image (40x) of a bull spermatozoon. The orientation of the tail in the very basal region coincides with the orientation of the head as far as I can tell, even from higher resolution images.

Now I detect the outline of the tail. Starting from this first basal tail-point, for the second tail-point is searched in the following way: Along the head orientation at a given distance (corresponding to the length of 2 pixels or $1.4 \mu\text{m}$) the next tail-point is suspected. Through this point a line is drawn perpendicular to the presumed tail outline. Along this line a gauss is fitted, with its maximum corresponding to the second tail point. Such fitting finally leads to a sub-pixel resolution in the detection of the tail-center. The vector connecting the first and the second tail-point points towards the third tail-point, which is then found as the second one before. This procedure is repeated 44 times, which corresponds to the total length of the tail.

Unfortunately, no robust detection algorithm could be developed that reliably detects the very tip of the tail. This is due to the fact that the tail gets thinner towards the end leading to a decrease in contrast, furthermore the tail end is the piece of the spermatozoon that moves fastest through the fluid hence it is also smeared out during the exposure time of the camera. Since it was not possible to find the end of the tail by eye reliably, I decided that it was not likely to find a reliable way to detect it automatically. The tails of all bull spermatozoa are very similar in length $L = (58.3 \pm 0.6) \mu\text{m}$ (mean and standard deviation) hence I have an uncertainty in length of 1%. I detected the tail along 44 points where 3 points were still inside the head. Hence I measured a tail-length of $41 \cdot 1.4 \mu\text{m} = 57.4 \mu\text{m}$ meaning that on average I miss about $1 \mu\text{m}$. This uncertainty has to be taken into account if in later analysis the waveform $\psi(s)$ is integrated or a derivative at the tip is computed.

So far, the tail-points are not equally spaced, especially if the tail undergoes high curvature. Furthermore their center-positions are noisy and off to both sides of the tail-symmetry line. This noise is reduced by filtering the x and y coordinates of the tail with a Savitzky-Golay-Filter (Press, Vetterling et al. 2002) with a span of 9 and a degree of 5 (A discussion on the optimal choice of the span and degree can be found in (Press, Vetterling et al. 2002). Their values depend on the noise and the typical size of a curved region.). This filtered outline is now interpolated with splines (Press, Vetterling et al. 2002). Starting from the base of the tail, equally spaced points along this outline are determined by integrating the distance between any two points along the arc-length. Hence the tail-

points are centered now with very high precision on the tail, and are also equally spaced. (I will estimate the associated errors in the next subsection.)

The data points obtained in this way are then stored as absolute positions within the image, furthermore tangential orientations of the head and tail relative to the x-image axis are calculated. These tangential orientations are obtained by fitting local Chebyshev polynomials of 9th degree with span 5 through the x - y -coordinates, from where the derivatives and hence the tangents could be calculated analytically via the Chebyshev coefficients. (For more detail see (Press, Vetterling et al. 2002), also a discussion on the optimal parameter choice can be found there.)

Hence finally, the tip-position of the head, the orientation of the head, and the orientations of the tangents on each tail-point lead to a full description of the outline. Here the arc-length of the tail is denoted by s and the tangent is $\psi(s)$. Re-plotting the outline of the waveform starting from the tip of the head and using only the tangents on these tail-points $\psi(s)$ leads to very good visual agreement with the initial waveform (not shown). Note that this outline in angular representation is one-dimensional, which makes the following analysis very convenient compared to a description of the waveform in (x,y) -coordinates.

The typical time it takes to detect the waveform within one image is in the order of 3 sec on a standard desktop PC. Hence, even very long movies, such as 30.000 frames, can be processed within 10 hours, hence no additional expensive computer power is needed concerning the overall data needed for this and possible follow up projects.

Since the spermatozoon had to be observed in comparatively long movies (up to 30.000 frames, for the presented analysis only 1024 were used) and one can never guaranty that the detection does not fail within some of the images, e.g. due to some dirt particle flowing through, an error-check was built in to judge whether the detection was successful. The criteria were that the maximum curvature of the tail did not exceed a certain value or that the tail did not cross itself. In such cases a place holder was kept in the whole data set taking care than in subsequent analysis, such as the Fourier analysis, no data points were used from these images. Usually, in all of the 1024 frames the spermatozoon was detected correctly, the failure rate in general is certainly much less than

1 in 100 frames. Therefore, if care is taken while acquiring a movie, the final detected data is of sufficient quality and completeness to do a time series analysis.

So far I did not discuss the detection uncertainty quantitatively. This will be done in the coming subsection.

Errors in waveform detection

The error on the waveform, which is given by $\psi(s)$, is due to two main influences: On one hand the tangent-angle $\psi(s)$ has some uncertainty itself ($d\psi_1$), furthermore the position of the tail-point s at which $\psi(s)$ is measured, can only be detected between different frames with some uncertainty ($d\psi_2$). Both influenced are quantified as follows: (All values are given as mean and 1 standard error of the mean (SEM).)

The first source of error stems from the fact that the points along the tail do not exactly lay on the center of the tail. For convenience I assume in the following that the tail is parallel to the x-axis end estimate the error for slight deviations. (Generally, the tail can have any orientation of course, but the error in the tangent angle has to be independent of this orientation, hence I can estimate the error for this particular case.) Since a Gaussian was fitted to the tail-cross-section and the positions of the tail-points were filtered (see previous section) the precision of the position in y has sub-pixel resolution and is estimated to be $\Delta y = 0.1 \text{ pixel}$. Now the tangent on the tail at the i^{th} tail-point is given by $\psi(s_i) = \arctan\left[\frac{(y_{i+1} - y_i)}{(x_{i+1} - x_i)}\right]$. For a tail parallel to the x-axis $\psi(s_i) = 0$ and the uncertainty in $\psi(s_i)$ is found by the lowest order Taylor expansion, where $(y_{i+1} - y_i) = dy$ is small and $(x_{i+1} - x_i) = \Delta L$: $d\psi(s_i) = dy / \Delta L$. Hence I find $d\psi_1 = dy / \Delta L = 0.1 \text{ pixel} / 2 \text{ pixel} = 0.05 \text{ rad} = 3^\circ$.

Second, the position s of each tail-point along the arc-length differs between different frames. This is due to the uncertainty of detecting the tip of the head, which is estimated to be $\Delta s_{\text{head}} = 0.5 \text{ pixel}$, furthermore due to the uncertainty in distance of any two neighbored points along the arc-length. This second influence was largely reduced by filtering the (x,y) -positions as described before and than fitting a spline (Press, Vetterling

et al. 2002) through it, along whose arc-length the successive points were found (see previous section). The uncertainty in distance between neighbored points was fixed to be not larger than 0.05 pixel . The uncertainty in the position in neighbored frames increases towards the end of the tail in a random walk like fashion, since some of the inter-point distances are too large and some are too small. Hence I find for the uncertainty Δs_L at the tip of the tail ($s=L$, where L is the length of the tail):

$\Delta s_L = \Delta l \cdot \sqrt{N} = 0.05 \text{ pixel} \cdot \sqrt{44} = 0.3 \text{ pixel}$. Adding the variances of Δs_{head} and Δs_L I find $\Delta s_{total} = 0.9 \text{ pixel}$. Together with the upper limit for the average curvature $\partial_s \psi = 5^\circ / \text{pixel}$ (the waveform at the tip is approximated by an arc with a circumference of about $50 \mu\text{m}$ where one pixel corresponds to $0.7 \mu\text{m}$) I can estimate the maximum error due to uncertainties in position s at the tip of the tail by $d\psi_2 = \partial_s \psi \cdot \Delta s_{total} = 3^\circ$. Towards the base this uncertainty is less since the maximum curvatures gets smaller and the uncertainty in tail-position s is also less. In principle at the base this contribution to the total uncertainty is zero. Hence it is reasonable to reduce this value to

$d\psi_2 = \partial_s \psi \cdot \Delta s_{total} = 2^\circ$ as an estimate being valid on average everywhere along the tail.

Taking both errors $d\psi_1$ and $d\psi_2$ together by adding up their variances I find $d\psi_{total} = 4^\circ$. A visual inspection of raw data curves such as in (see figure 10D) reveals that this is a reasonable value. This uncertainty can be significantly decreased by averaging over the waveforms obtained over many successive beat-cycles as described in the following section.

Fourier analysis

A visual inspection of a beating spermatozoon under physiological conditions reveals a very periodic pattern. (This is not necessarily the case, e.g. at unphysiologically low temperatures a rather erratic movement of the sperm tail can be observed.) This periodic pattern makes the Fourier analysis an ideal tool to average the waveform over many beating cycles. The Fourier analysis is carried out at each tail-point s separately using a Hanning window and a fast Fourier algorithm as described in the methods.

The Fourier analysis revealed clear peaks at the main frequency and its higher harmonics. It was found that at the tip 95% of the power in the Fourier spectrum was

contained within the first mode. At more basal parts of the tail this value is typically higher. Since the power is $|\psi|^2$, these 95% correspond already to 10% in ψ , which is still comparatively small but might become an important influence for spermatozoa beating under slightly different conditions. Hence for the presented data the waveform $\psi(s,t)$ for a given s changes nearly sinusoidal in time, and the higher modes only lead to smaller corrections and consequently all further analysis is only executed at the lowest Fourier-mode.

Besides restricting myself to this lowest mode, the Fourier analysis also filters out fluctuations in the beating pattern and detection noise. Since I average over $N=100$ beat cycles these fluctuations are reduced by $\sqrt{N} = 10$ and I obtain an uncertainty in the waveform of $d\psi_{total} = 4^\circ / \sqrt{100} = 0.4^\circ$.

Hence I conclude, that the Fourier averaged waveform has an uncertainty of $d\psi_{total} = 0.4^\circ$ corresponding to about 0.5% at the maximum values of the tangent angles $\tilde{\psi}(s)$. This high precision (compared to data obtained earlier by other groups such as (Rikmenspoel 1965; Brokaw 1993)) now allows the computation of various functionals in $\tilde{\psi}(s)$ with a reasonable error, since especially the derivatives $\partial_s^n \tilde{\psi}(s)$ increase in their uncertainty with increasing n , as I will discuss in the next two sub-sections.

Computing functionals of $\tilde{\psi}(s)$

To carry out the fits according to chapter 2 I need to compute certain functionals from $\tilde{\psi}(s)$, that is derivatives and integrations. Especially the numerical computation of derivatives is a delicate issue (Press, Vetterling et al. 2002). In order to do so I approximate $\tilde{\psi}(s)$ by an expansion in Chebyshev coefficients, which form a complete set of orthogonal basis functions based on polynomials (Press, Vetterling et al. 2002). They also have the advantage that from the coefficients the derivatives and integrals can be computed analytically.

This leads to the question of how many of the basis functions to take into account. Taking too few the curve is not well approximated, taking too many (in the extreme case as many as there are data-points) I also fit the noise and hence the successively computed

derivatives are meaningless. I estimated the cut-off in two ways, which are essentially based on the same idea and lead to a similar cut-off.

On one hand I computed the root-mean-squared difference between $\tilde{\psi}(s)$ and an expansion with a given cut-off. I then use that cut-off where this difference corresponds to the total measurement uncertainty since taking more coefficients into account effectively fits the noise. I checked that the coefficients in the expansion decayed reasonably fast with increasing order, that is I find a reasonable approximation with a few coefficients. (This was not the case with a sine-cosine-expansion, which is therefore not a suitable basis set for my problem.) I also checked that the root-mean-squared difference is distributed roughly equally for all points along the tail. If it would stem from a very few or even a single point this would indicate that the chosen basis functions do not converge equally well and hence are not suited for this problem.

On the other hand I did a chi-squared test (Press, Vetterling et al. 2002) for each cut-off to determine at what cut-off this approximation goes from an unsatisfactory (insignificant) fit towards being over-fitted. (Since this statistical test compares the difference between original data and fit in contrast to the measurement and fitting uncertainties this is basically the same as the other estimation discussed before. This second one might be seen on a more solid basis since it also accounts for the number of free parameters, that is the cut-off, that are used for the expansion.)

Both estimations gave similar answers and I chose the cut-off to be 12 to compute the desired functionals of $\tilde{\psi}(s)$.

Uncertainties in functionals of $\tilde{\psi}(s)$

By knowing the uncertainty in $\tilde{\psi}(s)$ I can estimate the resulting uncertainty in the derivatives in $\tilde{\psi}(s)$ and other functionals (generally called $F(\tilde{\psi}(s))$) such as the double-integration. I estimated these errors in two ways:

First I did an analytical estimation: I assumed that two neighbored points among which the derivative needs to be calculated independently vary with $d\psi_{total} = 0.4^\circ$. Given the distance between the points of $\Delta L = 1.4 \mu m$ I find

$d(\partial_s \psi) = \sqrt{2} \cdot d\psi_{total} / \Delta L = 0.4^\circ / \mu m$. The same holds for higher derivatives leading to

$d(\partial_s^2 \psi) = 0.4^\circ / \mu m^2$, $d(\partial_s^3 \psi) = 0.4^\circ / \mu m^3$ etc. (This assumes that the uncertainties in neighbored points are independent, also for in the derivatives. This assumption might be questionable.) The uncertainty of an integral is much less critical than the one for a derivative. Summing over $N=44$ points with uncertainty $d\psi_{total} = 0.4^\circ$ leads to an uncertainty of $d(\int \psi) = \sqrt{N} \cdot \Delta L \cdot d\psi_{total} = 4^\circ \mu m$ and $d(\int \int \psi) = \sqrt{N} \cdot \Delta L \cdot d(\int \psi) = 40^\circ \mu m^2$.

Alternatively I can estimate these errors by simulations. I randomly generate a large set of waveforms $\tilde{\psi}_j(s)$ that is consistent with the error-statistics on $\tilde{\psi}(s)$. For each of the $\tilde{\psi}_j(s)$ the desired functional $F(\tilde{\psi}_j)$ is computed by fitting Chebyshev polynomials of the 1st kind to $\tilde{\psi}_j(s)$ and explicitly taking all coefficients into account to exactly fit the noise. From these Chebyshev coefficients the functional $F(\tilde{\psi}_j(s))$ were then computed analytically. The statistics in the sample $F(\tilde{\psi}_j(s))$ leads to the uncertainty in computing $F(\tilde{\psi}_j(s))$. This protocol has the advantage, that it is straight forward especially in the case of more complicated functionals or in cases where the uncertainty is different at different parts of the function. The simulation also reveals that the uncertainty in the derivatives at the boundaries is higher then within the bulk. This is very reasonable since no constraint exists how the polynomials should be extrapolated outside the tail.

As stated in an earlier subsection the detection of the tip of the tail is associated with an uncertainty of $\Delta L = 1 \mu m$. If one wants to measure $\tilde{\psi}(s)$ or its derivatives at the tip in order to check the boundary conditions these values have to be extrapolated via $\partial_s^n \tilde{\psi}(s) = \partial_s^{n+1} \tilde{\psi}(s) \cdot \Delta L$. Hence I find $d\tilde{\psi}(L) = 4^\circ \mu m / \cdot 1 \mu m = 2^\circ$, $d(\partial \tilde{\psi}(s)|_{s=L}) = 0.75^\circ \mu m^2 / \cdot 1 \mu m = 0.75^\circ \mu m$, $d(\partial_s^2 \tilde{\psi}(s)|_{s=L}) = 0.05^\circ \mu m^3 / \cdot 1 \mu m = 0.05^\circ \mu m^2$, where the higher derivative is estimated from its typical half maximum value. This is an additional source of error that has to be added by adding the variances of the uncertainties,

Table A1 summarizes the relative and absolute uncertainties obtained with this approach.

Functional	Unit	Typical max value	Bulk absolute error	Bulk max relative error	Uncertainty at the tip from simulation	Corrected uncertainty at tip	Relative uncertainty at the tip compared to typical maximal value
Tangent angle ψ	$^\circ$	90	0.4	0.4%	0.4	1.5	2%
$\partial_s \psi$	$^\circ / \mu\text{m}$	8	0.4	5%	1.2	1.4	17%
$\partial_s^2 \psi$	$^\circ / \mu\text{m}^2$	1.5	0.4	27%	4	4	270%
$\partial_s^3 \psi$	$^\circ / \mu\text{m}^3$	0.1	0.4	400%			
$\int_0^s ds' \psi$	$^\circ \cdot \mu\text{m}$	800	4	0.5%			
$\int_s^L \int_s^{s'} ds'' \psi$	$^\circ \cdot \mu\text{m}^2$	10000	40	0.4%			

Table A1: Overview over the uncertainties of different functionals based on $\psi(s)$ at different parts of the tail

As can be read off from the table A1, the relative uncertainties in the higher derivatives get larger, furthermore the uncertainty for the derivatives at the tip are higher than in the bulk. Both are very reasonable. From the values one can see that fitting anything up to the second derivative in bulk is possible, for higher derivatives the uncertainties get too large. The fit that has been carried as out described in the main thesis and the uncertainties in the fit parameters are mainly determined by the uncertainties in the second derivative.

The uncertainties in the boundary conditions at the base as given in table A1 are the same as in bulk. This is due to the fact that first three points belong to the back part of the head instead of to the tail itself. This constrains the fitted polynomials at the assumed position of the base, which is in contrast to the tip. But this constraint can lead to artifacts because it is not clear whether the basal part of the tail inside the head is really following the symmetry line of the head. Actually as discussed in the main text it is very reasonable that additional conformational changes take place in this region. Accordingly the values of the derivatives are not trustworthy when it comes to proofing the validity of the

boundary conditions at the base. As discussed in the main thesis I only have confidence in two boundary conditions namely concerning the $\tilde{\psi}(s)$ at the base and its first derivative at the tip.

Summary

To summarize, I developed a new tool to automatically detect the outline of a spermatozoa within the frames of a movie, where the outline is described by the tangent angle $\psi(s,t)$ along the arc-length s of the sperm tail. The initial detection in an individual image is reasonably precise, but can be significantly enhanced by succeeding Fourier analysis in the case of periodic beating leading to an approximation of the wave form by the first Fourier component $\tilde{\psi}(s)$. This high precision waveform than allows the computation of various functionals $F(\tilde{\psi}(s))$ appearing in theories describing the axonemal beat, with the uncertainty in these functionals still being reasonably small to allow to test certain predictions of these theories.

In case where the beating is rather erratic instead of periodic this automated detection algorithm allows the measurement of long time series (in the order of 30.000 frames being the limit of the camera used), which could be used for time series analysis to study this erratic behavior.

A2 Self-organized vortex array

Order parameter

In this section I investigate the relationship between the order parameter χ and the pair-correlation function in the case of cycling sperm. I find that both carry the same information with respect to the packing order and the bifurcation. Furthermore I demonstrate that χ is robust in its information content against changes in the parameters used to compute χ . This makes χ a useful tool for studies of systems involving trails of multiple particles or signals.

Note that the tracks in other studied systems do not have to be circular. Any shape of trace is possible. Generally, χ measures whether the trails are random or correlated. Furthermore χ is also sensitive to anti-correlation, e.g. when similar path are explicitly avoided. The precise meaning and usage of χ in a particular system has to be checked with control data.

Measuring order among point particles: pair-correlation function

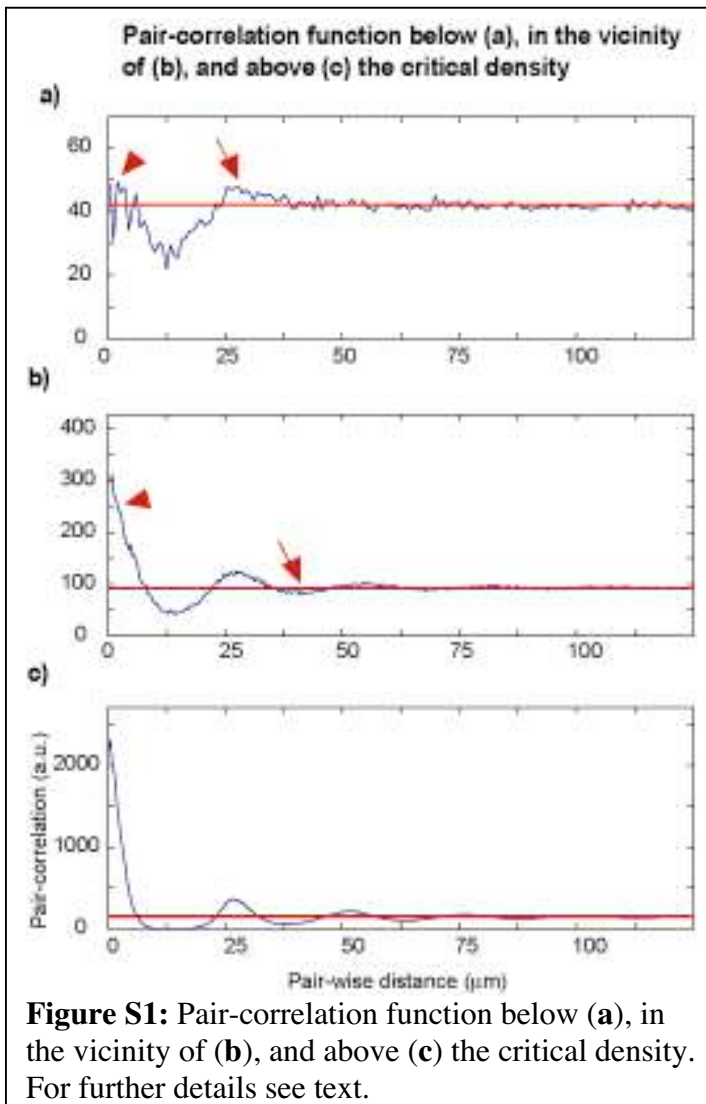
A standard analysis tool for the description of point-particles is the pair-correlation function $g_2(r)$:

$$g_2(r \pm dr) = \frac{1}{r} \sum_i \sum_{j>i} \Theta(|\bar{r}_i - \bar{r}_j| - r + dr / 2) \cdot \Theta(r + dr / 2 - |\bar{r}_i - \bar{r}_j|), \quad \text{Eq. S1}$$

where r is the pair-wise distance of the point-particles, Θ is the Heavyside function, \bar{r}_i are the center positions of the particles, i and j are the indices running over all particles, and dr is the bin-width of the histogram.

The pair-correlation function measures the probability of finding a particle at a given distance from another one. Fig. S1a-c show the pair-correlation functions (blue) for the model simulation corresponding to three different densities. These densities are chosen such that one is below (Fig. S1a), one in the vicinity (Fig. S1b), and one far above (Fig. S1c) the critical density. The red lines correspond to the pair-correlation for a homogenous particle distribution at the same total particle density.

Below the critical density (Fig. S1a, 500 particles/mm²) the distribution is



homogenous except close to the origin. The two peaks (arrow and arrowhead) with the sandwiched minimum are determined by the interaction potential among the particles. If a particle diffuses towards another it has a lower probability of staying in the high potential region. It gets pushed away into regions of lower potential where the probability increases.

At the critical density (Fig. S1b, 2400 particles/mm²) a second minimum shows up (arrow), followed by further maximums and minima with rapidly decaying amplitudes. Furthermore the peak at zero increases in its relative height to the average (arrowhead). The

emergence of the second minimum and the increase of the maximum at the origin indicate the formation of clusters of particles, and the onset of packing of these clusters, respectively.

At densities much higher than the critical density (Fig. S1c, 5700 particles/mm²) the peak at zero has become very sharp, indicating that the particles within a cluster are tightly packed. Furthermore, the alternating minima and maximums have become more pronounced.

To summarize, the critical density where the formation of clusters and their closed packing sets in can be read off from the pair-correlation function by measuring the heights of the zero peak and the second minimum relative to the average pair-correlation.

Definition of χ

In this paragraph I define in mathematical terms how the order parameter χ is computed.

Consider a stack of N binary frames of size X by Y pixels, let $F(x,y,n)$, where $x=1,\dots,X$, $y=1,\dots,Y$, $n=1,\dots,N$, denote the occupancy of the pixel at position (x,y) of the n^{th} frame. Here, $F=0$ for an unoccupied pixel and $F=1$ in the opposite case. The relative intensity in each frame is given by

$$p(n) = \frac{\sum_x \sum_y F(x,y,n)}{X \cdot Y} \quad \text{Eq. S2}$$

Here $p(n)$ is a real number between 0 and 1. The quantity $p(n)$ is the probability for a pixel being set to 1. $p(n)$ is independent of the frame number n as the number of objects and hence of occupied pixels is the same in all frames, that is $p(n)=p$ for all n .

The number of frames a pixel is occupied is given by

$$A(x,y) = \sum_n F(x,y,n) \quad \text{Eq. S3}$$

where $A(x,y)$ is an integer between 0 and N for all x and y . $A(x,y)=0,\dots,N$ and $A(x,y)$ being integer values. Let H_m be the histogram of the values in $A(x,y)$. If the distribution of the objects within the stack were random the entries in the histogram would be distributed according to a binomial distribution H_b , where $H_b(a) = p^a (1-p)^{N-a}$ with $0 \leq a \leq N$.

To measure the amount of order of the objects in the stack I compare the two histograms H_m and H_b . Both distributions have the same expectation value $p \cdot N$, but differ in the variances σ_m^2 and σ_b^2 respectively. From these variances I define the order parameter χ as:

$$\chi = \sigma_m^2 / \sigma_b^2 - 1 . \quad \text{Eq. S4}$$

The subtraction of 1 ensures that χ is zero for a random distribution.

Relation between pair-correlation function and order parameter χ

I investigated the relation between the pair-correlation function and the order-parameter χ by computing both for the simulated data presented in Fig.4e in the paper. I found that the height of the zero peak in the correlation function (Fig. S2a), the height of the second minimum in the correlation function (Fig. S2b), and χ itself (Fig. S2c) all indicate the same general dependence on the particle density: An initial plateau phase is followed by a transition towards an increasing phase with a constant slope. The transition happens at the same density (dashed red lines). Plotting all three variables pair-wise

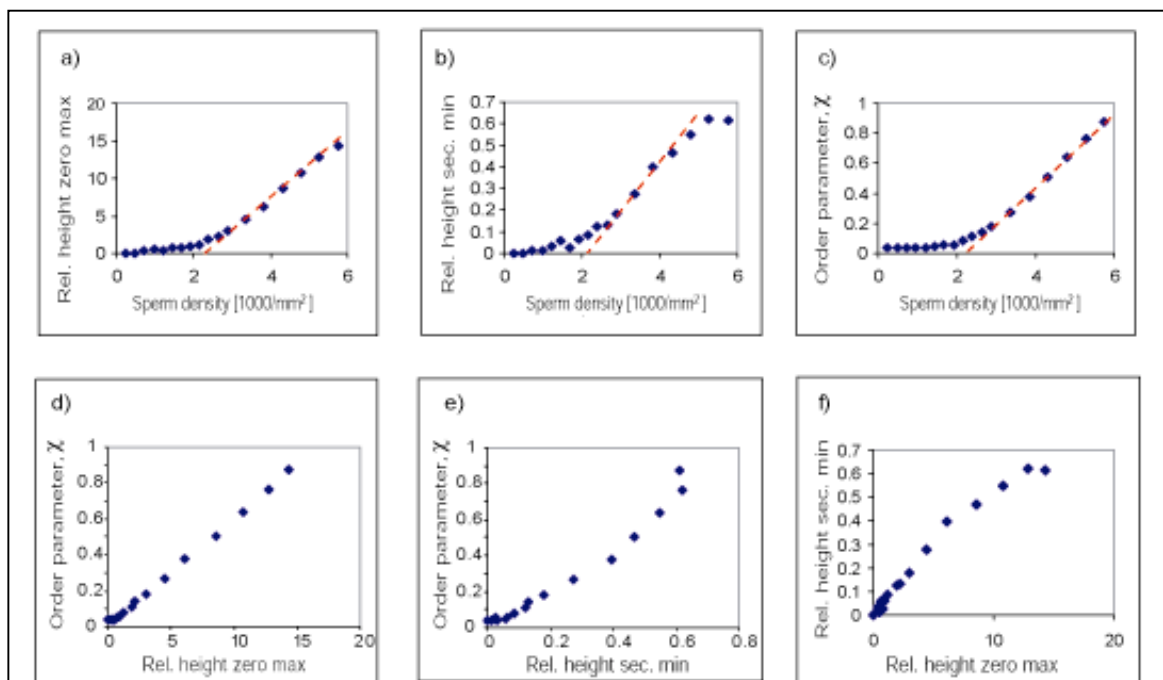


Figure S2: Relation between pair-correlation function (PCF) and order parameter χ . **a**, Relative height of the zero maximum of the PCF vs. sperm density. **b**, Relative height of the second minimum of the PCF vs. sperm density. **c**, Order parameter χ vs. sperm density. **d**, Relative height of the zero maximum of the PCF vs. order parameter χ . **e**, Relative height of the second minimum of PCF vs. order parameter χ . **f**, Relative height of the second minimum of the PCF vs. relative height of the zero maximum of PCF. (a-c) Crossing point between dashed red lines and the zero order parameter indicate the critical values.

against each other (Fig. S2d-f) I find correlations between them. The only exception is the second minimum, which levels off at higher densities. This can be understood from the

fact that at very high ordered states the second minimum in the pair-correlation becomes zero and therefore does not change anymore with increasing overall density.

The relation between the order parameter χ and the pair-correlation function can be understood as follows. The peak at zero in the pair-correlation function is equal to the convolution of the average particle density of a cluster with itself. Then from the total particle density and the average particle density within a cluster the statistics of spatial particle configurations can be deduced. For this statistic and the parameter choices used in the experiments, e.g. frame rate, number of frames, size of the objects, the corresponding χ can be found.

I conclude that χ and the pair-correlation function contain the same information with respect to the clustering and packing order for the simulated data.

Robustness of χ

Next I discuss how χ depends on the parameters needed to compute it from the experimental data. These parameters are the head size of the sperm, the number of frames used for the summing up process, and the frame rate of the movies.

To test these influences I used the simulated data on which Fig. 4e in the paper was based on. I studied the influence of each parameter by increasing and decreasing its value by 50%. From this data I computed the corresponding dependencies of χ on sperm density. I explicitly tested:

1. Head size of sperm: The size was varied between 2x2, 4x4, and 6x6 pixels, 4x4 pixels being the one used for all simulation and corresponding very closely to the experimental data.

2. Number of frames added up: The number was varied between 5, 10, and 15 frames, 10 being the ones used for all simulation and the experimental data. For the experimental data 10 frames correspond on average to a full swimming cycle of a sperm. This is in contrast to 5 frames, where two sperms swimming in the same vortex might not overlap at all, and 15 frames, where individual sperm swim over their own path and hence leading to self-overlap.

3. Frame rate at which the movies were acquired: The frame rate was varied between 8.5, 17, and 25.5 frames per second (fps). For the all simulations and experimental data 17 fps were used. For the frame rate of 17 fps a sperm head has moved on average so much not to overlap with itself in successive frames but also not leaving a large gap.

Fig. S3a shows χ vs. particle density for all these scenarios. I find that the absolute value of χ depends on each of the chosen parameters. But all curves contain initial plateau followed by an approximately linear increase starting at the same density. Fitted lines through the data points (not shown) in each phase intersect at the same critical density (arrow). Hence there is a critical density and its values is independent of the parameter choice.

Fig. S3b shows the pair-wise correlation between χ calculated with the original parameter choice vs. χ for each one of the parameters changed. I find linear dependencies

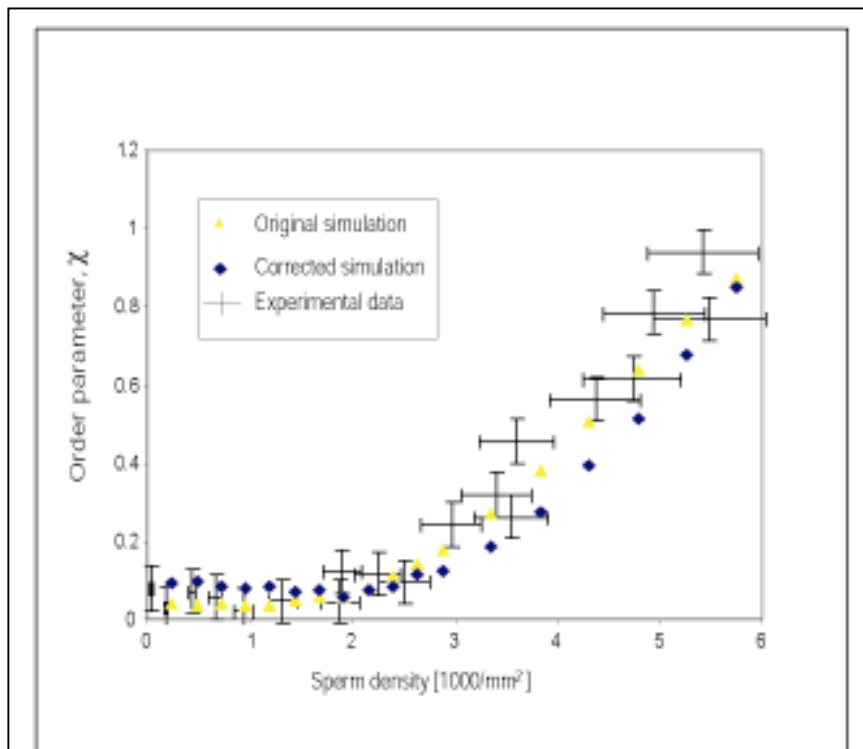


Figure S3: a, Comparison of different parameter sets used for computation of the order parameter χ b, Correlation among order parameter χ computed with different parameter sets.

between all of them. I interpret that a certain chosen parameter set has a systematic influence. Any parameter set systematically over- or underestimates the amount of trailing in the system. But the information content for a given parameter set is very robust. The order in the system

and the transition point are revealed for all different parameter choices as long as they are kept constant in a series of experiments. Furthermore it is advantageous to minimize these systematic influences by aiming at a parameter choice where the self-overlap is minimized. This was also the rationale in my parameter choice.

Error estimates on the order parameter χ

During the course of the experiment presented in Fig. 4 not only the surface sperm density changed. Also the circling radius of the spermatozoa changed from initially $R=33.1 \pm 8.3 \mu\text{m}$ to $R=14.8 \pm 2.0 \mu\text{m}$. The same effect is observed for isolated spermatozoa and is very likely due to the lack of Ca^{2+} in the artificial seawater, which is known to influence the asymmetry of the waveform (see ref.(Brokaw 1986)). Hence this effect is independent of the pattern formation. Furthermore the swimming speed changed from $v=123 \pm 16 \mu\text{m/s}$ to $v=99 \pm 27 \mu\text{m/s}$, presumably due to the use-up of the internal ATP.

This raises the questions, how these changes influence the order parameter χ . As discussed in the proceeding analysis of this supplementary material, the order parameter χ measures the correlation among the paths of particles independently of the shape of these paths, hence also at different swimming radii. Furthermore, it was shown, that a given parameter set needed to compute χ is optimized for the characteristics of the particle motion such as the swimming speed. If these parameters are not chosen optimally, systematic errors onto the value of χ are introduced. If for instance a sperm swims much slower than expected, then it overlaps in successive frames with itself and hence the amount of trailing is overestimated. If now the swimming characteristics of the objects during the course of the experiment change – as radii and swimming speed in my case – not all χ are measured on equal footing. Therefore I analyzed, how much uncertainty in χ is associated with these changes in the circling radii and swimming velocity.

Initially I estimated the error in χ by evaluating different areas within a movie separately and doing statistics on them. The error on the sperm density was estimated the same way. Since the variations in χ found by the controls described below were slightly larger in some cases (within a factor of two) I doubled the initially estimated error on χ .

These error bars are the ones shown in Fig. S4 (black crosses), as well as in the paper in Fig. 4c.

I did the following controls. First, I generated simulated data as described in the paper, but now the circling radius and the swimming velocity were adjusted accordingly

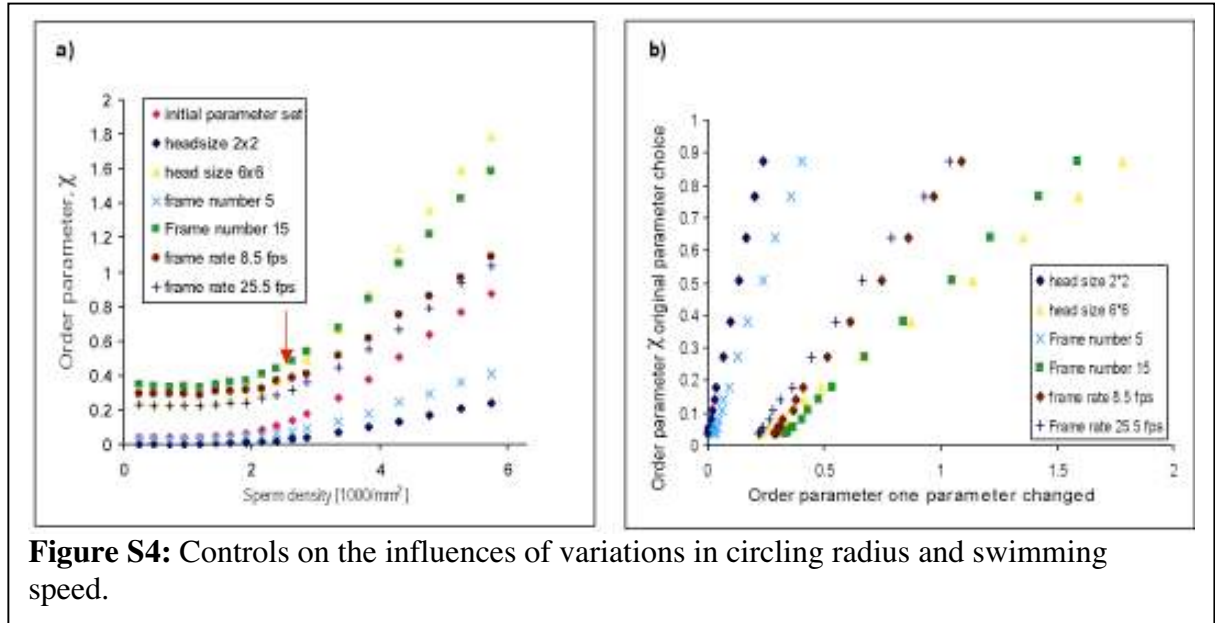


Figure S4: Controls on the influences of variations in circling radius and swimming speed.

with density as observed in the experiment. As can be read off from Fig. S4 this leads to changes in the absolute value of the order parameter χ that are in the same range as the fluctuations among experimental measurements. Second, I estimated the influence accordingly to the conclusions drawn in Fig. S3 (data not shown). Again I found that changes are comparatively small. Third, I computed χ for the experimental data with the larger swimming radii by averaging over 25 frames instead of 10. (If the radius is larger it takes more frames for a sperm to complete a full circle.) The results agreed with the initial ones (data not shown). To conclude, the initial plateau, the transition and then the increase in χ was revealed for all controls and hence is a real feature of the experimental data and also of the pattern forming process.

Finally I want to point out that the circling radius might influence the interactions among the spermatozoa and hence the critical density might change as well, depending what the actual radius at the bifurcation point was. I estimated this effect to be within a factor of 1/2-2, leaving my earlier conclusions unchanged.

Mean field description

In this section I perform a meanfield analysis of the model in one spatial dimension. In the meanfield limit, the state of the system is given by the particle density ρ . The evolution in time of the density is given by

$$\begin{aligned} \partial_t \rho(x,t) &= D \partial_x^2 \rho(x,t) - \partial_x J(x,t) \\ J(x,t) &= \rho(x,t) \zeta^{-1} \int_{-2R}^{2R} dx' \rho(x+x',t) V(x',t) \end{aligned} \quad \text{Eq. S5}$$

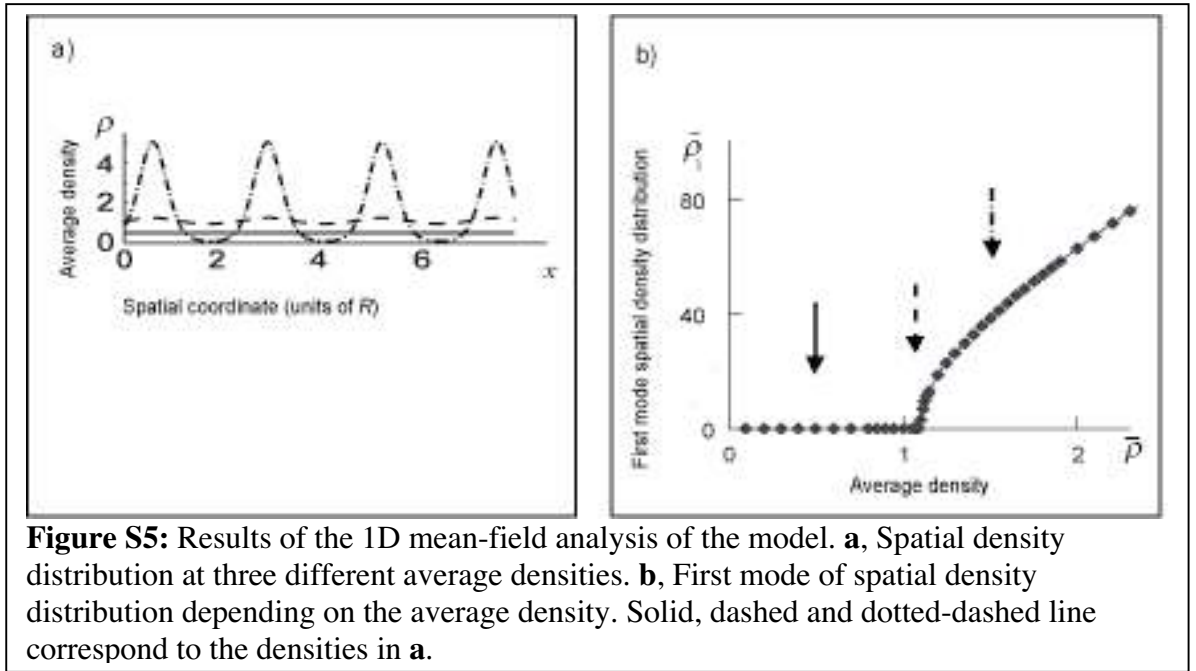


Figure S5: Results of the 1D mean-field analysis of the model. **a**, Spatial density distribution at three different average densities. **b**, First mode of spatial density distribution depending on the average density. Solid, dashed and dotted-dashed line correspond to the densities in **a**.

where t is time, x is position, D is the diffusion constant, J is the density current, ζ is a constant with dimensions of a friction constant, and V the interaction potential.

The interaction potential is given by
$$V(r) = \begin{cases} V_0 \cdot |r| & |r| < R \\ V_0 \cdot (2R - |r|) & R < |r| < 2R \\ 0 & |r| > 2R \end{cases} \quad (\text{see also Fig. 4d), where } r \text{ is the pair-wise distance.}$$

Note, however, that the qualitative behavior of the model is independent of the detailed shape of the potential, but depends only on some of its features, such as the existence of an attractive and a repulsive part, furthermore the minimum at the origin being not below zero.

The homogenous density distribution $\rho = \rho_0$ is a stationary state of the dynamics. Now I analyze the stability of this state with respect to small sinusoidal perturbation. I find that a critical density exists. Below that critical density the perturbation decays and the homogenous distribution is stable. Above the critical density the perturbation increases and an inhomogenous stationary solutions appears. This transition is categorized further to be a supercritical pitchfork bifurcation (Strogatz 2000).

The following relation governs the critical point:

$$\rho \cdot \frac{V_0}{D} \cdot \frac{R}{\zeta} = 1.05 \quad \text{Eq. S6}$$

The first wavelength that becomes unstable is determined by the following equation:

$$k_c = \frac{2 \cos k_c (\cos k_c - 1)}{\sin k_c (1 - 2 \cos k_c)}, \quad \text{Eq. S7}$$

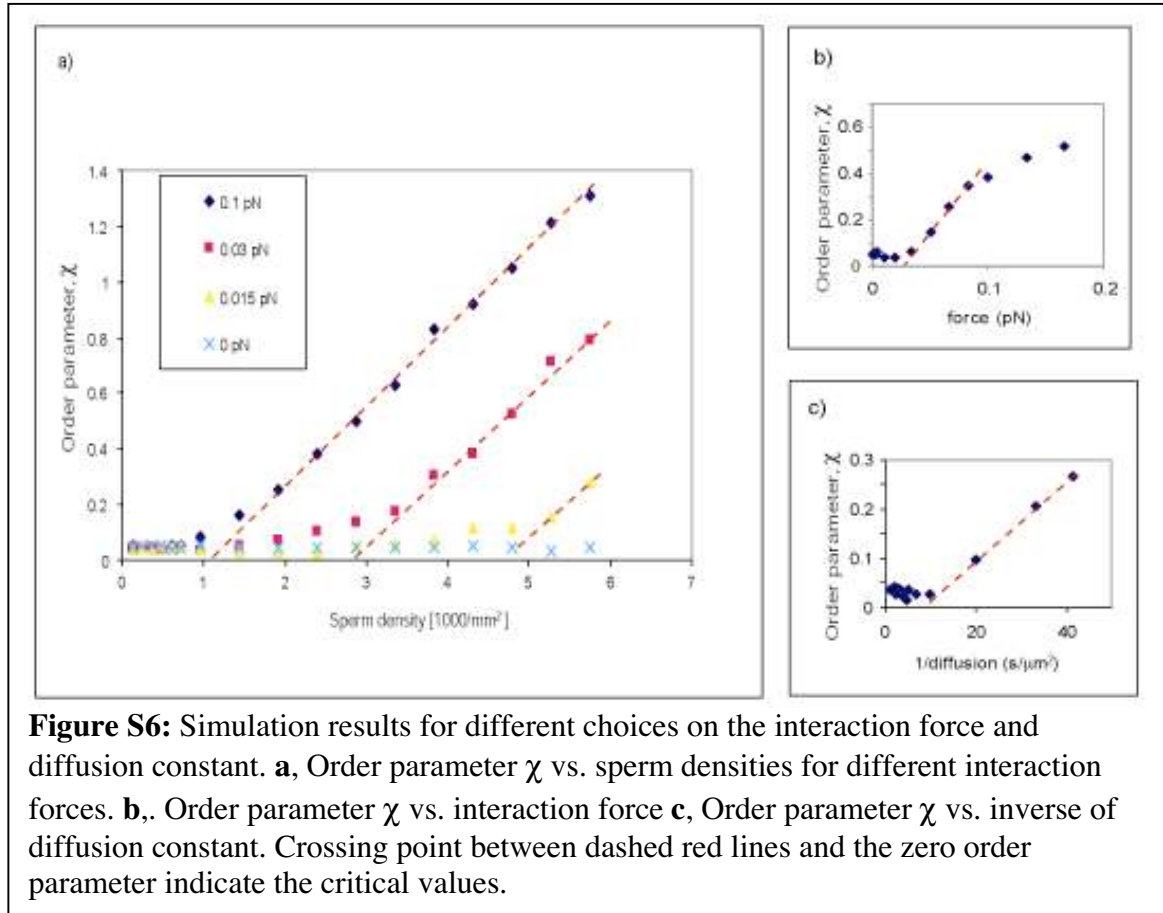
which has the solution $k_c = 2.67$.

Fig. S5a shows the spatial density distribution at three different average distributions (below, very close but above, and far above the critical density). Fig. S4b shows the amplitude of the first spatial Fourier mode. In the vicinity of the bifurcation point it increases with a square-root dependence, which is generic for a supercritical pitchfork bifurcation. The arrows (solid, dashed, and dotted-dashed) correspond to the densities shown in Fig. S1a. The solutions shown in Fig. S5 were obtained by numerical integration of Eq. S5. A one-dimensional box with periodic boundary conditions and size $32R$ was chosen.

The relation in Eq. S6 states that the bifurcation can set in by changing any one of these parameters, not only by varying the density as done experimentally. I tested whether this relation is compatible with the simulated data from simulations with the 2D model presented in the paper (same as described in Methods, except this time only 300 particles were used). Fig. S6a shows χ vs. density for four different forces. (Here the force is related to the potential by the relation $F = -grad(V) = -V_0 / R$.) The critical density (arrows) changes with the force. For zero force I do not find a critical density at all. I also notice that for zero force χ is the same at all densities. Hence χ is not an artifact due to the

particle density; instead it depends on the order among the particles as already shown in the previous section of this supplementary material.

If I keep the diffusion constant and the density fixed, but vary the force I also find



a transition (Fig. S6b). The same holds if I fix the force and the density but vary the diffusion coefficient (Fig. S6c). Therefore I find a qualitative agreement between the 2D simulation presented in the paper and the analytical 1D analysis presented in the supplements.

To conclude, the 1-D mean-field description of the model predicts a supercritical pitchfork bifurcation. This bifurcation is associated with a transition from a homogenous distribution to a periodic arrangement of regions with higher densities separated by regions with lower densities. In my 2D simulation this corresponds to the formation of hexagonal arranged clusters. These clusters correspond to the experimentally observed formation of closely packed vortices containing about 10 sperm.

A3 Supplementary movies

Movie V1: Phase contrast movie showing a bull spermatozoon clamped at its head to the surface beating at 20Hz. Scale: Length of head is about 10 μm . Original frame rate: 250 fps; replay: 5 fps. (QuickTime; 0.7 MB)

Movie V2: Phase contrast movie showing a bull spermatozoon hinged at its head to the surface beating at 20Hz. Scale: Length of head is about 10 μm . Original frame rate: 250 fps; replay: 5 fps. (QuickTime; 0.5 MB)

Movie V3: Phase contrast movie showing a bull spermatozoon swimming close to a surface and beating at 20Hz. Scale: Length of head is about 10 μm . Original frame rate: 250 fps; replay: 10 fps. (QuickTime; 3.4 MB)

Movie V4: Phase contrast movie showing a bull spermatozoon swimming close to a surface at approx. 10 fold increased viscosity. Note the shorter wavelength on the tail compared to Movie V3. The frame size demonstrates the maximum field of view of the used camera. Scale: Length of head is about 10 μm . Original frame rate: 250 fps; replay: 30 fps. (QuickTime; 8.9 MB)

Movie V5: Phase contrast movie showing a bull spermatozoon clamped to a suction needle that is driven by a piezo. The driving frequency is 12 Hz while the spermatozoon is beating with approximately 20 Hz. Scale: Length of head is about 10 μm . Original frame rate: 250 fps; replay: 10 fps. (QuickTime; 8.9 MB)

Movie V6: Phase contrast movie showing a human spermatozoon attached to the surface. Scale: Length of head is about 10 μm . Original frame rate: 250 fps; replay: 15 fps. (QuickTime; 18.2 MB)

For the movies **M1** to **M5** the circling motion of the spermatozoa appears clockwise or anti-clockwise in the videos, depending on whether the spermatozoa were imaged at the upper or lower surface. From inside the water-phase the spermatozoa always appear to circle clockwise.

Movie M1: Dark field movie showing a vortex array of sperm cells at a surface density of 6000 cells/mm². Scale: Length of head is about 10 μm. Original frame rate: 250 fps; replay: every 8th frame shown at 30 fps hence roughly real time. (QuickTime; 5.1 MB)

Movie M2: Same movie as (**Movie M1**), but replayed slower. Original frame rate: 250 fps; replay: all frames shown at 10 fps. (QuickTime; 3.8 MB)

Movie M3: Phase contrast movie showing a single spermatozoon swimming close to a surface. Scale: Length of head is about 10 μm. Original frame rate: 250 fps; replay: all frames at 7.5 fps. (QuickTime; 1 MB)

Movie M4: Phase contrast movie showing seven spermatozoa within a single vortex at a surface density of 4000 cells/mm². This movie was used for the data presented in Fig.3. Scale: Length of head is about 10 μm. Original frame rate: 250 fps; replay: all frames at 15 fps. (QuickTime; 9 MB)

Movie M5: Dark field contrast movies at different sperm surface densities (700, 2500, 4700 cells/mm²) corresponding to values below, in the vicinity of, and above the critical density. These movies (among others) were used to generate the data in Fig.4e. Original frame rate: 17 fps; replay: all frames shown at 15 fps. (QuickTime; 6.1 MB)

List of Figures

Figure 1: Cilia and flagella contain an axoneme and show dynamic wave patterns.

Figure 2: The essential structure of cilia and flagella is the axoneme.

Figure 3: The mammalian flagellum varies along its length.

Figure 4: The wave-patterns of cilia and flagella are different.

Figure 5: The different cytoskeletal motors as seen by EM.

Figure 7: The hydrolysis cycle of kinesin.

Figure 8: The hydrolysis cycle cytoplasmic dynein.

Figure 9: The complex structure of the axoneme is reduced to a pair of sliding filaments.

Figure 10: The beating pattern of a bull spermatozoon is automatically detected and converted into an angular representation.

Figure 11: A Fourier analysis in time reveals that the beating pattern of a spermatozoon can be described by its first eigenmode, furthermore the waves travel with similar velocity along the whole tail.

Figure 12: An averaged beating pattern $\psi(s,t)$ at high precision is obtained that allows the test of theoretical predictions.

Figure 13: The experimental data is fitted to the theory.

Figure 14: The fitted waveforms $\tilde{\psi}(s)$ are in good agreement with the experimental data.

Figure 15: Circulating spermatozoa from *S. droebachiensis* form a two-dimensional array of vortices.

Figure 16: The vortex array shows local hexagonal order and is liquid-like.

Figure 17: Hydrodynamic coupling among spermatozoa within a vortex leads to quantized rotating waves.

Figure 18: The formation of the vortex array at a critical sperm density is associated with a bifurcation.

List of Tables

Table 1: Comparison of fit parameters and their expected values for the different fits.

List of Movies

Movie V1: Bull spermatozoon clamped at its head.

Movie V2: Bull spermatozoon hinged at its head.

Movie V3: Bull spermatozoon swimming close to a surface.

Movie V4: Bull spermatozoon swimming close to a surface at increased viscosity.

Movie V5: Bull spermatozoon clamped to a suction needle that is driven by a piezo.

Movie V6: Human spermatozoon attached to the surface.

Movie M1: Vortex array of sperm cells at a surface density of 6000 cells/mm².

Movie M2: Same movie as (**Movie M1**), but replayed slower.

Movie M3: Single sea urchin spermatozoon swimming close to a surface.

Movie M4: Seven spermatozoa within a single vortex.

Movie M5: Movies at different sperm surface densities below, in the vicinity of, and above the critical density.

List of Publications

“Self-organization of hydrodynamically entrained sperm cells into an array of vortices”

I. Riedel, K. Kruse, and J. Howard

Submitted

“Ab initio calculation of the transmission coefficients from a superlattice electronic structure”

I. Riedel, P. Zahn, and I. Mertig

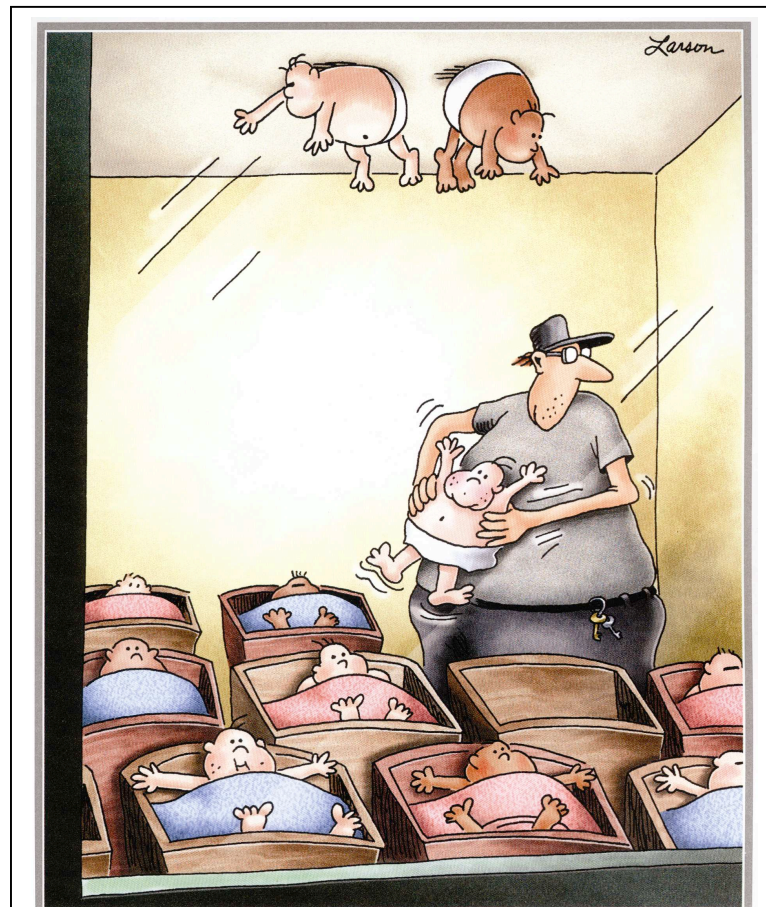
Phys. Rev. B **63**, 195403 (2001)

Acknowledgements

I want (and also have) to thank the following people in helping me to make this thesis happening:

- Jonathon “Joe” Howard for allowing me to work on such a “sexy” project, for his enthusiasm, the flat hierarchies, all the wonderful calculations on smallest sheets of paper (and other materials) and also for his really great support on personal concerns
- Frank Jülicher for being a full second supervisor, his constant interest in my work, and for integrating me in the activities of his group such as the Ski-minars
- Prof. Soff, Michael Meyer-Hermann and Petra Schwille for supervision at different phases of my thesis
- Andreas “Andy” Hilfinger, for joining me on this ride, preventing me from collapsing on “just” mathematical details, the great support at the very end and for all the dinners that we still owe each other
- Karsten Kruse for many discussions, but especially for enlightening me that self-organized vortex arrays are really the thing that everyone wants know about
- The whole Howard lab with all its former and present members; especially Regine and Anja for keeping the lab from gaining maximum entropy, furthermore Alvaro and Khaled for endless discussions on Matlab etc, finally Sunny for the (not so) bluesy coffees
- The men from the hill (MPI-PKS) for giving a lost son the spirit of real physics
- Donner Babcock, Charles Brokaw, Raymond Goldstein, Charles Lindemann, Hans Machemer, Karin Müller, Francois Nedelec for their interest in my work, their support and many discussions
- Diverse people from the MPI-CBG (Fish facility, Ronald, Hartmut, Robert,...)
- Everyone I forgot at 4.30 in the morning...
- All members of “Herrengedeck Strehlen” – we will rock!
- PD Dr. Reinhard Rachel for being a great “Patentonkel” and paving my way into science

- My parents for all their love, for not preventing me from going into science and instead even financing it – indirectly still today, because how to keep up the live style with a family on BAT IIa/2?
- And most important my very recently formed family – combining kids and science can be easy (see cartoon) or ... : I really thank Dana for her love, her support on my science addiction, for buying me all this chocolate, and for putting my sperm into good use – which brings my final acknowledgments to Luzy (you are a happy kid and an (almost) reliable sleeper from 8 to 7.30 - Why did you give up on this just during the last three weeks?) and to the Keks (who was really holding back her interest in the real world before I am done with everything).



Late at night, and without permission, Reuben would often enter the nursery and conduct experiments in static electricity.

Reproduced (also without permission) from (Larson 2004).

Bibliography

- Allen, W. (1980). Complete Prose. London, Picador.
- Ben-Jacob, E., I. Cohen, et al. (2000). "Cooperative self-organization of microorganisms." Advances in Physics 49(4): 395-554.
- Berg, H. C. (1993). Random Walks in Biology. Princeton, NJ, Princeton University Press.
- Blum, J. J. and M. Hines (1979). "Biophysics of flagellar motility." Q Rev Biophys 12(2): 103-80.
- Brady, S. T. (1985). "A novel brain ATPase with properties expected for the fast axonal transport motor." Nature 317(6032): 73-5.
- Brennen, C. and H. Winet (1977). "Fluid-Mechanics of Propulsion by Cilia and Flagella." Annual Review of Fluid Mechanics 9: 339-398.
- Brokaw, C. J. (1961). "Movement and Nucleoside Polyphosphatase Activity of Isolated Flagella from *Polytoma Uvella*." Experimental Cell Research 22: 151-&.
- Brokaw, C. J. (1971). "Bend propagation by a sliding filament model for flagella." J Exp Biol 55(2): 289-304.
- Brokaw, C. J. (1972). "Computer simulation of flagellar movement. I. Demonstration of stable bend propagation and bend initiation by the sliding filament model." Biophys J 12(5): 564-86.
- Brokaw, C. J. (1975). "Molecular mechanism for oscillation in flagella and muscle." Proc Natl Acad Sci U S A 72(8): 3102-6.
- Brokaw, C. J. (1984). "Automated methods for estimation of sperm flagellar bending parameters." Cell Motil 4(6): 417-30.
- Brokaw, C. J. (1986). "Sperm motility." Methods Cell Biol 27: 41-56.
- Brokaw, C. J. (1989). "Direct measurements of sliding between outer doublet microtubules in swimming sperm flagella." Science 243(4898): 1593-6.
- Brokaw, C. J. (1991). "Microtubule sliding in swimming sperm flagella: direct and indirect measurements on sea urchin and tunicate spermatozoa." J Cell Biol 114(6): 1201-15.
- Brokaw, C. J. (1993). "Microtubule sliding in reduced-amplitude bending waves of *Ciona* sperm flagella: resolution of metachronous and synchronous sliding components of stable bending waves." Cell Motil Cytoskeleton 26(2): 144-62.
- Brokaw, C. J. (1996). "Microtubule sliding, bend initiation, and bend propagation parameters of *Ciona* sperm flagella altered by viscous load." Cell Motil Cytoskeleton 33(1): 6-21.
- Brokaw, C. J. and S. M. Nagayama (1985). "Modulation of the asymmetry of sea urchin sperm flagellar bending by calmodulin." J Cell Biol 100(6): 1875-83.
- Burgess, S. A., M. L. Walker, et al. (2003). "Dynein structure and power stroke." Nature 421(6924): 715-8.
- Camalet, S. and F. Julicher (2000). "Generic aspects of axonemal beating." New Journal of Physics 2: 1-23.
- Camalet, S., F. Julicher, et al. (1999). "Self-Organized Beating and Swimming of Internally Driven Filaments." Physical Review Letters 82: 1590-1593.
- Cross, M. C. and P. C. Hohenberg (1993). "Pattern-Formation Outside of Equilibrium." Reviews of Modern Physics 65(3): 851-1112.

- Darnton, N., L. Turner, et al. (2004). "Moving fluid with bacterial carpets." Biophys J 86(3): 1863-70.
- Dombrowski, C., L. Cisneros, et al. (2004). "Self-concentration and large-scale coherence in bacterial dynamics." Physical Review Letters 93(9): 098103.
- Fauci, L. J. and A. McDonald (1995). "Sperm motility in the presence of boundaries." Bull Math Biol 57(5): 679-99.
- Fawcett, D. W. (1975). "The mammalian spermatozoon." Dev Biol 44(2): 394-436.
- Gibbons, B. H. and I. R. Gibbons (1969). "Reactivation of Sea Urchin Sperm after Extraction with Triton X-100." Journal of Cell Biology 43(2P2): A43-&.
- Gibbons, B. H. and I. R. Gibbons (1972). "Flagellar movement and adenosine triphosphatase activity in sea urchin sperm extracted with triton X-100." J Cell Biol 54(1): 75-97.
- Gibbons, B. H. and I. R. Gibbons (1973). "Effect of Partial Extraction of Dynein Arms on Movement of Reactivated Sea-Urchin Sperm." Journal of Cell Science 13(2): 337-357.
- Gibbons, B. H. and I. R. Gibbons (1974). "Properties of flagellar "rigor waves" formed by abrupt removal of adenosine triphosphate from actively swimming sea urchin sperm." J Cell Biol 63(3): 970-85.
- Gibbons, B. H. and I. R. Gibbons (1980). "Calcium-induced quiescence in reactivated sea urchin sperm." J Cell Biol 84(1): 13-27.
- Gibbons, I. R. (1981). "Cilia and flagella of eukaryotes." J Cell Biol 91(3 Pt 2): 107s-124s.
- Gibbons, I. R. and A. J. Rowe (1965). "Dynein - a Protein with Adenosine Triphosphatase Activity from Cilia." Science 149(3682): 424-&.
- Gibbons, I. R., C. Shingyoji, et al. (1987). "Spontaneous recovery after experimental manipulation of the plane of beat in sperm flagella." Nature 325(6102): 351-2.
- Gittes, F., B. Mickey, et al. (1993). "Flexural rigidity of microtubules and actin filaments measured from thermal fluctuations in shape." J Cell Biol 120(4): 923-34.
- Gray, J. (1928). Ciliary movement, Cambridge University Press.
- Gray, J. (1955). "The Movement of Sea-Urchin Spermatozoa." Journal of Experimental Biology 32(4): 775-800.
- Gray, J. (1958). "The Movement of the Spermatozoa of the Bull." Journal of Experimental Biology 35(1): 96-&.
- Gray, J. and G. J. Hancock (1955). "The Propulsion of Sea-Urchin Spermatozoa." Journal of Experimental Biology 32(4): 802-814.
- Grill, S. W., F. Julicher, et al. (2005). "Theory of Mitotic Spindle Oscillations." Physical Review Letters In Press.
- Grzybowski, B. A. and G. M. Whitesides (2002). "Dynamic aggregation of chiral spinners." Science 296(5568): 718-21.
- Gueron, S. and K. Levit-Gurevich (1998). "Computation of the internal forces in cilia: Application to ciliary motion, the effects of viscosity, and cilia interactions." Biophysical Journal 74(4): 1658-1676.
- Hancock, G. J. (1953). "The Self-Propulsion of Microscopic Organisms through Liquids." Proceedings of the Royal Society of London Series a-Mathematical and Physical Sciences 217(1128): 96-121.
- Hill, T. L. (1974). "Theoretical formalism for the sliding filament model of contraction of striated muscle. Part I." Prog Biophys Mol Biol 28: 267-340.

- Hines, M. and J. J. Blum (1979). "Bend propagation in flagella. II. Incorporation of dynein cross-bridge kinetics into the equations of motion." *Biophys J* 25(3): 421-41.
- Hodgkin, A. L. and A. F. Huxley (1952). "A quantitative description of membrane current and its application to conduction and excitation in nerve." *J Physiol* 117(4): 500-44.
- Hoelldobler, B. and E. O. Wilson (1990). *The ants*. Berlin, Springer.
- Hoffmann-Berling, H. (1955). "[Flagellum models and adenosinetriphosphate (ATP)]." *Biochim Biophys Acta* 16(1): 146-54.
- Hollenbeck, P. (1989). "Cell motility. Dissecting a molecular motor." *Nature* 338(6213): 294-5.
- Holwill, M. E. and J. L. McGregor (1976). "Effects of calcium on flagellar movement in the trypanosome *Crithidia oncopelti*." *J Exp Biol* 65(1): 229-42.
- Howard, J. (2001). *Mechanics of Motor Proteins and the Cytoskeleton*. Sunderland, Sinauer Associated Inc.
- Huxley, H. E. (1957). "The double array of filaments in cross-striated muscle." *J Biophys Biochem Cytol* 3(5): 631-48.
- Insall, R. and L. Machesky (1999). Cytoskeleton. *Nature Encyclopedia of Life Sciences*, London: Nature Publishing Group.
- Johnson, K. A. (1983). "The pathway of ATP hydrolysis by dynein. Kinetics of a presteady state phosphate burst." *J Biol Chem* 258(22): 13825-32.
- Julicher, F. and J. Prost (1997). "Spontaneous oscillations of collective molecular motors." *Physical Review Letters* 78(23): 4510-4513.
- Kamimura, S. and R. Kamiya (1989). "High-frequency nanometre-scale vibration in 'quiescent' flagellar axonemes." *Nature* 340(6233): 476-8.
- Kaupp, U. B., J. Solzin, et al. (2003). "The signal flow and motor response controlling chemotaxis of sea urchin sperm." *Nat Cell Biol* 5(2): 109-17.
- Kon, T., M. Nishiura, et al. (2004). "Distinct functions of nucleotide-binding/hydrolysis sites in the four AAA modules of cytoplasmic dynein." *Biochemistry* 43(35): 11266-74.
- Landau, L. D. and E. Lifshitz, M. (1987). *Fluid Mechanics*. Oxford, Pergamon Press.
- Larson, G. (2004). *The Far Side Calendar*. Missouri, Andrews McMeel Publishing.
- Lenz, P., J. F. Joanny, et al. (2003). "Membranes with rotating motors." *Physical Review Letters* 91(10): 108104.
- Linck, R. W. (2001). Cilia and Flagella. *Nature Encyclopedia of Life Sciences*, London: Nature Publishing Group.
- Lindemann, C. B. (1994). "A model of flagellar and ciliary functioning which uses the forces transverse to the axoneme as the regulator of dynein activation." *Cell Motil Cytoskeleton* 29(2): 141-54.
- Lindemann, C. B. and A. J. Hunt (2003). "Does axonemal dynein push, pull, or oscillate?" *Cell Motility and the Cytoskeleton* 56(4): 237-244.
- Lindemann, C. B. and K. S. Kanous (1995). "'Geometric clutch' hypothesis of axonemal function: key issues and testable predictions." *Cell Motil Cytoskeleton* 31(1): 1-8.
- Lindemann, C. B., W. G. Rudd, et al. (1973). "The stiffness of the flagella of impaled bull sperm." *Biophys J* 13(5): 437-48.
- Machemer, H. (1972). "Ciliary activity and the origin of metachrony in *Paramecium*: effects of increased viscosity." *J Exp Biol* 57(1): 239-59.
- Machin, K. E. (1958). "Wave Propagation Along Flagella." *Journal of Experimental Biology* 35(4): 796-806.

- Machin, K. E. (1963). "Control and Synchronization of Flagellar Movement." Proceedings of the Royal Society of London Series B-Biological Sciences 158(970): 88-&.
- Minoura, I., T. Yagi, et al. (1999). "Direct measurement of inter-doublet elasticity in flagellar axonemes." Cell Struct Funct 24(1): 27-33.
- Misteli, T. (2001). "The concept of self-organization in cellular architecture." J Cell Biol 155(2): 181-5.
- Moore, H., K. Dvorakova, et al. (2002). "Exceptional sperm cooperation in the wood mouse." Nature 418(6894): 174-177.
- Nedelec, F. J., T. Surrey, et al. (1997). "Self-organization of microtubules and motors." Nature 389(6648): 305-8.
- Nielsen, E., F. Severin, et al. (1999). "Rab5 regulates motility of early endosomes on microtubules." Nat Cell Biol 1(6): 376-82.
- Nishiura, M., T. Kon, et al. (2004). "A single-headed recombinant fragment of Dictyostelium cytoplasmic dynein can drive the robust sliding of microtubules." J Biol Chem 279(22): 22799-802.
- Oiwa, K. and H. Sakakibara (2005). "Recent progress in dynein structure and mechanism." Curr Opin Cell Biol 17(1): 98-103.
- Okamoto, K. I. and Y. Nakaoka (1994). "Reconstitution of Metachronal Waves in Ciliated Cortical Sheets of Paramecium - Wave Stabilities." J Exp Biol 192(1): 61-72.
- Okuno, M. and Y. Hiramoto (1979). "Direct Measurements of the Stiffness of Echinoderm Sperm Flagella." Journal of Experimental Biology 79(APR): 235-243.
- Pollard, T. D. (2003). "The cytoskeleton, cellular motility and the reductionist agenda." Nature 422(6933): 741-5.
- Press, W. H., W. T. Vetterling, et al. (2002). Numerical Recipes in C++. Cambridge, UK, Cambridge University Press.
- Prigogin, I. and G. Nicolis (1967). "On Symmetry-Breaking Instabilities in Dissipative Systems." Journal of Chemical Physics 46(9): 3542-&.
- Pringle, J. W. S., Ed. (1977). Insect Flight Muscle. North-Holland, Amsterdam.
- Purcell, E. M. (1977). "Life at Low Reynolds-Number." American Journal of Physics 45(1): 3-11.
- Rikmenspoel, R. (1965). "The tail movement of bull spermatozoa. Observations and model calculations." Biophys J 5(4): 365-92.
- Rikmenspoel, R., G. Vanherpen, et al. (1960). "Cinematographic Observations of the Movements of Bull Sperm Cells." Physics in Medicine and Biology 5(2): 167-181.
- Satir, P. (1968). "Studies on cilia. 3. Further studies on the cilium tip and a "sliding filament" model of ciliary motility." J Cell Biol 39(1): 77-94.
- Schief, W. R., R. H. Clark, et al. (2004). "Inhibition of kinesin motility by ADP and phosphate supports a hand-over-hand mechanism." Proceedings of the National Academy of Sciences of the United States of America 101(5): 1183-1188.
- Schliwa, M., Ed. (2003). Molecular Motors. Weinheim, Wiley-VCH Verlag.
- Schliwa, M. and G. Woehlke (2003). "Molecular motors." Nature 422(6933): 759-65.
- Schmitz, K. A., D. L. Holcomb-Wygle, et al. (2000). "Measurement of the force produced by an intact bull sperm flagellum in isometric arrest and estimation of the dynein stall force." Biophys J 79(1): 468-78.
- Shingyoji, C., H. Higuchi, et al. (1998). "Dynein arms are oscillating force generators." Nature 393(6686): 711-4.

- Shingyoji, C., K. Yoshimura, et al. (1995). "Effect of beat frequency on the velocity of microtubule sliding in reactivated sea urchin sperm flagella under imposed head vibration." J Exp Biol 198(Pt 3): 645-53.
- Shiroguchi, K. and Y. Y. Toyoshima (2001). "Regulation of monomeric dynein activity by ATP and ADP concentrations." Cell Motil Cytoskeleton 49(4): 189-99.
- Sleigh, M. A., Ed. (1974). Cilia and Flagella. London, Academic Press Inc.
- Strogatz, S. H. (2000). Nonlinear Dynamics and Chaos. Cambridge, MA, Westview Press.
- Summers, K. E. and I. R. Gibbons (1971). "Adenosine triphosphate-induced sliding of tubules in trypsin-treated flagella of sea-urchin sperm." Proc Natl Acad Sci U S A 68(12): 3092-6.
- Taylor, G. (1951). "Analysis of the swimming of microscopic organisms." Proc. Roy. Soc. 209: 447-461.
- Turing, A. M. (1952). "The Chemical Basis of Morphogenesis." Philosophical Transactions of the Royal Society B (London) 237: 37-72.
- Vernon, G. G. and D. M. Woolley (2004). "Basal sliding and the mechanics of oscillation in a mammalian sperm flagellum." Biophys J 87(6): 3934-44.
- Warner, F. D. (1976). "Ciliary inter-microtubule bridges." J Cell Sci 20(1): 101-14.
- Woolley, D. M. (2003). "Motility of spermatozoa at surfaces." Reproduction 126(2): 259-70.
- Woolley, D. M. and G. G. Vernon (2001). "A study of helical and planar waves on sea urchin sperm flagella, with a theory of how they are generated." J Exp Biol 204(Pt 7): 1333-45.
- Wu, X. L. and A. Libchaber (2000). "Particle diffusion in a quasi-two-dimensional bacterial bath." Physical Review Letters 84(13): 3017-3020.
- Young, H. D. (1962). Statistical Treatment of Experimental Data. Prospect Heights, Waveland Press, Inc.
- Zahn, K., R. Lenke, et al. (1999). "Two-stage melting of paramagnetic colloidal crystals in two dimensions." Physical Review Letters 82(13): 2721-2724.
- Zahn, K., G. Maret, et al. (2003). "Three-particle correlations in simple liquids." Physical Review Letters 91(11): 115502.
- Zaikin, A. N. and A. M. Zhabotinsky (1970). "Concentration wave propagation in two-dimensional liquid-phase self-oscillating system." Nature 225(535): 1970.

Erklärung

Die vorliegende Arbeit wurde unter der wissenschaftlichen Betreuung von Herrn Prof. Dr. Jonathon Howard vom Max Planck Institut für Molekulare Zellbiologie und Genetik sowie von Herrn Prof. Dr. Frank Jülicher vom Max Planck Institut für Physik Komplexer Systeme in Dresden durchgeführt. Weiterhin bestand eine enge Zusammenarbeit mit Herrn Dr. Karsten Kruse und Herrn Andreas Hilfinger.

Die Promotionsordnung der Fakultät Mathematik und Naturwissenschaften der Technischen Universität Dresden vom 20. März 2000 erkenne ich an.

Hiermit versichere ich, daß ich die vorliegende Arbeit ohne unzulässige Hilfe Dritter und ohne Benutzung anderer als der angegebenen Hilfsmittel angefertigt habe; die aus fremden Quellen direkt oder indirekt übernommen Gedanken sind als solche kenntlich gemacht. Die Arbeit wurde bisher weder im Inland noch im Ausland in gleicher oder ähnlicher Form einer anderen Prüfungsbehörde vorgelegt.

Dresden, den

Ingmar Riedel